FINAL REPORT - PHASE B

Report No. 0038-B-F

Prepared For:

NATIONAL AERONAUTICS AND SPACE ADMINISTRATION
COMMUNICATION RESEARCH BRANCH
CODE 625
GODDARD SPACE FLIGHT CENTER
GREENBELT, MARYLAND

A. Kampinsky
Technical Officer
Extension 4106

Under:

Contract No. NAS 5-3232

Conductron Corporation

343 SOUTH MAIN STREET
ANN ARBOR, MICH.

FINAL REPORT - PHASE B

Report No. 0038-B-F

Prepared For:

NATIONAL AERONAUTICS AND SPACE ADMINISTRATION
COMMUNICATION RESEARCH BRANCH
CODE 625
GODDARD SPACE FLIGHT CENTER
GREENBELT, MARYLAND

A. Kampinsky
Technical Officer
Extension 4106

Under:

Contract No. NAS 5-3232

TABLE OF CONTENTS

PREFACE

The work which is reported herein is a combined theoretical and experimental effort.

Among the many who participated creatively and effectively in this program were V. H. Weston, A. W. Wren, R. E. Kovac, M. J. Rycus, E. LeBaron, R. A. Henry, and H. E. Brooks. Professor E. F. Masur, of the Engineering Mechanics Department, University of Michigan, wrote Appendices B and C. Most of the numerical work was performed on Conductron's IBM 1620 computer.

R. K. Ritt
Project Manager

1. INTRODUCTION

This report is written at the conclusion of the second phase of studies and measurements performed by Conductron Corporation for NASA, GSFC, under Contract No. NAS 5-3232. The work done in the first phase, Balloon Segment Measurements, has previously been reported (Conductron Report No. 0038-2-A-F), and will, in the present report, be further discussed and related to the second phase work.

The second phase program has consisted of several separate, but related tasks, which we shall now describe in general terms, and which shall be discussed in detail below.

Task 1. To postulate a balloon structure, on the basis of experimental and theoretical materials studies supplied to Conductron by NASA, and from this postulated structure to predict the reflectivity of the balloon as a function of surface stress, frequency, polarization, and viewing aspect. Further, to examine these material studies to compare with conclusions independently arrived at by Conductron.

Task 2. To perform radar reflectivity measurements on the inflated balloon during Static Inflation Tests at Lakehurst NAS; to reduce data obtained, and from the reduced data to determine the radar reflectivity properties of the balloon as a function of surface stress, frequency, polarization, and viewing aspect.

Task 3. To predict the radar reflectivity properties of the inflated balloon, as a function of surface stress, frequency, polarization, and viewing aspect, on the basis of photogrammetric measurements made during the Static Inflation Tests, and supplied to Conductron by NASA.

These tasks were formulated by NASA as components of a program whose overall objective is to develop and establish means of estimating flight performance of passive communications satellites on the basis of pre-flight experiments, and to provide guidelines in the selection of satellite materials, fabrication, and deployment techniques. Although the NASA-Conductron program which this report describes is concerned primarily with the A-12 (Echo II) satellite, the techniques developed are not limited to a particular passive system.

2. THEORETICAL CONSIDERATIONS

The theoretical question which underlies most of the work done during this phase has been:

Given the shape of a conducting surface, and a given source of electromagnetic energy, what is the electromagnetic field observed at an arbitrary point not on the surface?

This question, of course, is the central problem in electromagnetic theory. In this section, a mathematical formulation of the problem is given which is particularly appropriate to the balloon configuration with which we are dealing. By this is meant that when this formulation is completed, and the balloon and the operating frequencies specified, approximations which lead to numerical answers can readily be made.

Certain preliminary remarks are necessary. Let the time dependence of the electromagnetic field be harmonic, with frequency f cycles/sec. Let $\omega = 2\pi f$. Then the electric and magnetic components of the field can be represented, respectively, as

$$\underline{E}\,(x, y, z)\, e^{-i\omega t}$$

and

$$\underline{H}\,(x, y, z)\, e^{-i\omega t}.$$

$\underline{E}$ and $\underline{H}$ are complex vectors. Let $k = \frac{\omega}{c}$, where c = velocity of light in vacuo, and let units be chosen so that the permeability and permittivity of free space are both unity. Then $\underline{E}$ and $\underline{H}$ satisfy the Maxwell equations:

$$\left.\begin{aligned} \nabla \times \underline{E} - i\,k\,\underline{H} &= 0 \\ \nabla \times \underline{H} + i\,k\,\underline{E} &= 0 \end{aligned}\right\} \qquad (1)$$

Let $\underline{E}^{(i)}$ and $\underline{H}^{(i)}$ be the field components which would be present if just the energy source, but not the conducting surface, were present. In any region of space which excludes the source, the pair $\underline{E}^{(i)}$, $\underline{H}^{(i)}$ satisfy (1). $\underline{E}^{(i)}$ and $\underline{H}^{(i)}$ are called the incident fields.

In the presence of the conducting body, the total field $\underline{E}$, $\underline{H}$, has the form:

$$\left.\begin{aligned} \underline{E} &= \underline{E}^{(i)} + \underline{E}^{(s)} \\ \underline{H} &= \underline{H}^{(i)} + \underline{H}^{(s)} \end{aligned}\right\} \qquad (2)$$

$\underline{E}^{(s)}$ and $\underline{H}^{(s)}$ are called the scattered fields. The scattered field is generated by currents induced on the conducting surface. If the surface is perfectly conducting, the value of the current, $\underline{J}(x, y, z)$, at a point on the surface, is given by the formula

$$\underline{J}(x, y, z) = \hat{n}(x, y, z) \times \underline{H}(x, y, z) \tag{3}$$

In (3), $\hat{n}(x, y, z)$ is the outward normal to the surface, and $\underline{H}$ is the total magnetic field.

Let the position vector of a point (x, y, z) be designated by $\vec{r} = x\hat{x} + y\hat{y} + z\hat{z}$, where $\hat{x}$, $\hat{y}$, $\hat{z}$ are the unit coordinate vectors. The scattered magnetic field can be represented by the formula:

$$\underline{H}^{(s)}(\vec{r}) = \frac{-1}{4\pi} \iint_S \left\{\underline{J}(\vec{r}_1) \times (\vec{r} - \vec{r}_1)\right\} \left\{\frac{ik\,|\vec{r} - \vec{r}_1| - 1}{|\vec{r} - \vec{r}_1|^3}\right\} e^{ik|\vec{r} - \vec{r}_1|}\, d\,S(\vec{r}_1) \tag{4}$$

In (4) the integral is taken over the surface of the perfectly conducting body. The surface current $J(\vec{r})$ must satisfy the equation:

$$\underline{J}(\vec{r}) = 2\,[\hat{n}(\vec{r}) \times \underline{H}^{(i)}(\vec{r})] - \frac{1}{2\pi}\,\hat{n}(\vec{r}) \times \iint_S \left\{\underline{J}(\vec{r}_1) \times (\vec{r} - \vec{r}_1)\right\} \left\{\frac{ik\,|\vec{r} - \vec{r}_1| - 1}{|\vec{r} - \vec{r}_1|^3}\right\} e^{ik|\vec{r} - \vec{r}_1|}\, dS(\vec{r}_1) \tag{5}$$

The derivation of equation (4) can be found in "Electromagnetic Theory", J. A. Stratton, pp. 460-468. It depends upon equation (1) and the fact that at the perfectly conducting surface, the tangential component of the total field must vanish. The derivation of (5) is implicit in this same section of Stratton; it can be found explicitly in Maue [Zeit f Physik, 126 (1949)].

Equations (4) and (5) provide a formulation of the problem. Given the incident magnetic field, $\underline{H}^{(i)}$, and the surface, S, a solution $\underline{J}(\vec{r})$ must be found for (5). Then this solution must be inserted into the integral (4); the resulting integration gives the scattered field, $H^{(s)}(\vec{r})$.

Equation (5) is an integral equation for $\underline{J}(\vec{r})$. In principle it has a unique solution, but in practice this solution, except for some very special cases, cannot be represented in a form which is amenable to numerical calculation. It is now appropriate to discuss the approximation to $\underline{J}(\vec{r})$ when S is a balloon-like structure.

2.1 THE SOURCE FIELD, $\underline{H}^{(i)}(\vec{r})$

The incident field is created by a distribution of currents located in a finite volume V. If some point within this volume is chosen to be the center of a fixed coordinate system, then analogous to (4), the incident field can be represented as an integral:

$$\underline{H}^{(i)}(\vec{r}) = -\frac{1}{4\pi} \iiint_V \left\{ \underline{J}^{(i)}(\vec{r}_1) \times (\vec{r} - \vec{r}_1) \right\} \left\{ \frac{ik\,|\vec{r} - \vec{r}_1| - 1}{|\vec{r} - \vec{r}_1|^3} \right\} e^{ik|\vec{r}-\vec{r}_1|}\, dV(\vec{r}_1) \tag{6}$$

Let $\vec{r} = R\,\hat{u}$, where $\hat{u}$ is a unit vector. Then,

$$\lim_{R \to \infty} R\, e^{-ikR}\, \underline{H}^{(i)}(R\hat{u}) = \frac{ik}{4\pi} \iiint_V \left\{ \underline{J}^{(i)}(\vec{r}_1) \times \hat{u} \right\} e^{-ik\hat{u}\cdot\vec{r}_1}\, dV(\vec{r}_1) = \underline{F}(\hat{u}) \tag{7}$$

In (7) $\underline{F}(\hat{u})$ is a vector which depends only on $\hat{u}$, and which is perpendicular to $\hat{u}$. We rewrite (7) in the form

$$\underline{H}^{(i)}(R\,\hat{u}) \sim \frac{e^{ikR}}{R}\, \underline{F}(\hat{u}) \tag{8}$$

If the source is a high gain antenna, $|\underline{F}(\hat{u})|$ will have a maximum for a fixed direction, $\hat{u}_o$, it will be approximately constant for a set of directions satisfying the inequality

$$\hat{u} \cdot \hat{u}_o > \cos \beta/2,$$

and very small, relative to $|\underline{F}(\hat{u}_o)|$, if $\hat{u} \cdot \hat{u}_o < \cos \beta/2$. The angle β is called the beamwidth of the antenna. If the antenna is constructed so that the only contributions made to $\underline{F}(\hat{u})$ in the integral (7) come from currents with a fixed direction, $\hat{p}_1$, then $\underline{F}(\hat{u}) = G(\hat{u})\,\hat{p}$, where $\hat{p} = \hat{p}_1 \times \hat{u}$.

Then for directions $\hat{u}$ within the beam (i.e., $\hat{u} \cdot \hat{u}_o > \cos \beta/2$),

$$\underline{H}^{(i)}(R\,\hat{u}) \sim \frac{e^{ikR}}{R}\, G(\hat{u})\,\hat{p}.$$

This represents a spherical wave, propagating radially, with wavelength $\lambda = \frac{2\pi}{k}$. The constant phase surfaces are spheres, and for large values of R, can be approximated by planes. Therefore, it is conventional, if the surface S' is located within the beam, and if R is sufficiently large, to replace $H^{(i)}(\vec{r})$ by a linearly polarized plane wave,

$$H^{(i)}(\vec{r}) \sim e^{ik\hat{u}_o \cdot \vec{r}} \hat{p}_o, \text{ where } \hat{p}_o = \hat{p}_1 \times \hat{u}_o.$$

As far as the surface of the scatterer is concerned, the only difference between this field and the true incident field is the constant numerical factor $\frac{G(\hat{u}_o)}{R}$, and since the integral equation (5) is linear, the solution is changed by multiplication by this constant factor. If the coordinate system is changed so that the center of coordinates is at the scatterer instead of at the source, the representation for the incident plane wave is then

$$\underline{H}^{(i)}(\vec{r}) = e^{-ik\hat{u}_o \cdot \vec{r}} \hat{p}_o \qquad (9)$$

Therefore, in the discussion of the reflectivity properties of the balloon, the incident magnetic field will be taken to be of the form (9). The criterion for the permissibility of this replacement is a measure of the deviation, over the region occupied by the scatterer, of the true spherical wave front and the plane wave front. This criterion is called the far zone criterion, and is usually defined by the requirement that

$$R \gg \frac{4\, d^2}{\lambda} \qquad (10)$$

where d is the largest dimension of the scatterer perpendicular to the beam.

2.2 APPROXIMATE SOLUTION TO (5)

If $\underline{H}^{(i)}(\vec{r})$ is a plane wave, (9), and if the scatterer is a convex surface, it is possible to define the illuminated and the shadow region. Referring to Figure 1

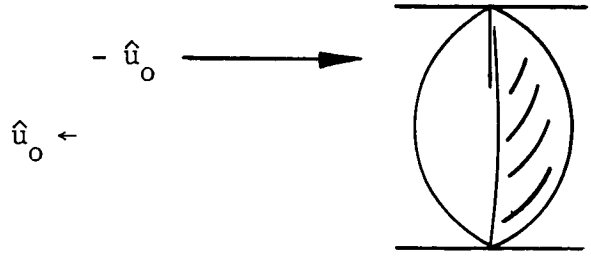

Figure 1

The direction of propagation is $-\hat{u}_o$, the shaded region is the shadow region, and the unshaded region is the illuminated region. It has been shown by V. A. Fock [Journal of Physics, USSR, 10, 130-136 (1946)] and more rigorously by J. A. Cullen [Phys. Rev., 109, 6, 1863-1867 (1958)] that as $k \to \infty$, the solution, $\underline{J}(\vec{r})$ has the limiting form

$$\underline{J}(\vec{r}) = \begin{cases} 2\,\hat{n}(\vec{r}) \times H^{(i)}(\vec{r}) & \text{in illuminated region} \\ 0 & \text{in shadow region} \end{cases} \qquad (11)$$

This is the classical geometric optics solution; when this solution is substituted into (4), the resulting representation for $H^{(i)}(\vec{r})$ is called the physical optics integral.

2.3 THE VALIDITY OF THE PHYSICAL OPTICS INTEGRAL

The theoretical calculations performed by Conductron on the Echo II balloon have been to compute $H^{(i)}(\vec{r})$ by means of the physical optics integral. The justification for this is based both on elementary physical considerations as well as rigorous information based on the Fock theory.

The obvious physical justification for using (11) to represent the current distribution can be obtained by the examination of equation (5). If S were an infinite plane the vectors $\underline{J}(\vec{r}_1)$ and $\vec{r} - \vec{r}_1$ in the integral would both lie in the plane, and therefore the cross-product $\hat{n}(\vec{r}) \times [\underline{J}(\vec{r}_1) \times (\vec{r} - \vec{r}_1)]$ would vanish for all $\vec{r}_1$. Thus, for S an infinite plane, the exact solution of (5) is $2\,\hat{n}(\vec{r}) \times H^{(i)}(\vec{r})$, this being independent of either k or the form of $H^{(i)}(\vec{r})$. Qualitatively, one sees that if the surface deviates only slightly from being a plane, this representation continues to be a good approximation. The question arises: what is meant by "deviates slightly from being a plane"? Since Maxwell's equations are unaltered if the distance scale and the wavelength $2\pi/k$ are multiplied by the same factor, it is clear that if a is a distance which plays a role in the description of the fields, then the product ka must be preserved if the fields are to be unaltered. Since the deviation of a surface from being a plane is measured by its principal radii of curvature, the statement that the surface "deviates slightly from being a plane" can be equated to the statement that "ka must be large", where a is either of the principal radii of curvature. Although the above dimensional argument is not at all rigorous, it contains the physical reasoning which has been used to justify the use of physical optics to compute radar reflectivity.

Historically, the physical optics integral has been used to calculate the numerical values of the fields scattered by a great number of perfectly conducting bodies. Because the justification for using the method is in general the intuitive argument given above, the success of the method has been measured in terms of comparison with experiment or with exact solutions, when they can be found.

The geometric optics solution to (5), given by (11) implies, in general, a discontinuity in the current at the boundary between the illuminated and

shadow region, called the shadow boundary. When this solution is inserted into the integral (4), the evaluation of the integral may sometimes be accomplished by an integration by parts in which the values of $\vec{J}(\vec{r})$ at the shadow boundary appear explicitly. When the curve orthogonal to the shadow boundary has finite curvature, such as in the case of the sphere, this contribution is spurious. In the case in which the shadow boundary has infinite curvature, as with a flat plate, or an infinite plane with a hole, the solution (11) does not take into account edge currents.

In the case of the curve orthogonal to the shadow boundary having finite curvature the work of Fock gives a rigorous criterion for the use of the current (11) in the evaluation of (4). In a joint paper with M. Leontovitch [Journal of Physics, X, 13 (1946)] and in the paper referred to above, he established that the value of $\vec{J}(\vec{r})$, in fact, varied continuously from approximately its geometric optics value in the illuminated region to approximately its zero value in the shadow region, the variation taking place in the penumbra region, a region of width

$$d = \sqrt[3]{\frac{\lambda R_o^2}{\pi}} \qquad (12)$$

where R_o is the radius of curvature of the geodesic in the direction of the propagation vector as it crosses the shadow boundary (see Figure 2)

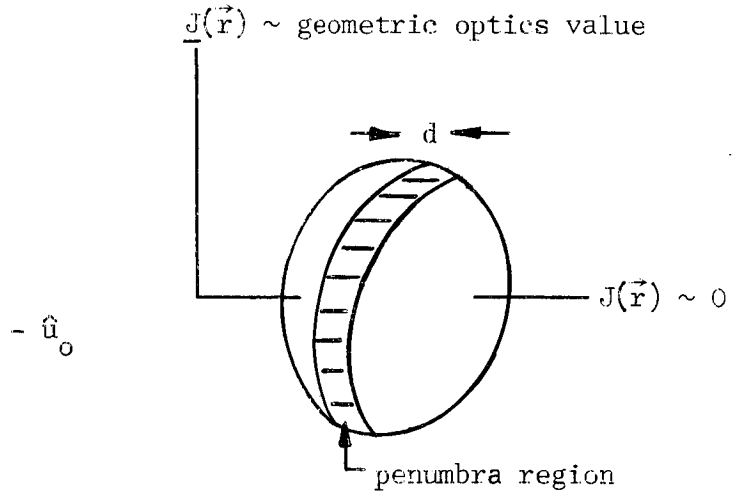

Figure 2

In the case of a sphere, for example, with $R_o = a$, the width of the penumbra region is

$$d = \left(\frac{2}{ka}\right)^{1/3} a$$

Thus, the area of the penumbra $\sim 2\pi a^2 \left(\frac{2}{ka}\right)^{1/3}$. Because the magnitude of the geometric optics current does not depend upon k, this shows that the

field computed by means of the physical optics integral is related to the true field by a relationship

$$H^{(s)}(\vec{r})\Big|_{\text{True}} = H^{(s)}(\vec{r})\Big|_{\text{Physical Optics}} \{1 + O([ka]^{-1/3})\}, \qquad (13)$$

where $O(x)$ is a function which, when multiplied by x, remains bounded as $x \to \infty$.

In general, for a perfectly conducting body, the error incurred in using the physical optics integral is $O([k R_o]^{-1/3})$, where R_o is the smallest radius of curvature of geodesics along the direction of propagation when they cross the shadow boundary. From the above definition of $O(x)$ it should be observed that this is an upper bound on the error.

It should further be observed that this criterion for the use of physical optics is less restrictive than the intuitive criterion stated above. It only requires that the numbers ka be large at the shadow boundary and not necessarily at all points in the illuminated region. The work of Fock refers, strictly, only to convex bodies. For such bodies it is rigorously true that for plane wave incidence the physical optics field will be in error as described above. In a later paper, [ZETF, 20, 961-978 (1950)] this result was generalized to include incident fields of spherical type.

In the work performed by Conductron in the present phase, two models of the Echo II balloon have been considered. The first is that of a convex body determined by various materials studies. To this model the above discussion applies. The second model is that of a "perturbed" sphere: namely, a surface having the equation:

$$\begin{aligned} x &= [a + \delta(\theta, \varphi)] \sin\theta \cos\varphi \\ y &= [a + \delta(\theta, \varphi)] \sin\theta \sin\varphi \\ z &= [a + \delta(\theta, \varphi)] \cos\theta \,, \quad 0 \le \theta \le \pi,\ 0 \le \varphi \le 2\pi \end{aligned} \qquad (14)$$

in which $|\delta| \ll a$.

The values of $\delta(\theta, \varphi)$ were obtained from photogrammetric measurements performed during the Static Inflation Tests.

Although the theory of statistically rough surfaces has been studied extensively, and the statistics of the balloon surface could be obtained by measurement of the values of $\delta(\theta, \varphi)$, the answers to questions about statistically rough surfaces are statistical answers. Since not just the statistics of $\delta(\theta, \varphi)$ was known, but $\delta(\theta, \varphi)$ itself was known, it was felt that a better result than a statistical one could be obtained. Therefore it was decided to attempt to extend the work of Fock to find conditions under which the use of the physical optics integral could be justified for the surface (14). It was conjectured that if the principal radii of curvature remained large in comparison to the wavelength, and if except for points in the

penumbra region no shadows for geometric rays existed, that the physical optics solution could be used. This conjecture was verified and is included as Appendix E.

2.4 THE PHYSICAL OPTICS INTEGRAL

If $\underline{J}(\vec{r})$ is taken to be the geometric optics solution, (11), and if $\underline{H}^{(i)}$ is a linearly polarized plane wave, then the physical optics integral can be written:

$$\underline{H}^{(s)}(\vec{r}) = -\frac{1}{2\pi}\iint_S \left\{\hat{n}(\vec{r}_1) \times \hat{p}\right\} \times (\vec{r} - \vec{r}_1)\left\{\frac{ik|\vec{r} - \vec{r}_1| - 1}{|\vec{r} - \vec{r}_1|^3}\right\} e^{-ik\hat{u}_o\cdot\vec{r}_1} e^{2k|\vec{r}-\vec{r}_1|}\, dS(\vec{r}_1)$$

where the integration is extended over the illuminated region. Let $\hat{u}^*$ be a unit vector and let $\vec{r} = R\,\hat{u}^*$. Then

$$\lim_{R\to\infty} R\, e^{-ikR}\, \underline{H}^{(s)}(R\,\hat{u}^*) = -\frac{ik}{2\pi}\iint_S \left\{(\hat{n}(\vec{r}_1) \times \hat{p}) \times \hat{u}^*\right\} e^{-ik[\hat{u}_o \times \hat{u}^*]\cdot\vec{r}_1}\, dS(\vec{r}_1) \qquad (15)$$

If $u^* = \hat{u}_o$, so that the field is being observed in the backscattered direction, because $\hat{u}_o \cdot \hat{p} = 0$, (15) has the simplified representation

$$\lim_{R\to\infty} R\, e^{-ikR}\, \underline{H}^{(s)}(R\,\hat{u}_o) = -\frac{ik}{2\pi}\iint_S \left\{(\hat{n}(\vec{r}_1)\cdot\hat{u}_o\right\}\hat{p}\, e^{-2ik[\hat{u}_o]\cdot\vec{r}_1}\, dS(\vec{r}_1)\,.$$

2.5 THE RADAR CROSS SECTION

For a spherical wave, and in the units chosen, the power flux in the direction of propagation is $|\underline{H}|^2$. [See Stratton, p. 457] If an incident plane wave,

$$\underline{H}^{(i)} = A\, e^{-ik\hat{u}_o\cdot\vec{r}}\,\vec{p}$$

illuminates a body and if $\underline{H}^{(s)}(\vec{r})$, a spherical wave is the scattered field, then the quantity

$$\lim_{R\to\infty} \frac{4\pi R^2}{A^2}\,|\underline{H}^{(s)}(R\,\hat{u}^*)|^2$$

is called the bistatic radar cross section; $\sigma(\hat{u}_o, \hat{u}^*)$, of the scatterer. Physically, it represents the power radiated per unit solid angle in the direction $\hat{u}^*$ as compared to the power incident upon the scatterer. It obviously has the dimensions of area, and when $\hat{u}^* = \hat{u}_o$, it is called the back-scattered cross section, or the echo area. If $\underline{H}^{(s)}(\vec{r})$ is given by the physical optics integral, the cross section is

$$\sigma(\hat{u}_o,\hat{u}^*) = \frac{k^2}{\pi} \left| \iint [(\hat{n}(\vec{r}_1) \times \hat{p}_1) \times \hat{u}^*] \, e^{-ik[\hat{u}_o \, \hat{u}^*]\cdot\vec{r}_1} \, dS(\vec{r}_1) \right|^2$$

3. BALLOON MATERIALS STUDY AND POSTULATED BALLOON STRUCTURE

Conductron was provided, by NASA, with copies of the following reports:

A) "Structural Analysis of Echo II to Predict the Surface Configuration", Final Report NAS 5-2365, January 1963, Fairchild Stratos Corporation.

B) "Structural Analysis of Echo II", Interim Report No. 1, NAS 5-3229, May 1963, Astro Research Corporation.

Our objective, in this part of the program, was two-fold:

(a) To postulate a balloon structure consistent with the analyses and predictions made in A) and B) and to perform theoretical calculations to determine the radar cross-section of this structure.

(b) To provide NASA with a critical evaluation of the reports A) and B).

3.1 THE BALLOON STRUCTURE

The Echo II balloon is constructed of 106 nominally identical gores of a three layer laminate, the outer layers being aluminum, the inner layer mylar. These gores are initially cut from a flat sheet, and are joined together by taped seams. The polar regions are covered by "polar caps" of the balloon material. In the operational balloon, four gores (two diametrically opposite pairs of adjacent gores) are reinforced to support telemetry equipment. These reinforced gores are not considered in the present discussion.

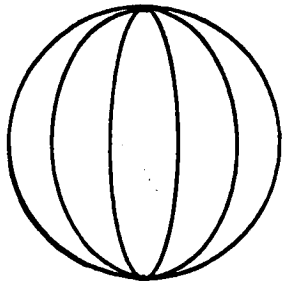

Figure 3 (Not Scale)

Figure 3 illustrates the configuration of a typical gore relative to the polar caps and the nominal spherical shape.

Figure 4

Figure 4 illustrates a typical latitudinal section corresponding to the dotted curve in Figure 3. The dots represent the seams.

The mathematical model chosen for each gore can be described in terms of Figure 5.

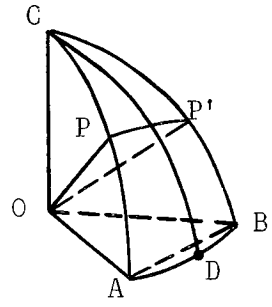

Figure 5

The figure represents the gore in the upper hemisphere. The gore itself is bounded by the arcs AC, BC, and the arc AB is in the equatorial plane. The arcs AC, BC are circular arcs having the radius, a, of the nominal sphere (a = 67.5 ft). The points P and P' have the same height above the equatorial plane. The plane determined by POP' intersects the surface of the gore in a curve PP'. This arc PP' is a circular segment with a radius R which is independent of the height of P and P' above the equatorial plane. The orthogonal trajectories to the arcs PP' are a family of circular arcs of which the arcs AC, BC, and CD are particular members. The radii of these circular arcs are, in general, different for different members of the family. The contrary is true only when the gore is a spherical segment. However, the largest possible value of this radius is a, and the smallest possible value is the perpendicular distance from O to the chord AB. The angle $AOB = \frac{360^{o}}{106} \simeq 3.4^{o}$, corresponding to the fact that there are 106 gores.

The value of R varies from R = a to R = ∞. This last value is the limiting case in which the "arcs" PP' become straight lines, and the gore is "flat". The selection of R was made by using the conclusions of report B) referred to above. The contours predicted in that report were actually fitted better by parabolas than by circles, but the radius of curvature along the parabola did not vary enough to effect, numerically, the assumption that it was, in fact, constant.

The calculations were submitted to NASA in the form of a technical report, and is included as Appendix A of the present report.

3.2 MATERIAL BEHAVIOR ANALYSIS

The purpose of the analysis in report A) was to "predict the surface configuration of the satellite when the internal pressure differential has been increased to various levels and reduced to zero pressure differentiated in a zero-g field."

This analysis depended first upon performing experiments to obtain the stress-strain curve for the material by experimental tests, and to determine the elastic modulus and the inelastic range. Using this data, a typical gore configuration was analyzed using membrane theory.

In Appendix B is found the Conductron discussion of the Fairchild Stratos Report. The principal issue taken by Conductron with this report is the failure to take into account the boundary layer analysis required in the neighborhood of the seams. Technically, this failure consists of neglecting, in the relevant differential equations those terms containing higher powers of t, where t is the skin thickness, and the linearization of the equations. To illustrate the effect of this over-simplification, in Section B.3 of Appendix B, the analogous problem for a cylindrical, rather than a spherical structure, is investigated. The choice of this problem was not based on any direct relevance of the solution to the Echo II satellite, but to illustrate, in a case in which the analysis can be completely performed, the effect of linearization of the equations and neglect of the higher order terms.

The purpose of report B) was to predict the "departure of satellite skin from spherical shape" by applying analysis to experimental data. The Conductron discussion of the Astro Report is contained in Appendix C. The principal disagreement of Conductron with this report is its assumption, in considering the displacement of the balloon from its nominal spherical configuration, that material points move only in the radial direction. Other disagreements can be found and are explicitly stated in Appendix C, but this principal disagreement is crucial. In this appendix, an analysis is performed in which the displacements and membrane forces are computed. It is shown that the meridional curves are not circles, as predicted by the Astro report, but that they are "flattened", and the amount of flattening is explicitly determined.

4. STATIC INFLATION TESTS

During the months of July and August three Echo II balloons, Nos. 9, 11, and 13, were inflated within the large dirigible hangar at Lakehurst NAS. Conductron performed radar cross section measurements on the three balloons and submitted Technical Report No. 0038-4-T to NASA describing the measurement program and the data reduction. This technical report is included herein as Appendix D.

Figure 6 is a scale drawing of the measurement configuration as viewed from above. The balloon is represented by the circle with center at O. The arc $T_L T_R$ is a circular arc subtending the angle $T_L O T_R = 30^o$. This arc represents a platform elevated approximately 50'. On either end of the platform are mounted transmitting antennas at T_R and T_L aligned to propagate in the direction $T_R O$ and $T_L O$, respectively. The receiving antenna moves along the track, aligned always to point at O, and the measurement is bistatic, the bistatic angle being $T_R OR$ or $T_L OR$ dependent upon which transmitter is activated. The plane $T_L T_R O$ is 10^o below the equatorial plane. The frequencies used were 1.31 KMC, 5.85 KMC, 5.65 KMC. A description of the measurement sequence and calibration is given in Appendix D.

4.1 EXPERIMENT DESIGN

The first fact to be recognized in planning the measurements was that in no way could measurements be performed in the far zone of the sphere. The results of Appendix A show that the field contribution of the scattering by at least three adjacent gores are necessary to give the correct radar cross-section. The width across these gores is $\sim\sqrt{10}$ meters; consequently, at C band the far zone of the sphere is defined by a range which is much greater than $\frac{10}{\lambda} \sim 200$ meters.

However, previous work by V. H. Weston [Trans. IRE, PGAP, AP-7, 43-51 (1959)], had shown that for spheres whose diameter is large in comparison to wavelength, the near zone field can easily be computed. Although this fact was initially obtained for plane wave incidence, it was found, using essentially different methods, to be valid equally for spherical wave incidence. The derivation is included as Section D.7 of Appendix D. Using the formulas therein, it was then possible to derive the fact that at a measurement range of 100 ft. from the surface of the balloon, the measured cross-section should be increased by 4.5 db to obtain the far-field radar cross section. This derivation appears in Section D.3.

The decision to use the measuring range of 100 ft. was a compromise involving several factors. For several reasons it was decided to use CW transmissions: it was economical, simple to maintain, and spectrally pure. Although there was no reason to anticipate dispersion problems, there was good reason to preclude them. Because of the low power (.5 - 1 w) of the

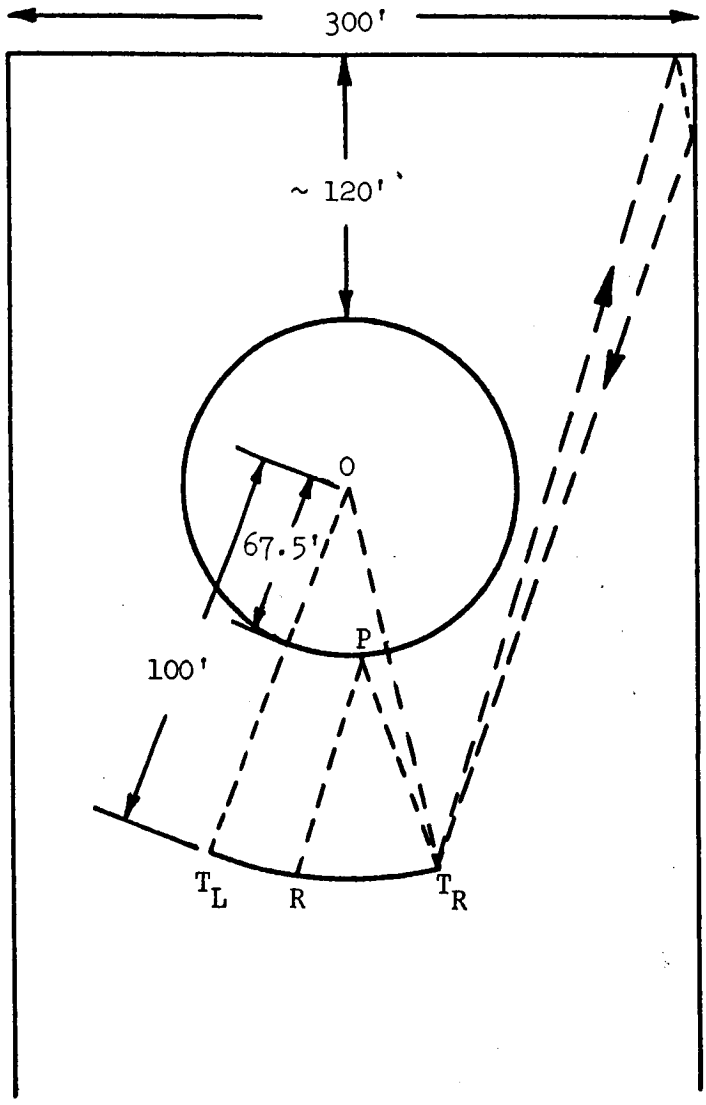

Figure 6 Scale Drawing of Hangar - Balloon-Track Configuration

CW system, it was desirable to bring the system as close to the balloon as possible, to increase system sensitivity. Simultaneously, it was desirable to remain in the far field of the antennas, which were standard gain horns. After verifying, during the hangar background measurements described in D.2 that in the region indicated by the arc $T_L T_R$ in Figure 6 the background levels were 20-30 db below the nominal balloon return, the 100 ft. distance was chosen to meet these demands. Using this range made it relatively easy to provide under-illumination of 12 db at the edge of the balloon, reducing the power in such unwanted reflection paths indicated by the arrowed lines in Figure 6.

Having selected the measurement configuration another question had to be dealt with. For a typical bistatic transmission the boresight of the antenna located at T_R, for example, would be aligned along the path $T_R O$. For the receiving antenna located at R, the main contribution to the received field is caused by the illumination in the neighborhood of the point P indicated on Figure 6, where the angles $OT_R P$ and ORP are equal. For the range chosen, the angle $OT_R P$ is sufficiently large so that the effect of beam taper must be taken into account. The data correction necessary to account for this effect is described in D.3.

It was necessary to design a measurement sequence and arrange the instrumentation so that a maximum amount of data could be obtained during the time available. This time was limited by the capability of maintaining a given inflation level. The measurement sequence has already been referred to. Figure 7 is a block diagram of the measurement system.

4.2 THE DATA

Although Balloon No. 13 was designated as the prime data balloon, data was also obtained for Balloons No. 9 and No. 11. Typical raw data is given in D.6. A single recording represents a change in bistatic angle of 30°, which corresponds to a measurement of 15° of the balloon surface. Two patterns at the same frequency, pressure, and polarization but marked TRANSMIT LEFT and TRANSMIT RIGHT respectively, correspond, together, of a measurement of 30° of the balloon surface.

Given a fixed angular interval, the basic parameters sought were the mean cross-section and some measure of the scintillation about the mean cross-section. From the point of view of the eventual utilization of the balloon as a communications satellite, the ideal parameters would be the mean value of $|H|^2$ and the standard deviation of this quantity about its mean. To compute these values, however, would require a conversion of the data, which is, in its raw form, on a decibel, or logarithmic, scale. Since, in this experiment, the major concern was to relate the radar cross-section in a systematic fashion to the variables of frequency, polarization, and inflation pressure (or more precisely--inflation history) it was felt that no advantage was to be obtained by making this conversion. It was also felt that if sufficiently small angular intervals were chosen, the maximum variation, in decibels, of

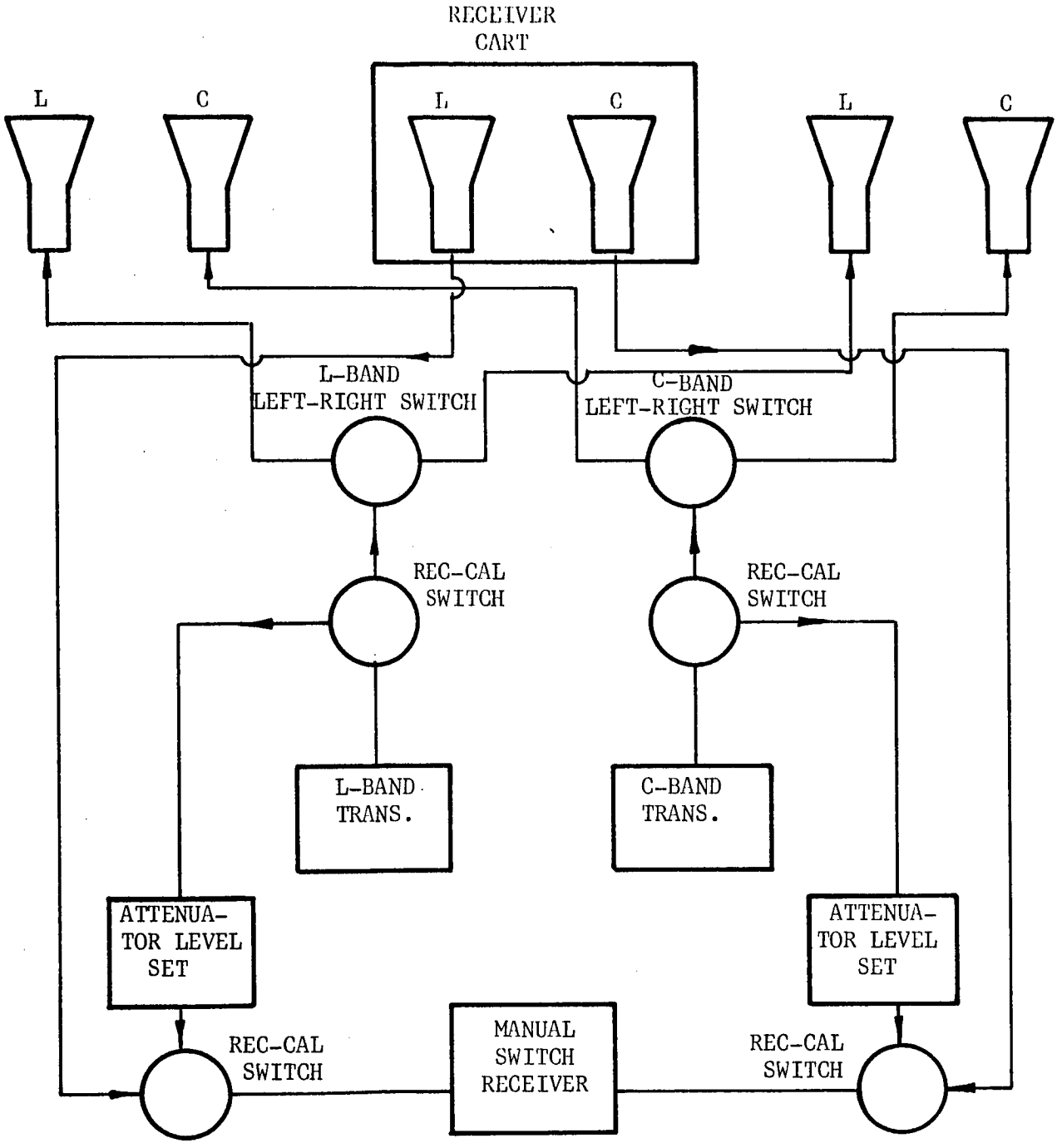

Figure 7 Block Diagram of RF System. Attenuator Levels were Set During Calibration Procedure and the Calibration Verified at Conclusion of Experiment

the cross-section over that interval would be an adequate measure of scintillation properties.

For this reason it was decided to subdivide the 30^{o} of measured surface into six 5^{o} intervals. The mean value of the cross-section of the raw data on each interval was measured, using a planimeter. The near zone correction of 4.5 db was then added, as well as the antenna beam taper correction, which for intervals of this size, was regarded as being constant. The mean was then recorded, in db relative to the nominal cross-section of the balloon. The maximum variation in cross-section for each 5^{o} interval was recorded directly from the raw data.

The results are tabulated in Tables D-1, D-2, and D-3, in Appendix D. The most obvious and striking feature of these tables is the difference in the scintillation level of the side of the balloon containing the reinforced gores for Balloons 11 and 9 on the one hand, and Balloon No. 13, on the other. This is shown by examining the + columns under "0", "5", and "10" for the Nos. 11 and 13 balloon, and the $\bar{+}$ column under "15", "20", and "25" for the No. 9 balloon.

At first glance there seems to be no significant difference in the scintillation level between the measurements at horizontal and vertical polarization. Using Table D-3, for the prime data balloon No. 13, a distribution histogram for the 42 entries was tabulated for the value of the function $10 \log \frac{\sigma_V}{\sigma_H}$, at both L-band and C-band. These histograms are given in Figure 8 and Figure 9.

The C-band distribution (Figure 8) has a mean -.5 db, and is skewed to the negative side. This indicates or is at least consistent with, the hypothsis that at C-band the scintillation level at vertical polarization is either negligibly different or slightly less than the scintillation level at horizontal polarization.

The L-band distribution (Figure 9) has a mean + .25 db, and exhibits little or no skewness. This indicates, or is at least consistent with, the hypothesis that at L-band there is no difference between the scintillation levels at horizontal and at vertical polarizations.

These results indicate that whatever feature of the balloon is creating scintillations about the mean cross-section, it is insensitive to polarization. When one looks casually at the balloon, one sees large numbers of horizontal creases and ridges radiating from the seams. If these creases have any effect on the cross section, it would be in terms of scintillation effects, since their structure and placement is not regular. The very slight sensitivity at C-band to polarization indicates that these creases have a small, but negligibly small, effect on the cross section.

To describe the effect of inflation history on the gore, the Tables D-4 and D-5 were compiled. From these tables it is apparent that once the

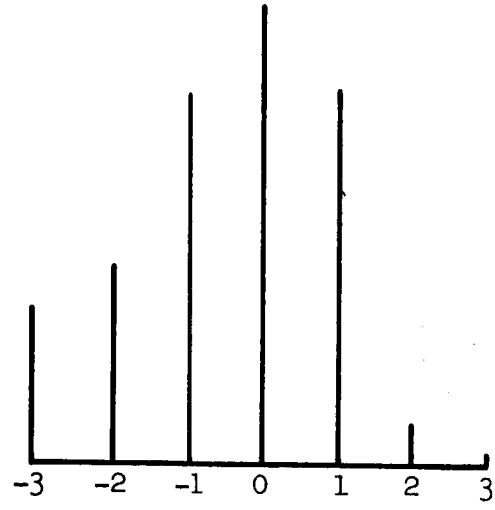

Figure 8 Distribution for 10 log $\frac{\sigma_V}{\sigma_H}$ at C-Band
Mean = - .5

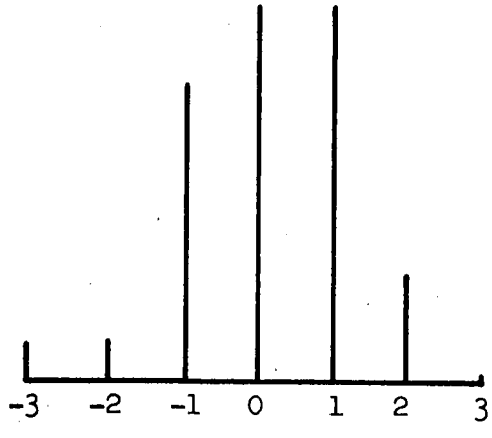

Figure 9 Distribution for 10 log $\frac{\sigma_V}{\sigma_H}$ at L-Band
Mean = .25

balloon has been inflated, the pressure history does not have significant effect on the mean cross-section value. On the other hand, increasing the pressure seems slightly to decrease the scintillation level, and except for one discrepancy (Table D-5, C_H, at final relaxation), after relaxation from 7400 psi, there is less scintillation than after relaxation from 4800 psi; in turn, after relaxation from 4800 psi there is less scintillation than during the initial relaxed condition.

Dividing the numbers in the "m - Summed over other gores" (Table D-4) by 5 is equivalent to finding the mean cross section of the balloon over all the non-reinforced gores. Although the resultant numbers are, with few exceptions between ± 1, nevertheless Table D-3 indicates large variations in the mean value from between one 5^o strip to another. This indicated a need to study the reflectivity patterns on a larger scale to determine effects that would not be observed by breaking the analysis into 5^o sections.

For this purpose, four patterns were selected, all from the non-reinforced side of the balloon. Their descriptions are these.

Pattern Number	Pressure Level	Polarization	Frequency
363	4800 (Relaxed)	H	L
367	4800 (Relaxed)	H	C
385	7400 (Relaxed)	V	L
389	7400 (Relaxed)	V	C

For each pattern the corrected cross section value in db relative to the nominal value was recorded at 10-minute intervals, giving a total of 180 points for the 30^o scale. Calling the ordered sequence of points f(n), n = 1, 2, ... 180, the normalized correlation function

$$C(n) = \frac{\sum_{j=1}^{N-n} f_{j+n} f_j}{\left\{\sum_{j=1}^{N-n} f_j^2\right\}^{1/2} \left\{\sum_{j=n}^{N} f_j^2\right\}^{1/2}}, \quad N = 180$$

was computed. The resulting autocorrelation function was plotted for $10' \leq \beta \leq 15^o\ 10'$, the autocorrelation of the truncated sequence being regarded as meaningless for larger values of β. The results are given in Figure 10. It is clear that the principal parameter to which the autocorrelation curve is sensitive is frequency. At C-band there is a well-defined autocorrelation peak at ~ 5^o and another at ~ 10^o. This corresponds to ~ 2.5^o and 5^o on the balloon. If one examines Figure A-11 and Figure A-12, in Appendix A, which correspond, respectively, to C-band at 4000 and 7000 psi, one finds deep nulls, for the equatorial plane, approximately 1.7^o apart at 7000 psi and just a peak at the center of the pattern,

or equivalently nulls 3.4^{o} apart at 4000 psi. Returning to Figure 10, one finds a peak for the 7800 R curve at 1.7^{o} which does not occur for the 4800 R curve. Thus, the model balloon structure postulated in Appendix A is capable of predicting certain autocorrelation peaks in the radar data, and should be regarded as basically a correct model for the structure of the balloon.

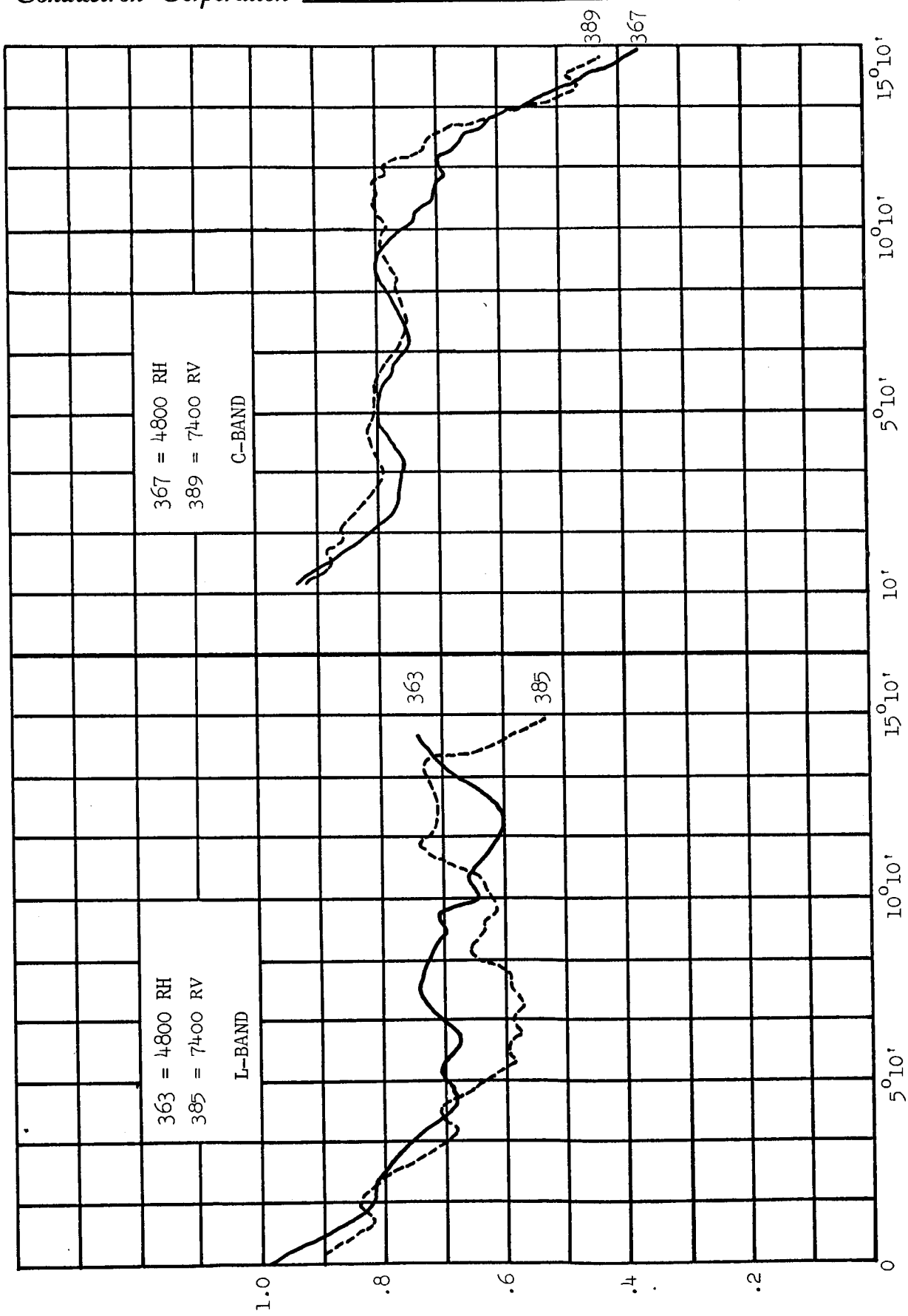

Figure 10 Autocorrelation Curves

5. THE PHOTOGRAMMETRIC MEASUREMENTS

Conductron was supplied, by NASA, photogrammetric measurements of the Echo II balloon taken during the Static Inflation Tests. These measurements were made at several stations meridionally opposite to the side of the balloon on which the radar measurements were being performed. One station covered two unreinforced gores (gores 102 and 103), the other covered two reinforced gores (gores 106 and 1). The pressure levels were 2800, 4800, and 7400 psi.[1] The measurements were first re-reduced to a form which defined the surface to be a perturbed sphere as defined by Equation 14. In Appendix F the results of this reduction are presented, a discussion of the topography as a function of inflation pressure is given, and a method of computation of the physical optics integral is presented. It was felt that although this method would be satisfactory for rough estimates, to obtain the desired accuracy, numerical computation of the physical optics integral was required. The analysis which preceded the numerical computations, as well as the results are given in Appendix G.[2] The curves obtained are given in Figures 11, 12, 13 and 14. All the figures indicate a variation in radar aspect of 20°. Figures 11 and 13 describe the unreinforced gores. Figures 12 and 14 describe the reinforced gores.

From Tables D-4 and G-2 we can make the following comparison between the cross-sections computed via the photogrammetric measurements and the cross-sections that were measured by the radar. Let $\langle\sigma\rangle$ designate the mean cross-section for the unreinforced section (relative to nominal sphere)

f = 5.85 KMC

$\langle\sigma\rangle$ Photogrammetric	$\langle\sigma\rangle$ Measured	PSI	Difference in $\langle\sigma\rangle$
2.35	- 1.25	2800	3.55
- 1.24	.2	4800	- 1.44
- 0.76	- .6	7400	- .16

[1] The photogrammetric data at these levels was adequate to perform the analysis. Data at other levels was supplied, but had too many blank spots for adequate analysis.

[2] The numerical computation consisted, basically, of representing the physical optics integral as a sum; the choice of grid size was 6 inches (the number b defined on page G-4). This choice was to assure accuracy of $\pm$.75 db in the radar cross-section. The computer program was formulated to ensure a round-off error of less than .25 db; the computed results are therefore accurate to within 1 db. See Appendix G for a more complete discussion of this point.

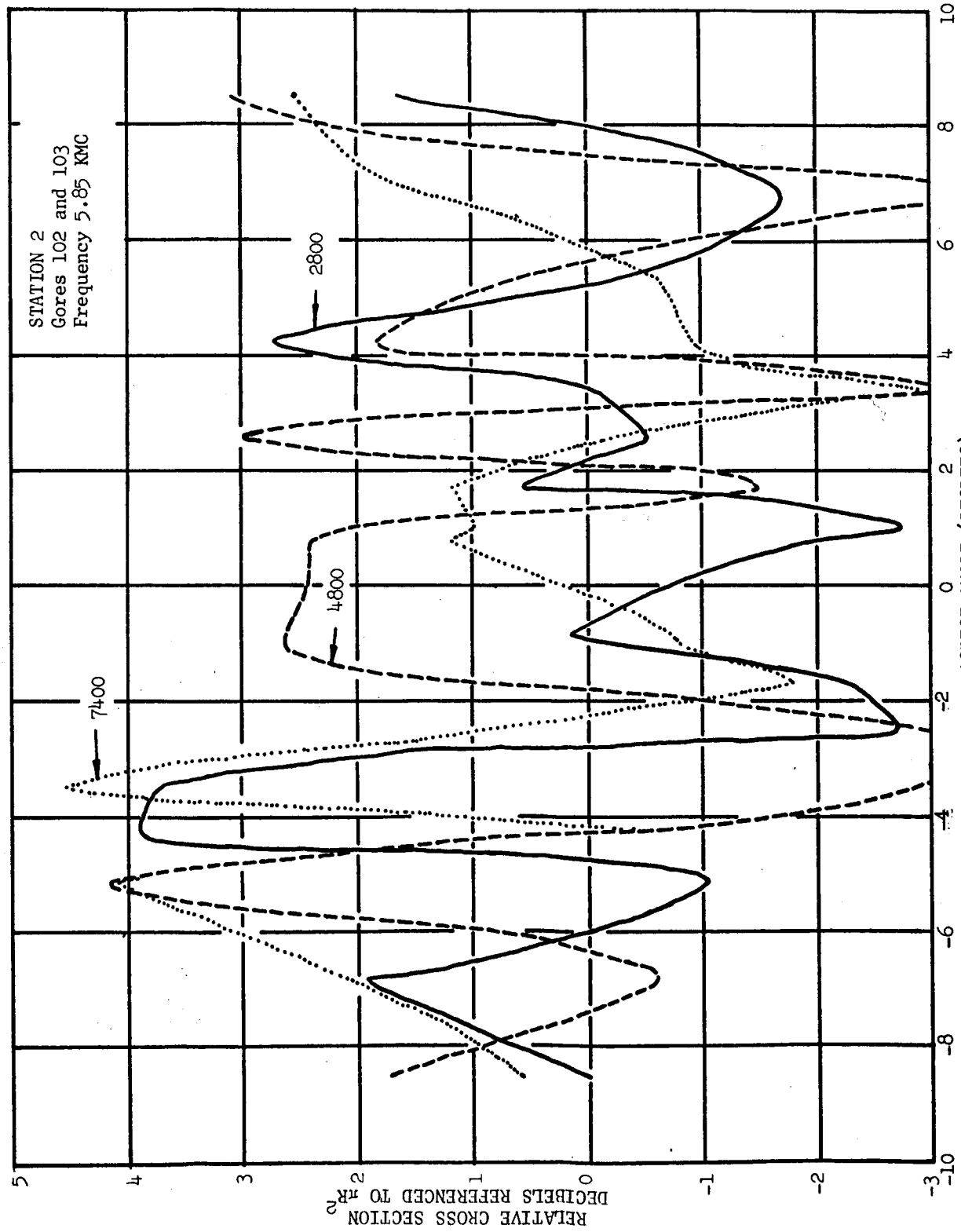

Figure 11 Computed Cross Section from Photogrammetric Measurements Over a 16^0 Aspect Interval

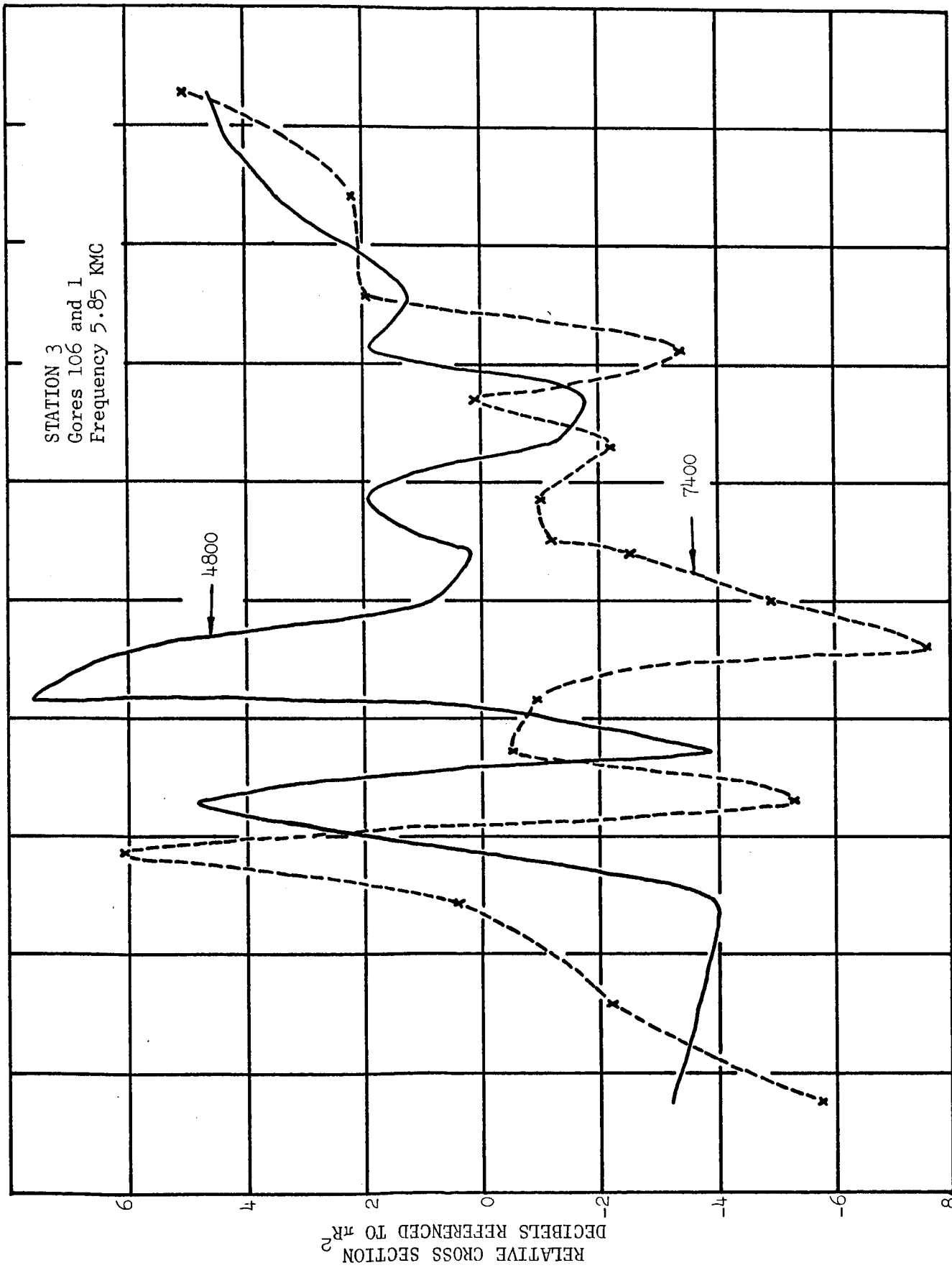

Figure 12 Computed Cross Section from Photogrammetric Measurements Over a 16° Aspect Interval

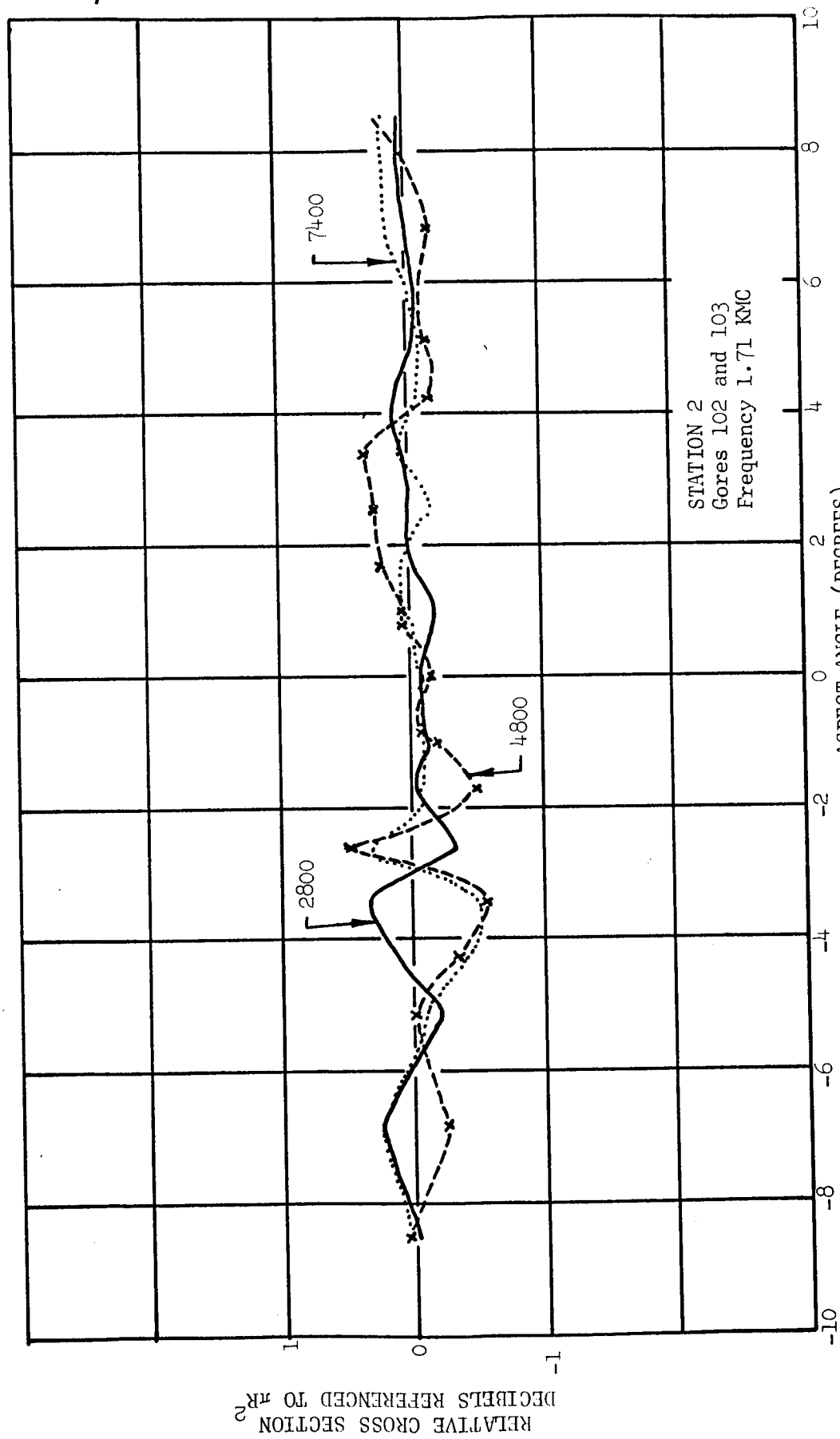

Figure 13 Computed Cross Section from Photogrammetric Measurements Over a 16° Aspect Interval

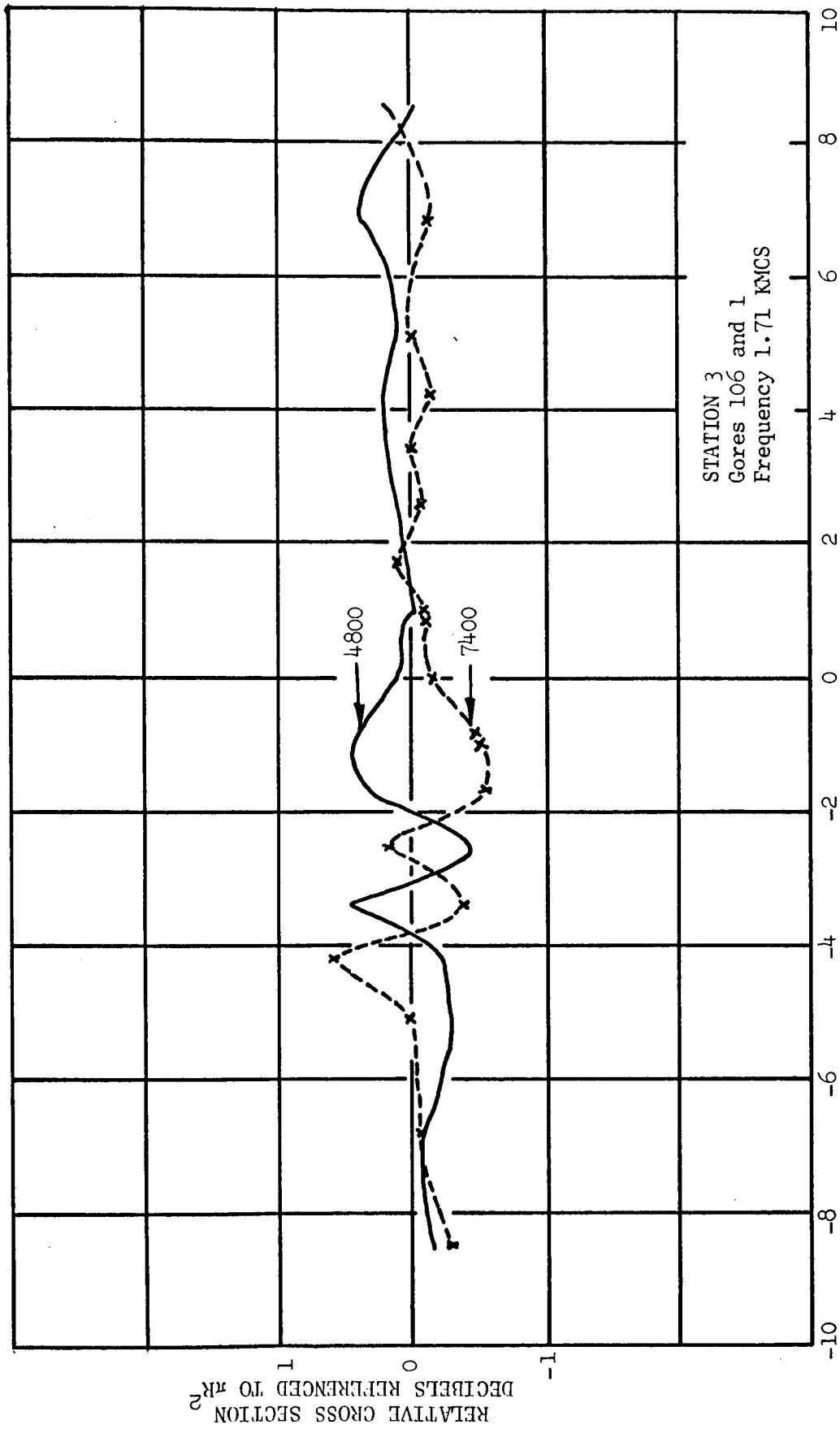

Figure 14 Computed Cross Section from Photogrammetric Measurements Over a 16° Aspect Interval

The discrepancy between these values becomes less as the pressure is increased. This indicates, as might be expected, that as the pressure increases, the basic shape of the balloon (a smooth convex surface) becomes more repeatable as one moves around the balloon, so that the mean cross-sections measured over different parts of the balloon (at the same latitude) become more independent of longitude.

From Figure 12 the values of successive peak-peak scintillations was computed and weighted according to the angular distance between successive peaks; that is, the vertical distance (in db) between an adjacent maximum and minimum was multiplied by the horizontal distance (in angle) between them; these numbers were added and divided by the total angle, giving a weighted average. These weighted averages were computed and designated $\langle \pm \rangle$. From Table D-5 the corresponding $\langle \pm \rangle$ were computed by dividing the sums for the unreinforced gores by 5:

f = 5.85 KMC

$\langle \pm \rangle$ Photogrammetric	$\langle \pm \rangle$ Measured	PSI
5.2	5.4	2800
5.6	4.8	4800
4.6	4.9	7400

It is seen that the scintillation obtained by the calculation of the field from photogrammetric measurements on one side of the balloon does not significantly differ from the scintillation obtained by the radar measurements on the other side of the balloon.

6. RELATIONSHIP TO PHASE "A" PROGRAM

In the first phase of the program 12 ft. circular segments of Echo II material were mounted on a support structure, and the radar cross-section measured at the Conductron Radar Range. The details of that phase have been reported previously [Conductron Report 0038-A-F].

In the first phase program two basic problems were encountered. Conductron's mechanical analysis showed that the balloon segment, when mounted on the support structure, would assume the same configuration, for a given pressure level, as it would in the full scale balloon, except for an annular region extending inwards about 2 ft.[1] from the rim of the "mounting ring", to which the segment was attached (see Figure 15).

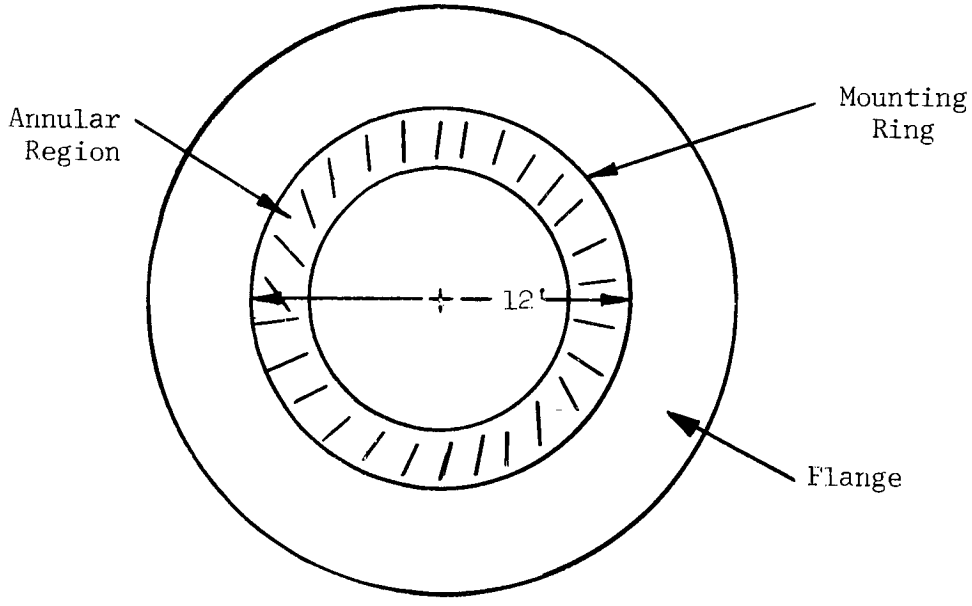

Figure 15

This left at the high pressures, only an 8 ft. diameter sector whose mechanical behavior was the same as it would be on the full scale balloon.

[1] at the higher pressures. At lower pressures, the width of this annulus decreases, according to the formula $d = \sqrt{\epsilon}\ R$, where ϵ is circumferential strain and R is the segment radius.

The second problem was the electrical effect of the flange. The original specification for the flange was that its cross-section be at least 20 db below the nominal return from the balloon. The flange was designed (see Figure 16) to have an elliptical shape and it was predicted to have the desired cross-section.

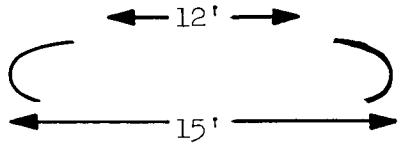

Figure 16 Cross Section of a Flange

During the measurement program, contour measurements were made on the segment, producing topographical maps similar to those found in Appendix F. However, the grid size on these maps precluded an exact calculation of the physical optics integral; at this stage of the investigation, it was not feasible to instrument precise contour measurements. The maps were therefore used to compute radii of curvature, and the predicted cross-section, on the basis of specular scattering theory, was found to be essentially constant.

However, the cross-section data at C-band had a 5-6 db scintillation level, and on this basis it was assumed that the mounting flange was interfering with the measurement, and that the radar cross-section of the flange was between 14 and 18 db below the nominal level of the balloon, rather than the 20 db value for which it had been designed. It is now clear that the 5-6 db scintillation level, which was independent of inflation history, is exactly what would have been predicted on the basis of the second phase program, and that more accurate contour measurements would have revealed this during the first phase program. This also indicates that the flange design had actually met its specifications.

At the conclusion of the first phase of the program, it was felt that the segment measurement techniques could reliably predict the mean cross-section of the balloon as a function of the balloon inflation history. Upon re-examining the first phase measurement program it is seen that both cross-section and scintillation levels are the same as have been consistently found in the Static Inflation Tests.

In the evolution of this program, it has become apparent that in addition to mean radar cross-section and scintillation level, a significant quantity which can be related to the inflation history and to the frequency is the autocorrelation function. On the basis of the work reported in Appendix A, it is seen that for this particular description of balloon behavior, measurements which include at least a three gore sector must be performed. Because in the first phase, the effectively 8 ft. diameter segment (at high pressures) was less, in width, than the three gores advisable

the first phase work must be regarded as inadequate only to predict the auto-correlation data for the full scale balloon. In continuation of this work, it is planned to use a larger balloon segment.

7. SUMMARY AND CONCLUSIONS

The model we have developed for the Echo II balloon is a smooth convex body upon which is superimposed a small surface perturbation. This smooth convex body can itself be regarded as a small perturbation from a sphere (see Figure 17).

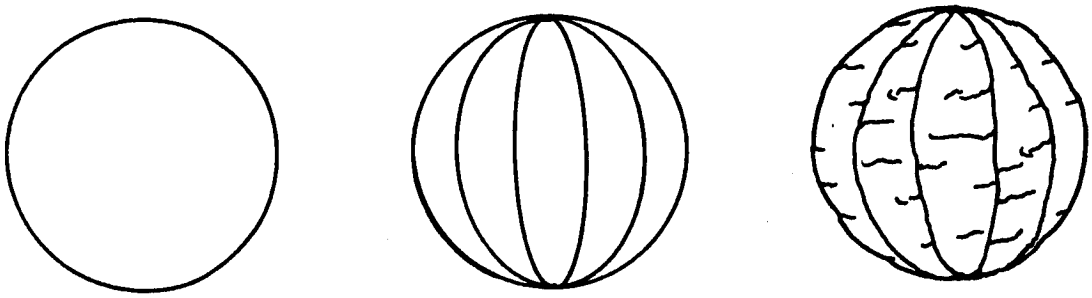

Sphere | Smooth Convex Body (Appendix A) | Echo II (Appendix F)

Figure 17

This final configuration, of course, can be regarded as a perturbation on the original sphere, but it is important to have at hand the smooth convex body model and the small perturbation model, dependent upon what effects are critical.

The systematic changes in the radar cross-section as the illuminating beam moves around the balloon is predicted from the smooth convex body. If the gores are identical, the field contributions from three gores are adequate to determine the radar cross-section. This model can be used to predict the autocorrelation peaks of cross-section as a function of viewing angle.

The methods of physical optics are adequate to describe the perturbation model. In particular, the scintillation levels are in close agreement with experiment.

Although the model developed in Appendix A is predictive of the autocorrelation peaks, the mean cross-sections and peak-peak scintillations for that model differ significantly from the values obtained in the Phase A segment measurements and the static inflation tests. This means that although the basic geometry is correct, the numerical values of the parameters determined by the mechanical analyses provided Conductron by NASA are incorrect. The fact that the model was predictive of the autocorrelation peaks

means that the latitudinal radius of curvature estimate was correct. Because the mean cross-sections computed from the model are uniformly higher than those observed on Echo II, the longitudinal radius of curvature for the model is too large. The balloon "flattening" effect derived in Appendix C would cause a reduction in this radius of curvature in the equatorial region, and thereby account for the discrepancy between computed and measured values of the cross section.

It is planned, in the near future, to conduct some more segment measurements at the Conductron Radar Range and another Static Inflation Test. The segments will be sufficiently large so that the resultant scattered field of at least three gores will be obtained. The data will then be used to predict the results of the static inflation test, on the basis of the work performed in the present phase. This will serve both as a verification of the theories and techniques developed, so far, in this program and a demonstration of an effective tool to predict satellite radar performance.

APPENDIX A

A.1 INTRODUCTION

This report consists of the theoretical calculation of the scattering properties of a hypothesized perfectly conducting geometric configuration. The configuration consists of 106 gores and two end panels, arranged, in the fashion of the Echo II balloons, to form a nominal sphere of radius a = 20.6 meters. The exact shape of these gores was to be determined by using data given in two reports:

"Structural Analysis of Echo II to Predict the Surface Configurations," Fairchild Stratos Corporation, Final Report, Contract NAS-5-2365, January 1963, and

"Structural Analysis of Echo II," Astro Research Corporation, Interim Report No. 1, NAS 5-3229, May 1963.

The emerging hypothecated geometry is the following: If one stays away from the polar caps, which are not studied in these reports, each gore can be represented by two coordinates (S_1, S_2), S_1 representing distance along the gore in the longitudinal direction, S_2 representing distance along the gore in a direction orthogonal to the longitudinal direction. (see Figure A-1)

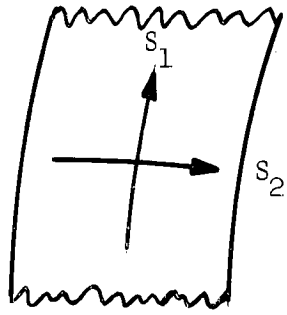

Figure A-1

The curves S_2 = constant are plane curves, the planes being mutually orthogonal, and the normal to the surface at the intersection of two such curves is orthogonal to the plane of their tangent vectors.

For fixed S_1, the form of the resulting curve was obtained from the data in the above mentioned reports, and depended, of course, on the assumed surface stress. The surface stresses chosen were 500, 4000, 7000, and

12,000 psi. These stresses correspond, respectively, to surface forces of .18, 1.44, 2.52, and 4.32 lb/in. The Astro Data, taken at forces of 1.72, 2.66, 4.05 lb/in was extrapolated graphically to obtain the data corresponding to the forces we had chosen.

It was found that the corresponding curves could be fit with a parabola, of very nearly constant curvature; the corresponding mathematical representation was chosen to be a circular arc of radius A, where the ratio $\gamma = \frac{A}{a}$ had the values 22, 3, 1.7, 1, corresponding to the given pressures.

In Section A.2 below, we derive the formulas to be used to find the scattering cross section of this idealized structure, and in Section A.3 we find numerically the cross-section for values of γ, $\gamma = \infty$, $\gamma = 3$, $\gamma = 1.7$. We do not bother with $\gamma = 1$, for this is the perfect sphere. It shall be seen that the solution is in the form of a Fresnel integral, and it is elementary to see, from the asymptotic form of the integral, that $\gamma = \infty$ is a valid approximation for $\gamma = 22$. The scattering considered is bistatic, the transmitter being in the direction of the unit vector $\hat{u}_T$, the receiver in the direction of the unit vector $\hat{u}_R$.

It is a temptation to use, a priori, the bistatic theorem, which replaces the problem of bistatic scattering with the problem of monostatic scattering, in the direction

$$\hat{u}_o = \frac{1}{2 \cos \beta} (\hat{u}_T + \hat{u}_R),$$

where the bistatic angle, 2β, is defined by

$$\cos 2\beta = \hat{u}_T \cdot \hat{u}_R.$$

This theorem is an exact theorem, but it does not apply to bodies with discontinuous tangent planes or edges; further, it is a limit theorem, being a statement of what happens as $k = \frac{2\pi}{\lambda} = \frac{f}{c} \to \infty$.

Since we shall deal here with two frequencies f = 1.71 KMC and f = 5.85 KMC, the second condition does not apply; the trouble is that the Fresnel integrals involved, except in the case of $\gamma = \infty$, are not close enough to their limiting forms. The first condition is intrinsically more serious, however. For bistatic ($\beta \neq 0$) scattering, there is a cross-polarization term, which is not present in monostatic scattering.

Fortunately, the errors introduced by replacing the bistatic by the monostatic problem are proportional to sin β and to sin ψ_o, where ψ_o is a parameter, to be described later which is small. The errors turn out to be negligible, in terms of the criterion that if the field quantities are represented in the form $\vec{H}(1 + \delta)$, then $|\delta|$ must be less than .08. This criterion guarantees accuracy in the cross-section of $\pm$ 1 db. In the following section, approximations will be made to simplify the relevant calculations. These approximations have to do with discarding terms which are proportional to either product sin ψ_o sin β or $\alpha_o = \frac{\pi}{106}$; the resulting errors total less than the required .08.

In Section A.3 we evaluate the relevant integral, and obtain graphs of the cross section as one moves across a gore. These results are valid for any bistatic angle, 2β, $\leq 30^{\circ}$, and have been computed for azimuth angles for $\hat{u}_o$, $-\frac{\pi}{2}$, $\frac{\pi}{4}$, and $\frac{\pi}{6}$.

A.2 SCATTERING BY A GORE

Let the gore have the equation,

$$\vec{r} = \vec{r}\,(S_1, S_2),$$

where S_j, $j = 1, 2$ are the arc lengths of the orthogonal coordinate curves. The full variation of S_1 is the longitudinal perimeter of the gore, which is approximately πa; for each S_1, S_2 varies over the interval $-\frac{S}{2}, \frac{S}{2}$, in which S, of course, depends on S_1. The coordinate curves are plane curves, having the unit tangent vectors,

$$\hat{T}_j\,(S_1, S_2) = \hat{r}_{S_j}\,(S_1, S_2),\ j = 1, 2$$

and have curvatures K_j, which will be assumed to be constant and having the values $\frac{1}{a}$, $\frac{1}{A}$, where $A^j \geq a$. The Frenet-Seret formulas are

$$\frac{\partial \hat{T}_j}{\partial S_j} = -K_j\,\hat{n},\quad \frac{\partial\,\hat{n}}{\partial S_j} = +K_j\,\hat{T}_j,\ j = 1, 2$$

and

$$\hat{n} = \hat{T}_2 \times \hat{T}_1.$$

To compute the scattered field, it is assumed that the currents induced by the incident field are given by the physical optics approximation, valid for large a,

$$-2\,\vec{H}^{(i)} \times \hat{n},$$

where $\vec{H}^{(i)}$ is the incident magnetic field. The transmitter will be assumed to be located in the direction of the unit vector $\hat{u}_T$, and the receiver in the direction of the unit vector $\hat{u}_R$. The bistatic angle 2β, is defined by

$$\cos 2\beta = \hat{u}_R \cdot \hat{u}_T,$$

and the unit vector $\hat{u}_o$ is defined by

$$\hat{u}_o = \frac{1}{2\cos\beta}\,(\hat{u}_R + \hat{u}_T).$$

The polarization of the incident field is given by the unit vector $\hat{p}$, where $\hat{p} \cdot \hat{u}_T = 0$. Then the scattered field $\vec{H}^{(s)}$ is given by the physical optics formula. The normalized scattered field, $\vec{H}$, defined by

$$\vec{H} = \sqrt{4\pi R^2}\ e^{-ikR}\,\vec{H}^{(s)},$$

is then, for large R, described by

$$\vec{H} = \frac{ik}{\sqrt{\pi}} \iint e^{-2ik\cos\beta \hat{u}_o \cdot \vec{r}} (\hat{n} \times \hat{p}) \times \hat{u}_R \, dS,$$

the integral being extended over the illuminated portion of the gore.

Because there is always a value of S_1 for which $\hat{u}_o \cdot \vec{r}_{S_1} = 0$, the above integral can be evaluated by regarding it as an iterated integral, and integrating first with respect to S_1 by the method of stationary phase (justified because ka is $\gg 1$), we obtain

$$\vec{H} \sim ie^{\pi i/4} \sqrt{\frac{ka}{\cos\beta}} \int_{-\frac{S}{2}}^{\frac{S}{2}} dS_2 \left[\frac{e^{-2ik\cos\beta \hat{u}_o \cdot \vec{r}(S_1^*, S_2)}}{\sqrt{\hat{u}_o \cdot \hat{n}\,(S_1^*, S_2)}} [\hat{n}\,(S_1^*, S_2) \times \hat{p}] \times \hat{u}_R \right]$$

S_1^* is the point for which $\hat{u}_o \cdot \vec{r}_{S_1}(S_1^*, S_2) = 0$, and is independent of S_2. Hence we can regard S_1^* as a constant in the evaluation of the integral. The geometry of the curve

$$\vec{r} = \vec{r}\,(S_1^*, S_2)$$

is demonstrated in Figure A-2.

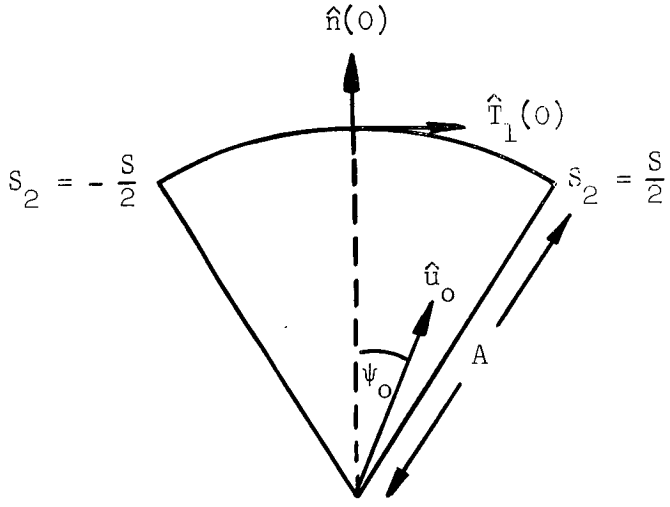

Figure A-2

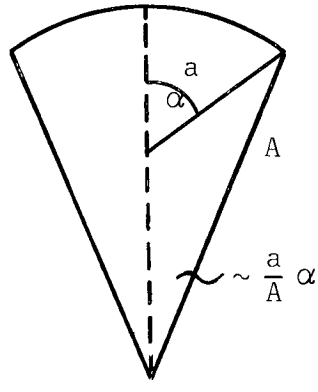

Figure A-3

The vector $\hat{u}_o$ lies in the plane of the curve (because $\hat{u}_o \cdot \hat{T}_2 = 0$), which is an arc of a circle with radius A. In Figure A-3, the relationship of this circle to the radius of the nominal sphere, a, and the angle α is shown. $\alpha = \frac{\pi}{106} \sin\theta_o$, where θ_o is the aximuth angle of $\hat{u}_o$. [$\theta_o = \frac{\pi}{2}$ corresponds to $\hat{u}_o$ lying in the equatorial plane.] Numerically,

$$\frac{S}{2} = A \sin^{-1}\left[\frac{a}{A}\alpha\right] \sim a\,\alpha$$

Now, using the Frenet-Seret formulas, we obtain

$$\vec{r}(S_2) = \vec{r}(0) + \hat{T}_1(0)\, S_2 - \frac{1}{2A}\hat{n}(0)\, S_2^2 + \ldots$$

$$\hat{n}(S_2) = \hat{n}(0) + \frac{\hat{T}_1(0)}{A} S_2 + \ldots$$

From Figure A-2 it is clear that $\hat{u}_o \cdot \hat{n}(0) = \cos\psi_o$, $\hat{u}_o \cdot \hat{T}_1(0) = \sin\psi_o$, and from Figure A-3,

$$\vec{r}(0) = [a\cos\alpha + A\,(1 - \cos\tfrac{a}{A}\alpha)]\,\hat{n}(0) \sim a\,\hat{n}(0).$$

Therefore, the integral can be approximated

$$\vec{H} \sim i\, e^{\pi i/4}\sqrt{\frac{ka}{\cos\beta}}\; e^{-2ika\cos\beta\cos\psi_o} \int_{-\frac{S}{2}}^{\frac{S}{2}} dS_2$$

$$\frac{e^{i2ka\cos\beta\left[\frac{\cos\psi_o}{A}S_2^2 - 2\sin\psi_o S_2\right]}}{\sqrt{\cos\psi_o + \frac{S_2}{A}\sin\psi_o}} \left[\left[\hat{n}(0) + \frac{\hat{T}_1(0)}{A}S_2\right] \times \hat{p}\right] \times \hat{u}_R$$

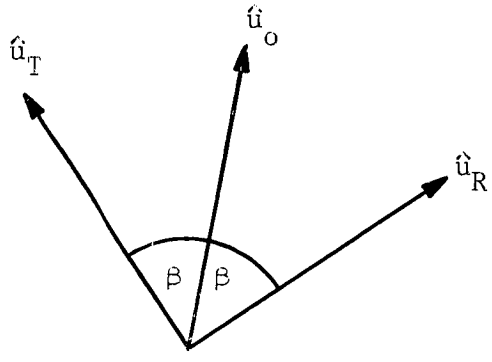

Figure A-4

Figure A-4 illustrates the configuration of $\hat{u}_o$, $\hat{u}_T$, and $\hat{u}_R$. There are two independent orientations for the polarization vector $\hat{p}$. The first is perpendicular to the plane of the three vectors, $\hat{p}^{(1)}$, corresponding to horizontal electric polarization. For an arbitrary vector $\hat{v}$,

$$[\hat{v} \times \hat{p}^{(1)}] \times \hat{u}_R = (\hat{u}_R \cdot \hat{v})\, \hat{p}^{(1)},$$

which leaves the polarization unchanged. In particular, if $\hat{v} = \hat{n}(0)$, because $\hat{u}_T$ lies on a cone of half-angle β about $\hat{u}_o$,

$$\cos\beta\cos\psi_o - \sin\beta\sin\psi_o \leq (\hat{u}_R \cdot \hat{n}_o) \leq \cos\beta\cos\psi_o \sin\beta\sin\psi_o$$

If $0 \leq \beta \leq 15^o$ and $0 \leq \psi_o \leq 7\text{-}1/2^o$, we may take

$$(\hat{u}_R \cdot \hat{n}_o) \sim \cos\beta\cos\psi_o,$$

so that the vector cross product term in the integrand can be replaced by

$$\cos\beta\cos\psi_o\, \hat{p}_1 + 0\left(\frac{S_2}{A}\right).$$

The other orientation, corresponding to vertical electric polarization is

$$\hat{p}^{(2)} = (\hat{u}_T \times \hat{p}^{(1)}).$$

For arbitrary $\hat{v}$,

$$(\hat{v} \times \hat{p}_2) \times \hat{u}_R = [\hat{v} \times (\hat{u}_T \times \hat{p}^{(1)})] \times \hat{u}_R$$
$$= [(\hat{v} \cdot \hat{p}^{(1)})(\hat{u}_T \times \hat{u}_R) - (\hat{v} \cdot \hat{u}_T)(\hat{p}^{(1)} \times \hat{u}_R)].$$

The second vector corresponds to vertical electric polarization, whereas the first corresponds to $\hat{u}_T \times \hat{u}_R = \sin 2\beta\, p_1^{(1)}$, a cross polarization term. If $\hat{v} = \hat{n}(0)$, as above $(\hat{v} \cdot \hat{u}_T) \sim \cos\psi_o \cos\beta$, and since $\hat{p}_1$ is orthogonal to $\hat{u}_o$ and $\hat{n}(0)$ makes an angle ψ_o with $\hat{u}_o$, $(\hat{v} \cdot \hat{p}^{(1)}) \leq |\sin\psi_o|$.

With this approximation, the cross-product term in the integrand is

$$+ \cos\beta\cos\psi_o\, (\hat{u}_R \times \hat{p}^{(1)}) + 0\left(\frac{S_2}{A}\right).$$

Now neglecting terms $0(\frac{S_2}{A})$ in the slowing varying part of the integrand, and suppressing the polarization vector, and suppressing the factor $i\, e^{\pi i/4}$, we obtain

$$\vec{H} \sim e^{-2ikacos\beta cos\psi_o} \sqrt{kacos\beta cos\psi_o} \int_{-\frac{S}{2}}^{\frac{S}{2}} e^{ikcos\beta\left[\frac{cos\psi_o}{A} S_2^2 - 2sin\psi_o S_2\right]} dS_2.$$

For the values $0 \leq \beta \leq 15^{\circ}$, $0 \leq |\psi_o| \leq 7.5^{\circ}$, a final approximation, suppressing the constant phase term:

$$H \sim \sqrt{ka} \int_{-\frac{S}{2}}^{\frac{S}{2}} e^{ik\left[\frac{S_2^2}{A} - 2\psi_o S_2\right]} dS_2.$$

Now, letting $\frac{S}{2} = a\,\alpha$, $\xi = \frac{S_2}{a}$, and defining

$$\gamma = \frac{A}{a} \quad (\gamma \geq 1),$$

we obtain

$$\frac{\vec{H}}{\sqrt{\pi a^2}} \sim \sqrt{\frac{ka}{\pi}} \int_{-\alpha}^{\alpha} e^{ika\left[\frac{\xi^2}{\gamma} - 2\psi_o\,\xi\right]} d\xi.$$

A.3 NUMERICAL DETERMINATION OF THE CROSS-SECTION

We have seen that the normalized field, $\vec{H}$, scattered by a single gore is given by

$$\frac{\vec{H}}{\sqrt{\pi a^2}} \sim \sqrt{\frac{ka}{\pi}} \int_{-\alpha}^{\alpha} e^{ika\left[\frac{\xi^2}{\gamma} - 2\psi_o\,\xi\right]} d\xi,$$

where a is the nominal balloon radius, $\gamma = \frac{A}{a}$, and $\alpha = \frac{\pi}{106} \sin\theta_o$, where θ_o is the azimuth angle of the vector $\hat{u}_o$, and ψ_o is the angle between $\hat{u}_o$ and the normal to the center of the gore. To obtain the field scattering by the balloon, as $\hat{u}_o$ "moves across" a gore, i.e., $-\alpha \leq \psi_o \leq \alpha$, this expression must be evaluated, not only for this range of values for ψ_o, but also for the ranges, $-3\alpha \leq \psi_o \leq -\alpha$, $\alpha \leq \psi_o \leq 3\alpha$, etc., representing the returns from adjacent gores, the results (in general, complex) must be added, and the square of the absolute value of the sum must be computed to obtain the balloon cross-section relative to the cross-section of the nominal sphere.

A.3.1 "Flat" Gores

The first case to be considered is the one in which the gores are "flat", or, equivalently, $\gamma = \infty$. Here, the above expression can be integrated in an elementary fashion, obtaining:

$$\frac{\vec{H}}{\sqrt{\pi a^2}} \sim 2\sqrt{\frac{ka}{\pi}}\;\alpha\left(\frac{\sin(2ka\,\alpha\,\psi_o)}{2\,ka\,\alpha\,\psi_o}\right)$$

which is the well-known return from a circular cylinder.

The computations are elementary. We have performed them at frequencies 1.71 KMC, 5.85 KMC, and for values of θ_o, $\frac{\pi}{2}$, $\frac{\pi}{4}$, and $\frac{\pi}{6}$. The results of these computations are illustrated in Figures A-5, A-6, A-7, and A-8. The infinite null observed in the equatorial plane at 5.85 KMC (Figure A-8) is caused by the null in the field pattern within the interval $-\alpha \leq \psi \leq \alpha$. The critical frequency, below which this does not happen is determined by the equation

$$2\ ka\ \alpha^2 = \pi,$$

which for the present case gives $f_c = 3.9$ KMC.

A.3.2 Finite Values of γ

Although the preceding case, $\gamma = \infty$, is an extreme limit, we shall see that the answers obtained are not remarkably different than for relatively small values of γ. For finite values of γ, by completing the square of the quadratic term in the exponential, and making the substitution

$$z = \sqrt{\frac{ka}{\gamma}}\ (\xi - \gamma\ \psi_o),$$

the integral can be written as

$$\frac{H}{\sqrt{\pi a^2}} \sim \sqrt{\frac{\gamma}{\pi}}\ e^{-ika\gamma u_o^2} \int_{-\sqrt{\frac{ka}{\gamma}}(\alpha + \gamma\ \psi_o)}^{\sqrt{\frac{ka}{\gamma}}(\alpha - \gamma\ \psi_o)} d^{iz^2}\ dz.$$

Let

$$X = \sqrt{ka\ \gamma}\ \ \psi_o$$

$$V = \sqrt{\frac{ka}{\gamma}}\ \alpha.$$

Then

$$\frac{H}{\sqrt{\pi a^2}} \cong \sqrt{\frac{2\gamma}{\pi}}\ e^{-iX^2} \sqrt{\frac{\pi}{2}} \int_{X+V}^{X-V} e^{iz^2}\ dz,$$

in which the integral is a Fresnel integral. For the frequencies under consideration and for the given value of a, the possible range of values of V is $0 \leq V \leq 1.5$, and the possible range of values of X is $0 \leq X \leq \infty$. Using the well-known asymptotic representation:

$$\sqrt{\frac{\pi}{2}} \int_o^x e^{iz^2}\ dz \sim 1 - \frac{i\ e^{ix^2}}{\sqrt{2\ \pi\ x}},$$

it is easy to verify that if V is in the stated range, the integral becomes negligible in comparison to its value at $X = 0$, when $X \geq 5$. Because, given k, a, γ and X, ψ_o is determined, this allows one to estimate how many gores are necessary to take into account to determine the total field. As either

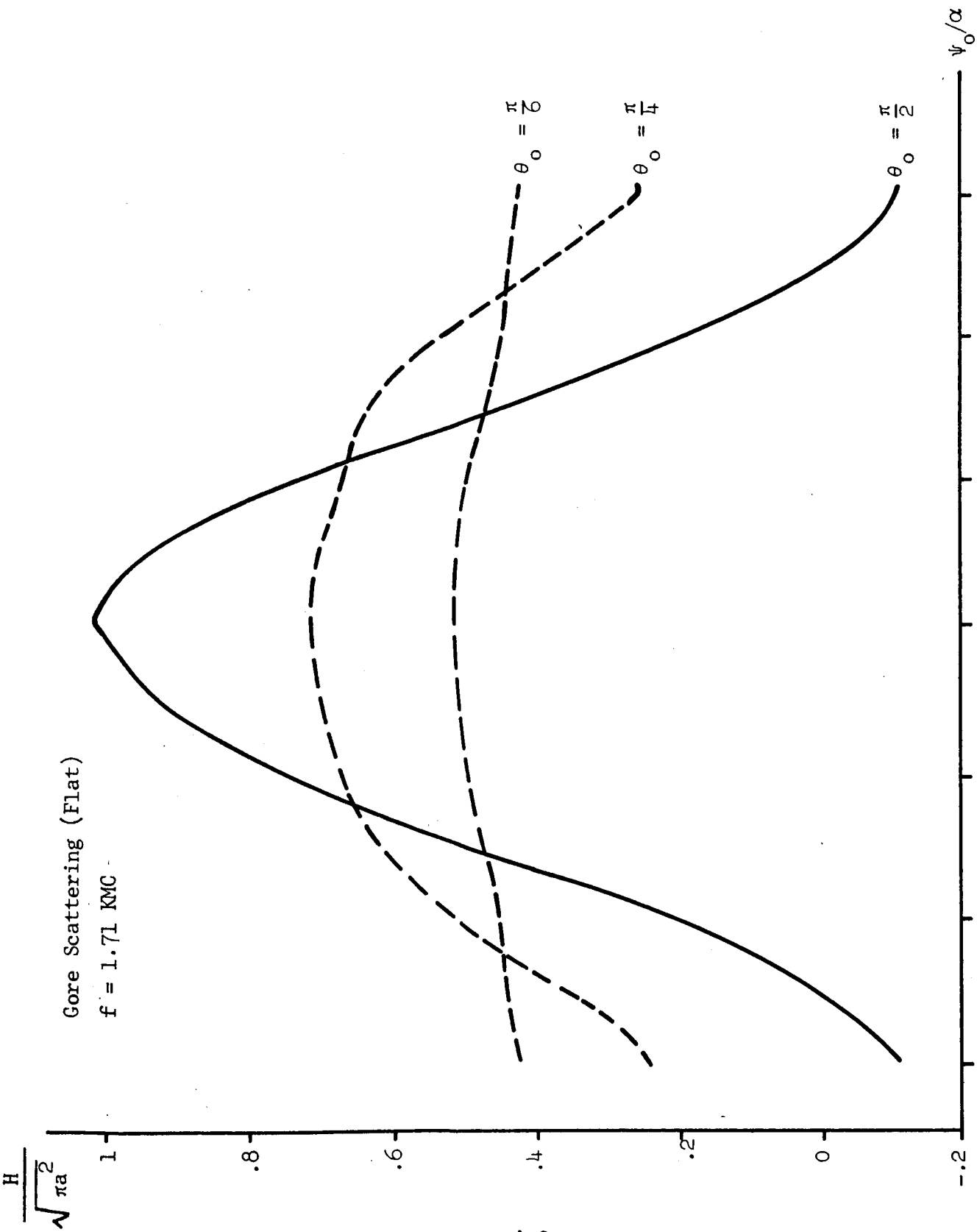
Gore Scattering (Flat)
f = 1.71 KMC
$\frac{H}{\sqrt{\pi a^2}}$
1
.8
.6
.4
.2
0
-.2
-3
-2
-1
0
1
2
3
ψ_o/α
$\theta_o = \frac{\pi}{2}$
$\theta_o = \frac{\pi}{4}$
$\theta_o = \frac{\pi}{6}$

Figure A-5

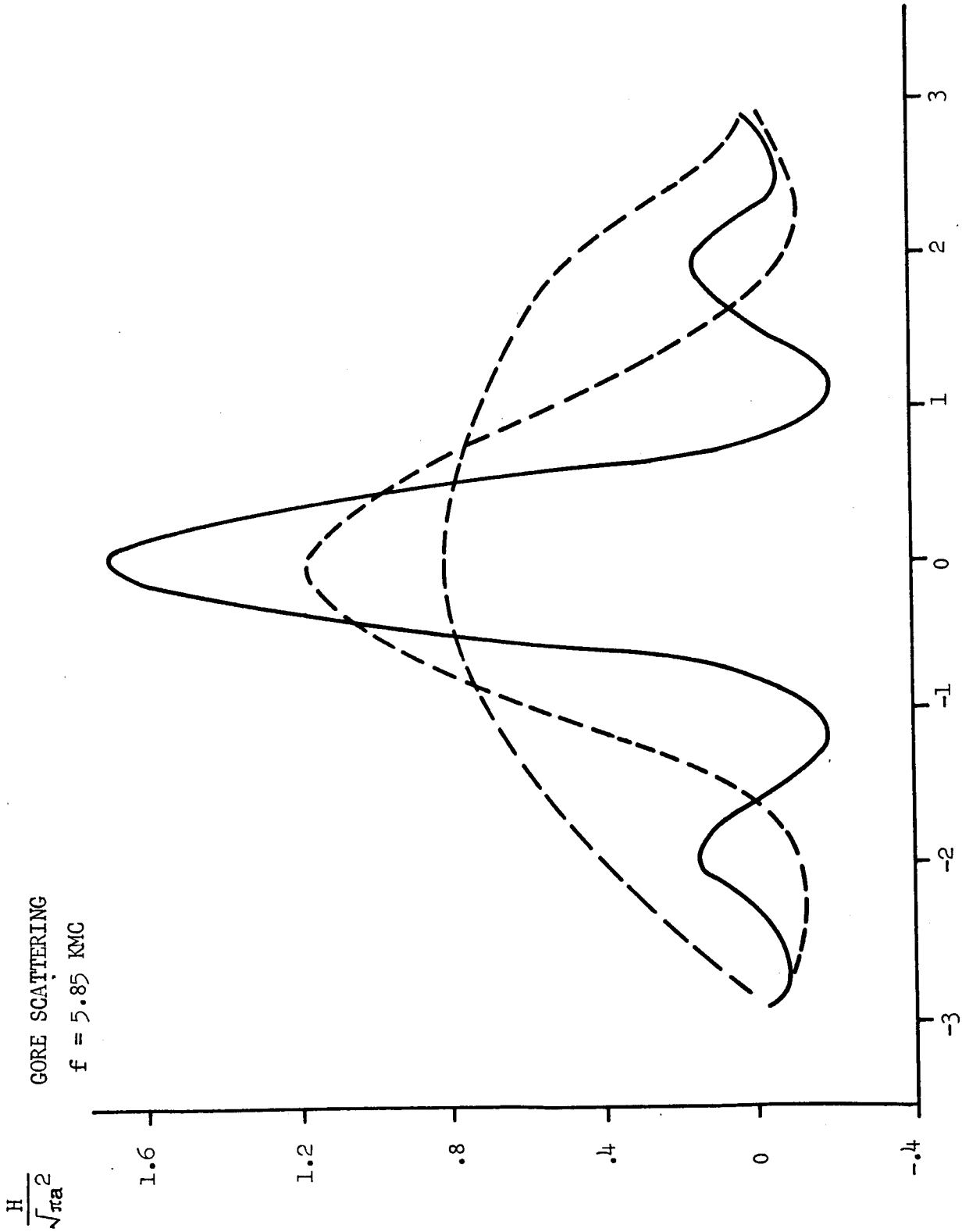

Figure A-6

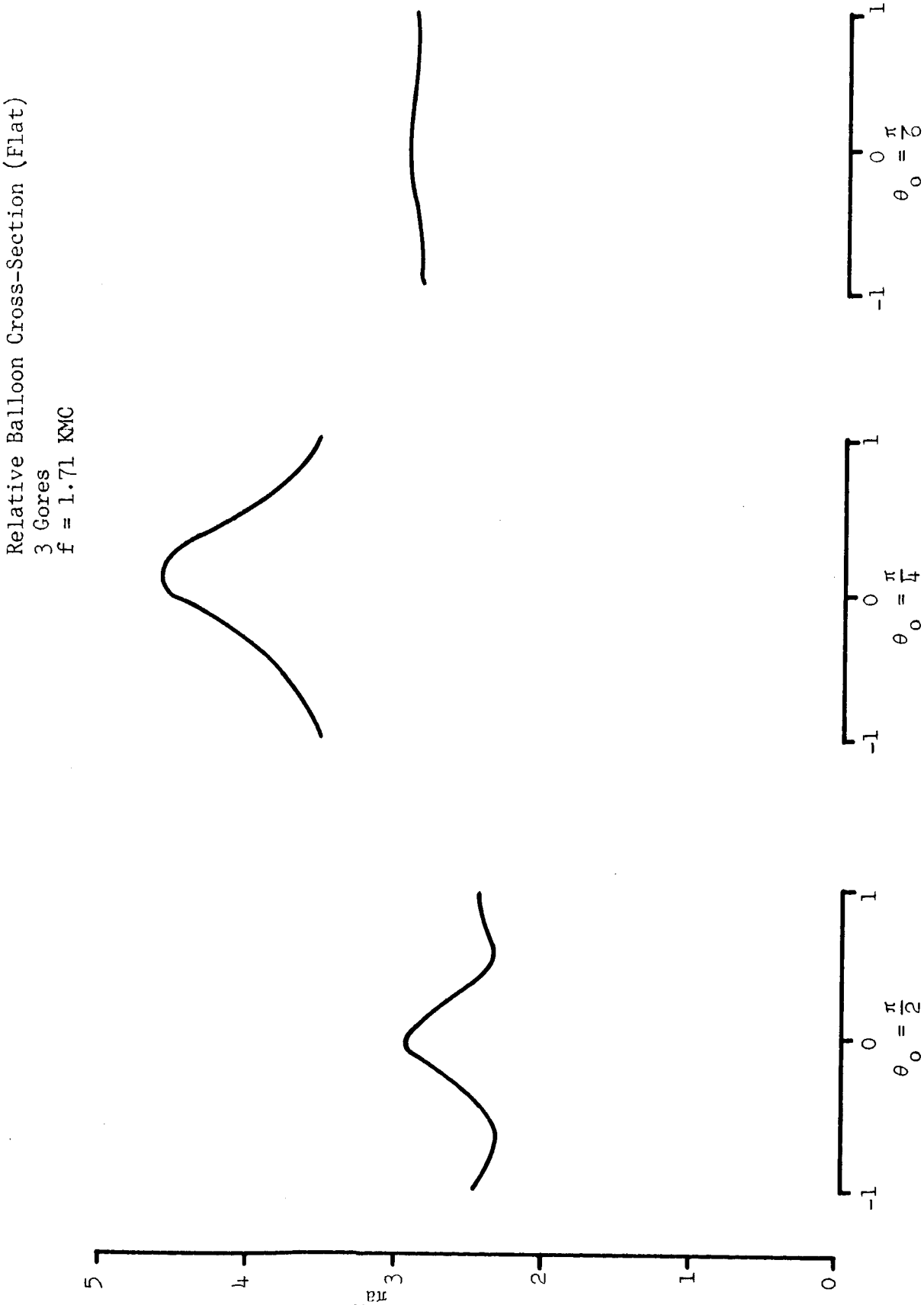
Relative Balloon Cross-Section (Flat)
3 Gores
f = 1.71 KMC
10 log σ / πa²
0
1
2
3
4
5
-1
0
1
θo = π/2
θo = π/4
θo = 0

Figure A-7

Relative Balloon Cross-Section (Flat)
3 Gores
f = 5.85 KMC
10 log σ/πa²
10
5
0
-5
-10
-15
-20
θo = π/2
θo = π/4
θo = 0
1
0
-1
ψo/α

Figure A-8

γ or k the frequency increases, the maximum number of necessary gores decreases. Table A-1 has been computed, using standard tables of Fresnel integrals, correct to the second significant figures, and, with interpolation, can be used to evaluate the fields in question both for the present values of the parameters and for others.

TABLE A-1

$$e^{-ix^2}\sqrt{\frac{\pi}{2}}\int_{X-V}^{X+V} e^{iz^2}\,dz$$

X \ V	.2	.4	.6	.8	1	1.2	1.4
0	.32	.64	.94+.12i	1.22+.23i	1.44+.48i	1.56+.78i	1.5 +.50i
.2	.32						
.4		.61-.02i					
.6			.72+.10i				
.8				.43+.14i			
1	.30	.57+.04i	.74+.08i	.79+.07i	.74+.07i		
1.2						.44-.6i	
1.4							.44-.86i
2	.27+.06i	.21+.16i	.11-.12i	.11-.12i	-.48i	.16-.18i	-.18-.35i
3	.22-.08i	.19+.05i	-.17	-.36+.04i	-.15+.18i	-.2	0
4	.19	.12	.10	0	.20i	0	0
5	-.01+.18i	0	0	.14	0	0	0

Using this table, the following values of the field have been computed, for values of ψ_o/α indicated.

f = 1.71, γ = 1.7

$\theta_o = \frac{\pi}{2}$		$\theta_o = \frac{\pi}{4}$		$\theta_o = \frac{\pi}{6}$	
$\frac{\psi_o}{\alpha}$	$H/\sqrt{\pi a^2}$	$\frac{\psi_o}{\alpha}$	$H/\sqrt{\pi a^2}$	$\frac{\psi_o}{\alpha}$	$H/\sqrt{\pi a^2}$
0	1 +.1 i	0	.7	0	.5
.57	.8+.1 i	.57	.7	.57	.5
.94	.8+.1 i	1.35	.7	1.94	.5
1.9	.1+.1 i	2.7	.2+.2 i	3.8	.2+.1 i
2.8	-.2	4	.2	5.8	.2
3.8	.2	5.35	.1	7.7	.2

f = 1.71, γ = 3

0	. +.7 i	0	.7	0	.4
.33	.8	.33	.7	.33	.4
.71	.8	1	.6	1.44	.4
1.42	.1+.1 i	2	.3+.1 i	2.4	.4
2.12	0	3	.3	4.25	.3
2.85	.3	4	.1	5.8	.3

f = 5.85, γ = 1.7

0	1.6+.6 i	0	1.3+.2 i	0	.9+.1 i
.57	.6+.2 i	.57	.9+.1 i	.57	.7+.1 i
.6	.1-.3 i	.72	.8+.1 i	1	.7
1.03	-.2+.1 i	1.45	.1-.1 i	2	.1+.1 i
1.55	.1 i	2.2	-.4	3	-.2
2.06	0	2.3	0	4	-.2
		3.2	.1	5	0

f = 5.85, γ = 3

0	1.8+.4 i	0	1.2+.1 i	0	1
.33	1.2+.3 i	.33	1 +.1 i	.33	.8
.39	1.1+.1 i	.55	1 +.1 i	.78	.8
.78	.1-.3 i	1.1	-.3	1.55	.3+.1 i
1.17	-.4	1.63	.3	2.42	.9
1.56	0	2.4		3.1	.1
1.95	.1				

Because the fields are complex, to use these tables it is necessary to consider the real and imaginary parts of the fields separately, but except for this, the computation is routine. The results of combining all significant contributions are given in Figures A-9, A-10, A-11, and A-12. Comparison with the results obtained for $\gamma = \infty$, indicates some changes, but qualitatively, the results are similar. To see how the field pattern differs from its limiting form, a comparison between the scattering from a single gore at 1.71 KMC, Figure A-5 above, can be made with the scattering at finite γ, Figures A-13, A-14.

10 log $\frac{H^2}{\pi a^2}$
+10
+5
0
$\frac{\psi_o}{\alpha}$
-1
0
1
$\theta_o = \frac{\pi}{2}$
$\theta_o = \frac{\pi}{4}$
$\theta_o = \frac{\pi}{2}$
10 log $\frac{\sigma}{\pi a^2}$ vs. $\frac{\psi_o}{\alpha}$
f = 1.71 KMC
γ = 1.7

Figure A-9

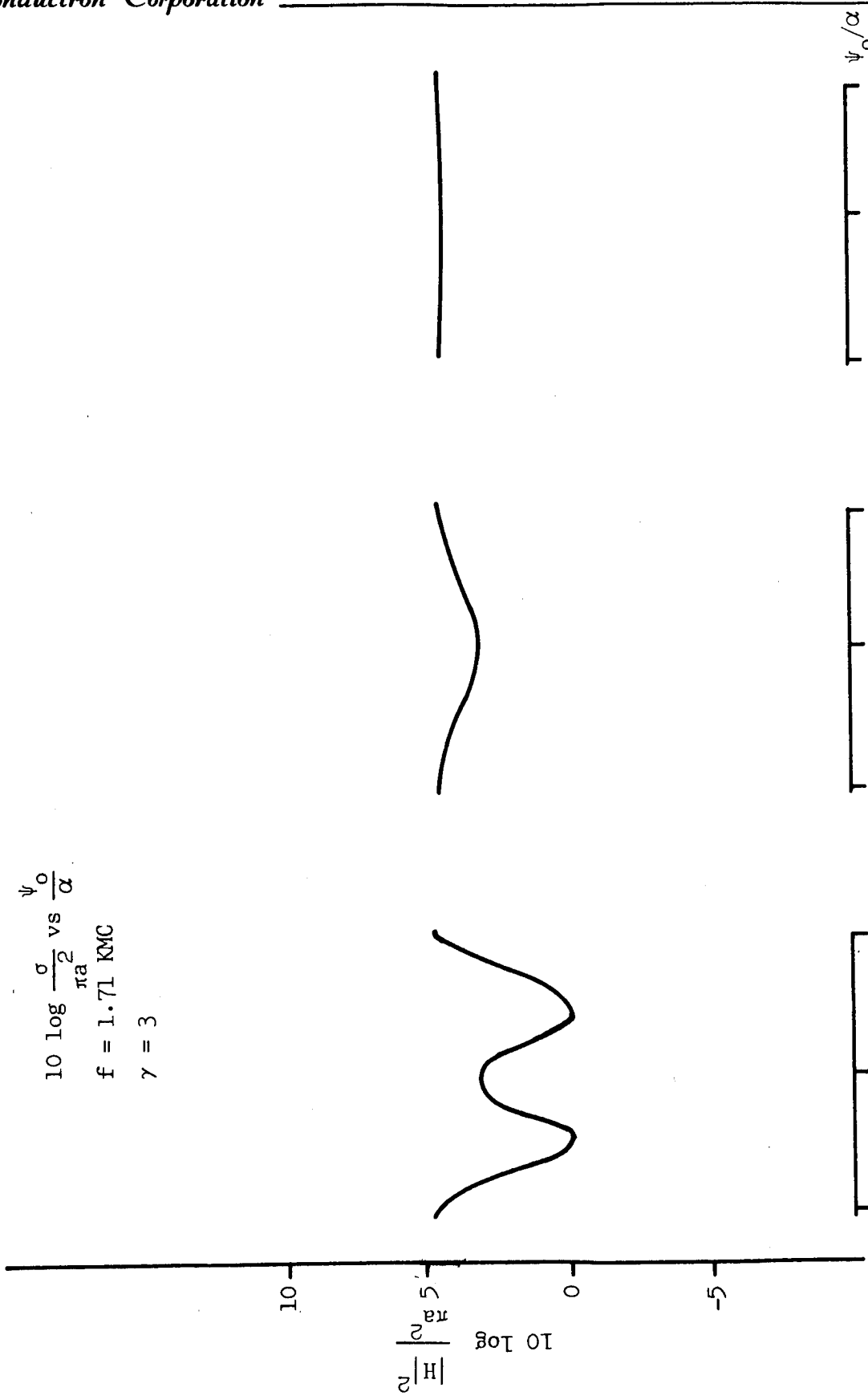
10 log $\frac{\sigma}{\pi a^2}$ vs $\frac{\psi_o}{\alpha}$
f = 1.71 KMC
γ = 3
10 log $\frac{|H|^2}{\frac{\sigma}{\pi a^2}}$
10
5
0
-5
$\theta_o = \frac{\pi}{2}$
$\theta_o = \frac{\pi}{4}$
$\theta_o = \frac{\pi}{6}$
-1
0
1
ψ_o/α

Figure A-10

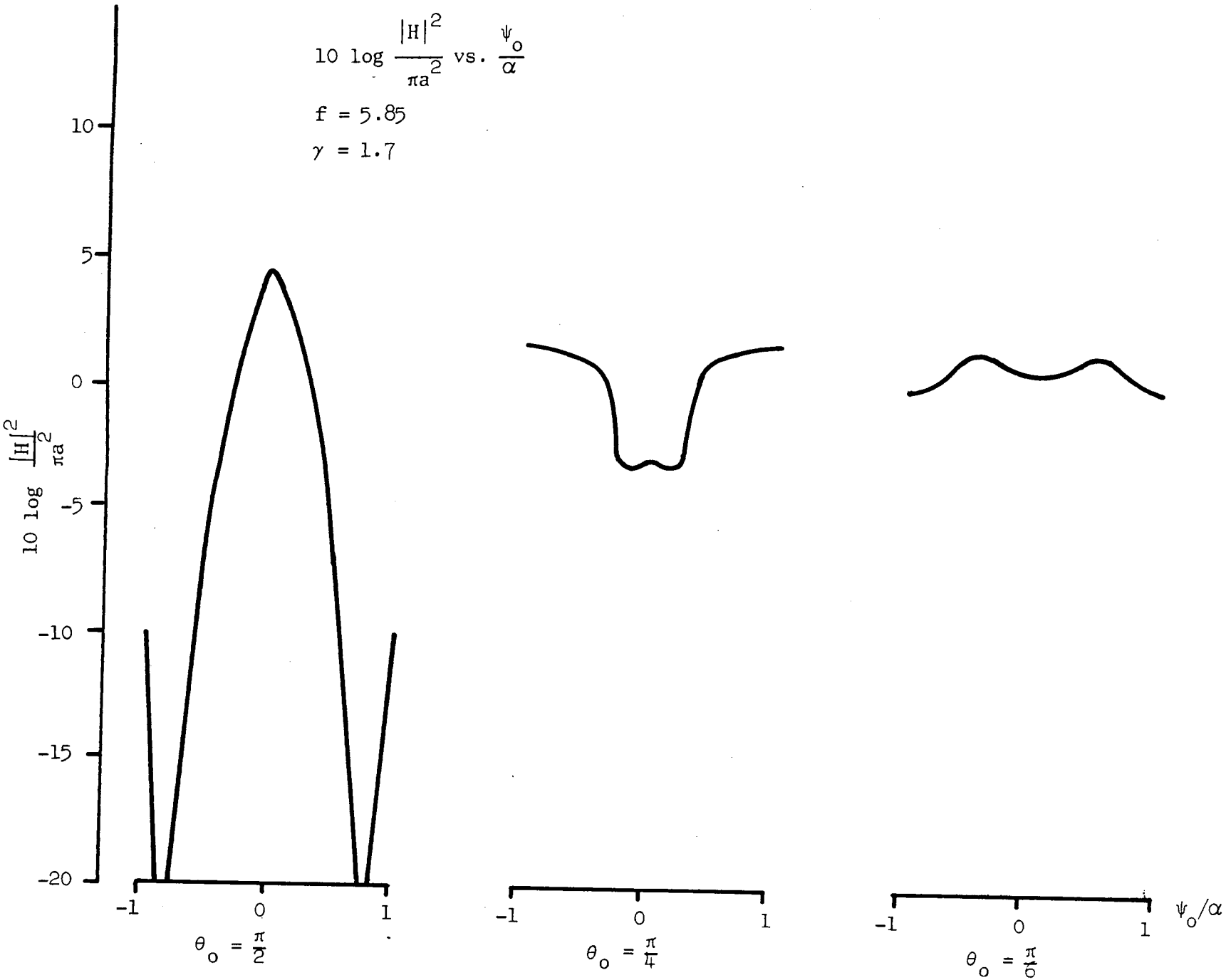
10 log |H|²/πa² vs. ψo/α
f = 5.85
γ = 1.7
10 log |H|²/πa²
10
5
0
-5
-10
-15
-20
-1
0
1
θo = π/2
θo = π/4
θo = π/6
ψo/α

Figure A-11

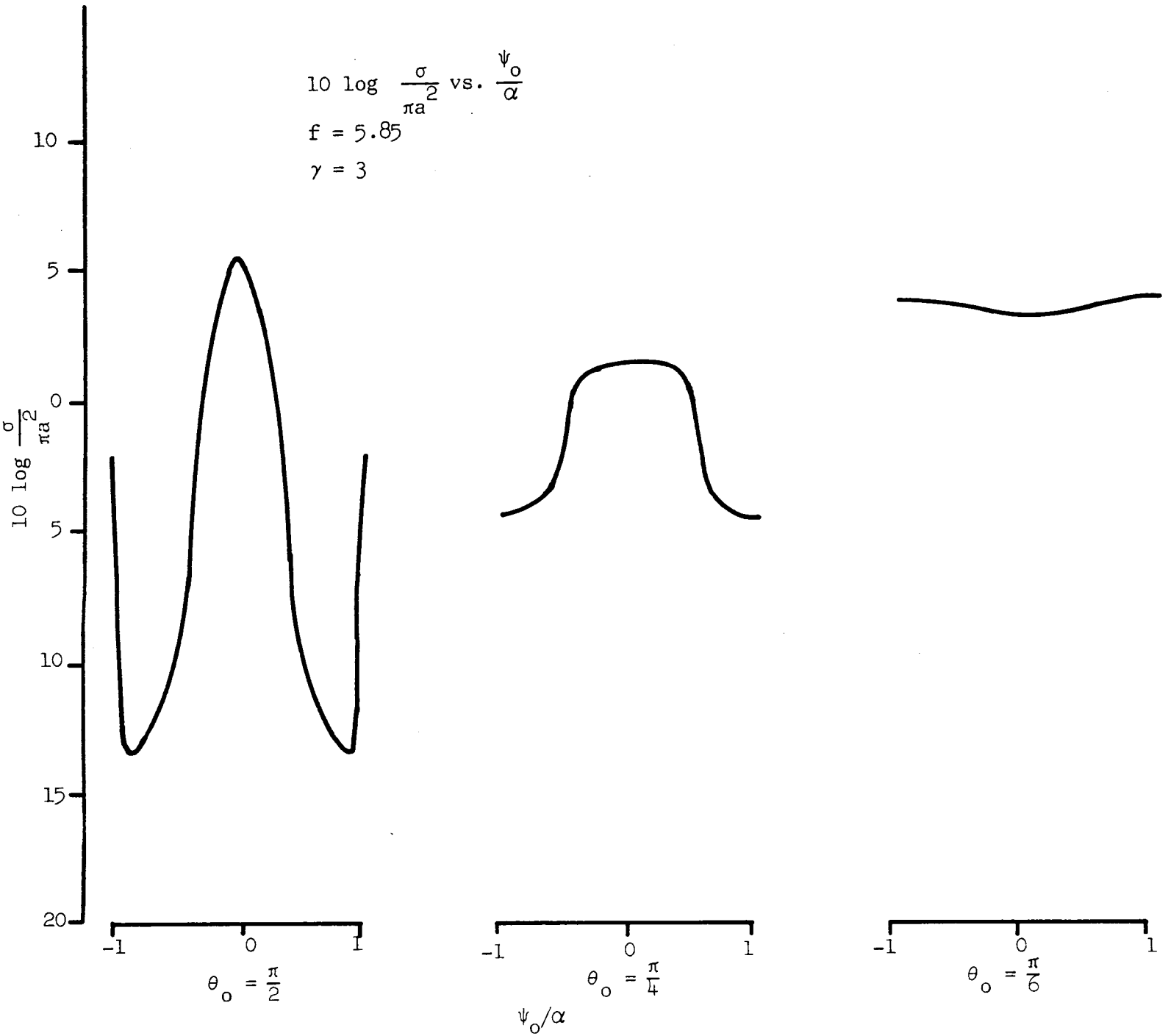
10 log $\frac{\sigma}{\pi a^2}$ vs. $\frac{\psi_o}{\alpha}$
f = 5.85
γ = 3
10 log $\frac{\sigma}{\pi a^2}$
10
5
0
5
10
15
20
-1
0
1
$\theta_o = \frac{\pi}{2}$
$\theta_o = \frac{\pi}{4}$
$\theta_o = \frac{\pi}{6}$
ψ_o/α

Figure A-12

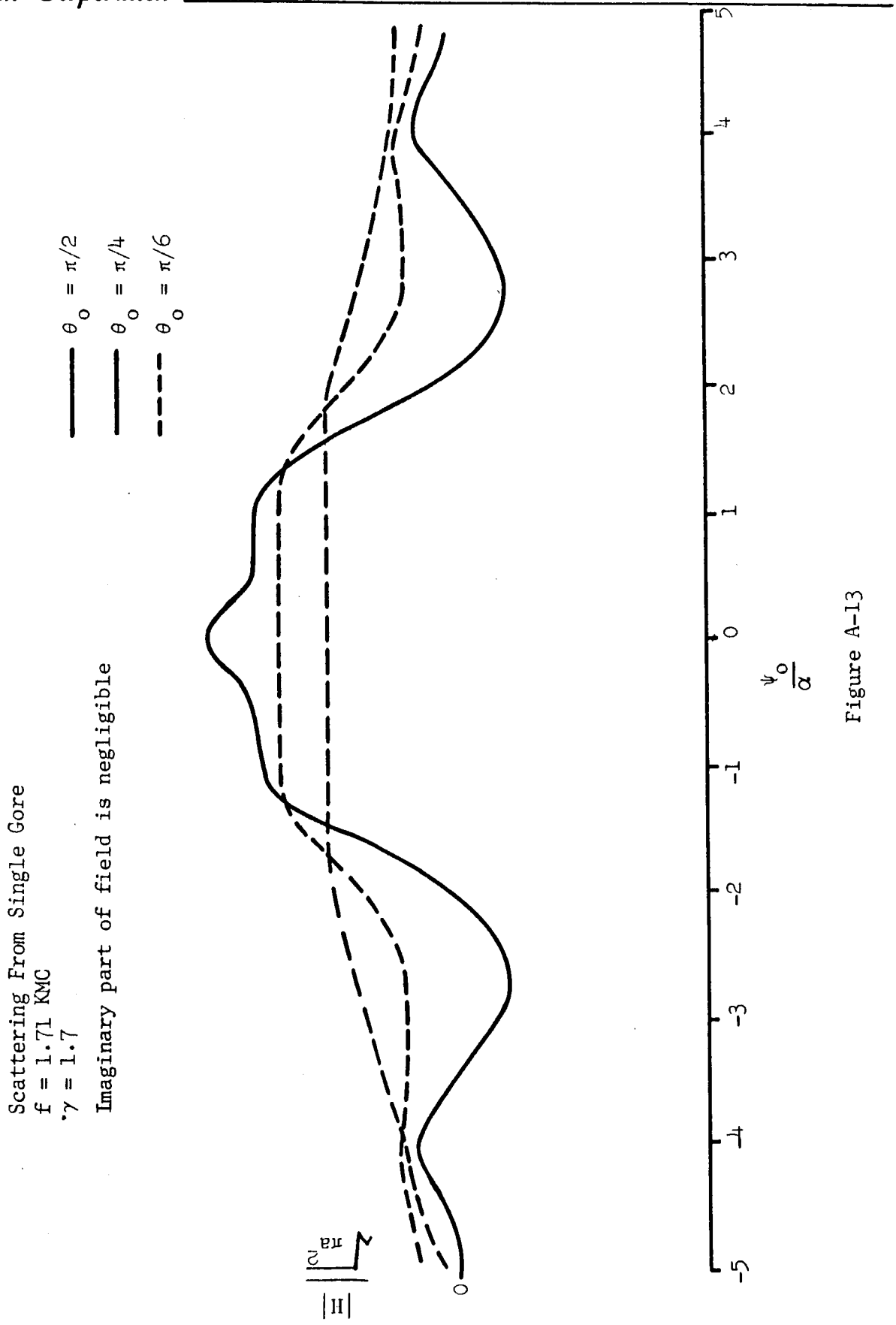
Scattering From Single Gore
f = 1.71 KMC
γ = 1.7
Imaginary part of field is negligible
θo = π/2
θo = π/4
θo = π/6
|H|
πa²
-5
-4
-3
-2
-1
0
1
2
3
4
5
ψo/α

Figure A-13

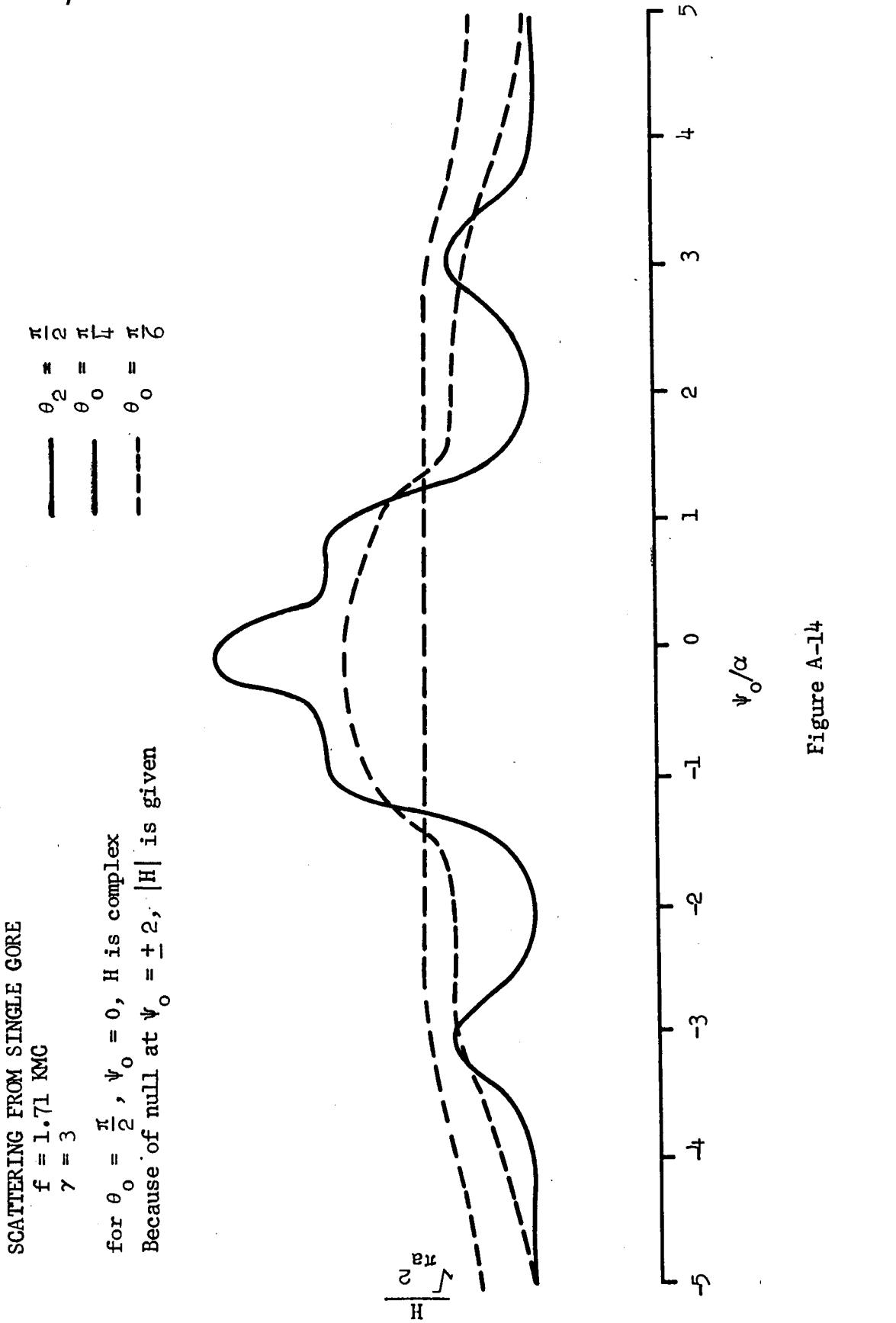
SCATTERING FROM SINGLE GORE
f = 1.71 KMC
γ = 3
for $\theta_o = \frac{\pi}{2}$, $\psi_o = 0$, H is complex
Because of null at $\psi_o = \pm 2$, |H| is given
$\theta_2 = \frac{\pi}{2}$
$\theta_o = \frac{\pi}{4}$
$\theta_o = \frac{\pi}{6}$
$\frac{H}{\sqrt{\pi a^2}}$
ψ_o/α
-5
-4
-3
-2
-1
0
1
2
3
4
5

Figure A-14

APPENDIX B

B.1 INFORMATION REGARDING MATERIAL BEHAVIOR

It is obviously necessary to gain a full understanding of the material behavior of the sandwich-type skin. Within the limited amount of the time available, it is felt that the Fairchild Stratos Corporation (FSC) has done an acceptable job. Nevertheless, the data which are presently available are not only not fully reliable, as pointed out by FSC itself, but they are also highly incomplete.

It appears that the balloon is to be inflated in such a way that plastic (i.e., permanent) deformations in the balloon take place. Consequently, as the pressure is being released, it is necessary to understand the mechanical behavior of the skin during the unloading process. Such test data are apparently not available at the present time, although it may be surmised that the material will unload elastically. Moreover, in view of the proposed penetration of the plastic domain, it is necessary to gain a better insight into the stress-strain law of the skin for different types of loading histories. Also, because some bending does take place, experimental information should be obtained regarding the response of the skin to bending moments. It is agreed, however, that shearing stresses are probably not an isssue.

The report of FSC assumes that, in view of the vastly larger magnitude of the modulus of elasticity of aluminum as compared with that of mylar, all the stresses are taken by the aluminum itself. This certainly requires experimental verification. Furthermore, it is necessary to gain information relative to the behavior of the skin after one or more of the aluminum facings have failed. None of the experimental data described above require a prohibitive apparatus; it should therefore be possible to conduct such a program locally without undue additional effort. Further experimental studies may become necessary as the need arises. For example, in order to minimize the irregularities at the seams, it may be desirable to reduce the bending stiffness of the splices (rather than to increase it as the present design seems to require). This could be achieved, for example, by omitting the inside aluminum facing and, in order to counteract this omission, by doubling the outside facing. Other methods are certainly feasible. In any event, the usefulness of such a step should be supported by experimental evidence.

In addition, because the inflating process introduces non-elastic strains and hence an unloading history different from the loading history, there may result not only residual strains, but also residual stresses. The average stress in the balloon, after the removal of the internal pressure, will obviously vanish. Nevertheless, local residual stresses may remain, especially near points of imperfection or discontinuities. It may therefore be necessary to test the material against the possibility

of stress relaxation--a phenomenon which, in time, may bring about a slight modification of the local irregularities, if not of the overall shape of the balloon.

B.2 ANALYSIS

No claim is made that a meaningful analysis is necessarily simple. Nevertheless, with realistic simplification, it appears likely that such an analysis can be undertaken within a reasonable effort. Basically, the balloon should be analyzed as a sequence of cylindrical shells (in the shape of the gores) spliced together at the seams. Such an analysis, in its pure form, is extremely complicated, especially if plastic deformations are to be included.

Fortunately, the thickness of the skin is so minimal that it is possible to ignore the bending stiffness of the shell. This leads to a "membrane" theory of substantially reduced complexity. The relevant equations of this theory are given in Equations B.1 to B.9 in Section B.3. It is noted that Equations B.7 to B.9 contain non-linear terms in the strain-displacement relations. Such terms are absolutely essential (and may in fact become dominant) if the radial displacement w is of the same order as, or larger than, the thickness t of the balloon. It is noted that these non-linear terms have not been included in the analysis prepared by FSC.

The boundary conditions governing a representative gore are given by Equations B.10 to B.14. Of these, Equations B.10 to B.12 represent symmetry conditions at the center of the gore. Equation B.13, at the edge, is also due to symmetry, and Equation B.14 represents the fact that the displacement of the seam must be radial. Since, on the other hand, the system of Equations B.1 to B.9 can be reduced to a sixth order system involving a stress function and the displacement w, it is necessary to establish three boundary conditions for each boundary. Equations B.13 and B.14 are therefore inadequate. An additional equation is obtained from the conditions of equilibrium; i.e., the resultant force in the radial direction must vanish in the seam. In the absence of any bending stiffness at all, this implies that the balloon must be smooth (see Equation B.22 for the simplified case).

This condition is apparently what the FSC report postulates. Actually while the thickness t of the skin, and hence the bending stiffness t^3, is exceedingly small, it does not vanish altogether. It may therefore be necessary, in the immediate vicinity of the splice, to take into consideration the full system of equations, including the effect of the bending stiffness. The order of the system of equations has now been raised to eight; the four boundary conditions then require that, in addition to Equations B.13 and B.14, the slope of the deflected surface vanish at the splice and that the splice be in equilibrium against radial motion. This condition, again for the simplified problem investigated in Section B.3, is given in the second and third of Equations B.26.

The effect of the finite bending stiffness is likely to be purely local. In other words, by employing standard boundary layer techniques, it is likely that a realistic solution to the problem can be given by a membrane analysis for the "interior" domain of the balloon and a boundary layer type analysis along the splices. None of these facts have been taken into consideration in the FSC report. Moreover, some of the averaging processes employed are not entirely clear. In fact, some of the connections between the final graphs and the intermediate equations apparently involve an amount of algebra which, at least at first glance is not altogether transparent. In any event, the analysis performed by FSC, while impressive in the light of the time restrictions, appears of limited relevance.

In Section B.3, a sample computation is attempted for a vastly simpler problem. In effect, the actual balloon has been replaced by a cylindrical shell of polygonal cross section similar to the actual cross section of the balloon at the equator. Such a computation can be carried out explicitly; the development of a boundary layer can also be shown in explicit form. It is not to be inferred that these results given have any quantative application to the problem of the almost spherical shell. However, it is felt that, as a demonstration of a simplified approach, some of the features of the expected computational method can be brought out in this manner.

B.3 The equations of equilibrium of a typical gore is given by the following equations:

$$N_{xx,x} + N_{xy,y} = 0 \qquad (B.1)$$

$$N_{xy,x} + N_{yy,y} = 0 \qquad (B.2)$$

$$N_{xx} w_{,xx} + 2 N_{xy} w_{,xy} + N_{yy} w_{,yy} - \frac{N_{yy}}{R} = -p \qquad (B.3)$$

In these equations, the first two constitute the condition of equilibrium in the tangent plane and the third the one perpendicular to it. The membrane forces are N_{ij}, and the deflection perpendicular to the tangent plane is w. A comma, followed by a letter, constitutes partial differentiation with respect to the corresponding coordinate. Equations B.1 and B.3 are taken relative to the final configuration, although certain standard approximations inherent in shell theory have been made.

The equations relating the membrane forces to the membrane strains e_{ij} are as follows:

$$N_{xx} = K'(\epsilon_{xx} + \nu \epsilon_{yy}) \tag{B.4}$$

$$N_{yy} = K'(\epsilon_{yy} + \nu \epsilon_{xx}) \quad \left(K' = \frac{Et}{1 - \nu^2}\right) \tag{B.5}$$

$$N_{xy} = K' (1 - \nu) \epsilon_{xy} \tag{B.6}$$

Finally, the strain-displacement relations are given by

$$\epsilon_{xx} = u_{,x} + \frac{1}{2} w^2_{,x} \tag{B.7}$$

$$\epsilon_{yy} = \nu_{,y} + v_{,x} + w_{,x} w_{,y}) \tag{B.8}$$

in which u and v are, respectively, the displacements in the x and y directions. It is noted, as already pointed out in the body of this report, that non-linear terms in the lateral deflection w are retained.

The system of Equations B.1 to B.9 involves nine unknown variables: The three independent membrane forces N_{ij}; the three displacement components u, v, and w; and the three independent membrane strain components ϵ_{ij}. Equations B.1 and B.2 imply the existence of a stress function. Equations B.7 to B.9 imply a compatibility relation among the strains after the elimination of u and v. When this is substituted in Equations B.3 to B.6, there result two equations in the stress function and the deflection w (associated with the name of Foeppl) which are of the sixth order.

The "boundary conditions" at the center of the gore are given by the symmetry conditions 10, 11, and 12 as follows:

$$N_{xy}(0,y) = 0 \tag{B.10}$$

$$w_{,x}(0,y) = 0 \tag{B.11}$$

$$u(0,y) = 0 \tag{B.12}$$

At the seam, the following two conditions

$$N_{xy}(\ell,y) = 0 \tag{B.13}$$

$$u(\ell,y) = w \tan \alpha \tag{B.14}$$

imply that, by symmetry, the shearing stress vanishes and the displacement is radial. A third condition can be obtained as is discussed in the body of the report; ℓ represents half the width of the gore.

In what follows the problem is investigated for the case in which ℓ is a constant (i.e., for a cylindrical vessel). In that case, all references to the y coordinate may be dropped. It follows, therefore, from Equation B.1 that

$$N = \text{constant} \tag{B.15}$$

in which N is employed for N_{xx}. In Equation B.3, simplification leads to

$$NW''' = -p \tag{B.16}$$

in which W is employed for the lateral deflection associated with the membrane theory and a prime represents differentiation with respect to the argument x. In view of Equation B.11 and B.15, Equation B.16 may be integrated to yield

$$W = A - \frac{p}{2N} x^2 \tag{B.17}$$

in which A is a constant of integration.

With the equivalent of Equations B.4 and B.7, the membrane force N is expressed in the form

$$N = Et\,(u' + \frac{1}{2} W'^2). \tag{B.18}$$

In view of the boundary condition 12 and Equations B.15 and B.17, the displacement u is obtained as follows:

$$u = \frac{Nx}{Et} - \frac{1}{6} \frac{p^2 x^3}{N^2} \tag{B.19}$$

It is noted that the second term on the right side of Equation B.19 is the result of the non-linear expression in Equation B.18. If it were omitted, the result would be in serious error, as can be seen below.

Because of the large number of gores, the width of the gore may be approximated by

$$\ell = R\alpha \tag{B.20}$$

where α represents half the central angle of the gore. When Equations B.17 and B.19 are substituted in the boundary condition B.14, this leads to the following relationship (with tan α replaced by α):

$$A = \frac{p}{2N} R^2\alpha^2 + \frac{NR}{Et} - \frac{1}{6} \frac{p^2 R^3 \alpha^3}{N^2} \tag{B.21}$$

Finally, to have equilibrium in the radial direction, it is necessary (within the confines of membrane theory) that the shell be smooth at the joints; this implies that

$$W'(\ell) = -\alpha \tag{B.22}$$

When this is substituted in Equation B.17, the expected result

$$N = pR \tag{B.23}$$

is obtained. All constants have now been determined as functions of the internal pressure p. In particular, the deflections at the center of the gore and at the seam are given, respectively, by

$$\begin{aligned} W(0) &= \frac{R\alpha^2}{3} + \frac{pR^2}{Et} \\ W(\ell) &= -\frac{R\alpha^2}{6} + \frac{pR^2}{Et} \end{aligned} \tag{B.24}$$

In these expressions, the first terms on the right side represent the "bulging" necessary to convert the polygon into a circle, and the second the expansion due to the internal pressure*.

The exact equations, which take account of the bending stiffness of the shell, should be

$$-\frac{Et^3}{12} w'''' + Nw'' = -p \tag{B.25}$$

instead of Equation B.16. The boundary conditions read as follows:

$$\begin{aligned} w''' (0) &= 0 \\ w' (\ell) &= 0 \\ N\alpha - \frac{Et^3}{12} w''' (\ell) &= 0 \end{aligned} \tag{B.26}$$

of which the first and third represent additional conditions and the second replaces Equation B.22. To solve this more accurate system, it is convenient to replace the independent variable x by z through

$$x = \ell - z. \tag{B.27}$$

In other words, z is measured from the edge into the interior. Also, let

$$w = W + v \tag{B.28}$$

* Equation B.24, could, of course, have been obtained by far more elementary procedures. The reason in carrying out the present process is to demonstrate the necessity of including the non-linear terms in the strain-displacement relations.

in which W is the result of the previous approximate computation. It follows then that v is governed by

$$\frac{Et^3}{12} v'''' - Nv'' = 0 \qquad (B.29)$$

in which the prime now represents a derivative with respect to z.

An approximate solution to Equation B.29, subject to the previously stated boundary conditions and the superposition 28, is given by,

$$v = \frac{\alpha}{\beta} e^{-\beta z} \qquad (B.30)$$

in which the parameter β is given by

$$\beta^2 = \frac{12N}{Et^3} \equiv \frac{12\epsilon}{t^2} \quad (\epsilon = \frac{t}{Et}) \qquad (B.31)$$

Equation B.30 is only approximate in the sense that it does not satisfy the conditions at the center of the gore exactly. However, the expression $R\alpha\beta$ passes all bounds for vanishing thickness t. In other words, Equation B.30 represents an asymptotic solution to the system considered here. It is seen that for increasing internal pressure the local irregularities decrease both in magnitude and extent. The analysis given above is based on elastic behavior. In the presence of plastic yielding it is expected that the surface becomes even smoother than indicated here.

The analysis given above demonstrates explicitly the development of a boundary layer. It is expected that similar behavior will prevail in the case of the actual shell. In effect, a singular perturbation has been performed on the simplified solution. This local behavior is entirely independent of the width of the gore as well as of the external boundaries (if any).

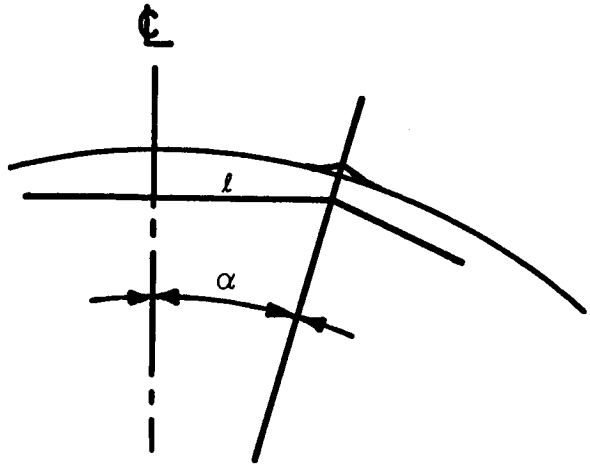

Figure B-1

APPENDIX C

C.1 INTRODUCTION

In the present investigation we are concerned with the reliability of the structural analysis of Echo II contained in a report by the ASTRO Research Corporation (ARC). This report deals with the deviation from perfect spherical shape of an Echo II balloon which is constructed by means of a large number of gores made out of a sandwich-type material (X15). The ARC report is entirely predictive, and it is the purpose of the present study to arrive at an evaluation of these predictions.

The ARC report may reasonably be divided into three sections:

1. the predicted shape of the balloon under internal pressure and under the assumption of perfectly elastic behavior;

2. the effect of the pressure relaxation, especially in view of the assumed irreversible material behavior; and

3. an experimental study to establish the material constants used in the first two sections of the report.

In the second section referred to above, the material is assumed to unload elastically. Since, according to the ARC report, the unloading characteristic of the balloon is primarily based on the results of the first section, it becomes clear that the reliability of the first section is essential for all subsequent analyses. It is for this reason that the present study concerns itself primarily with the first section.

C.2 ANALYSIS OF INFLATED SHAPE

The authors of the ARC report have recognized the fact that the problem of computing the predicted inflated shape is essentially a non-linear one. In its original (that is, uninflated) state, the balloon is composed of a large number of gores, which are cut in such a manner as to form portions of circular cylinders after assembly. In other words, a parallel of latitude appears as a polygon rather than as a circular, while the center lines of the gores appear as circles of radius r_o.

In its inflated state the balloon should be spherical, or nearly so. The authors of the ARC report have attempted to predict the exact shape by first assuming it to be a perfect sphere and by then applying corrective terms to this sphere on the basis of the violation of one of the equations of equilibrium. Apparently assuming this correction to be comparatively small they have linearized this process; if carried out properly, this appears to be a legitimate procedure. However, we will show that, in our opinion, the results of the ARC report are of questionable validity.

The ARC report is rather concise, making it necessary at times to guess as to what the authors had in mind. We have attempted to reconstruct their apparent thinking and computations. In particular, if we assume that the balloon is inflated into a perfect sphere of radius r, then the strains in the meridional and azimuthal directions are given in Eqs. (1) and (2) of the report. We have confirmed Eq. (1) but have been unable to confirm Eq. (2). Instead, according to our calculations, the latter should read

$$\epsilon_\varphi = \frac{r}{r_o} \left(1 - \varphi^2 \cos^2 \theta\right) - 1 \qquad (2')$$

if only terms up to the second power in φ are included. The discrepancy does not appear serious, however, since the authors' Eq. (2) represents the average of our Eq. (2') over the width of one gore. It is conceivable (although the report makes no mention of it) that this was done by the authors to satisfy one of the equations of equilibrium in the plane tangent of the sphere. The authors' as well as our own computations are based on the assumption that each point on the balloon moves radially outward.

This assumption, of course, is artificial and can only be maintained if it leads to a system of stresses which are in equilibrium. The authors note that this is, in fact, not true and that there exists an imbalance between the uniform outward pressure and the resisting radial resultant pressure associated with the meridional and azimuthal membrane forces. They also note a further imbalance associated with the presumed reinforcement at the seams; however, we will not pursue this in detail in the present study since it is our belief that even if the balloon were truly homogeneous the authors' conclusions would be open to doubt.

If the membrane forces N_θ and N_φ are computed on the basis of Eq. (1) and (2), and if the shearing strains and hence shearing stresses are correctly assumed to vanish, then the equations of equilibrium are violated both in the radial and in the meridional direction. The authors attempt to make allowance for the former but not for the latter. It is for this reason that the basic assumption of the authors (namely purely radial movement) is actually untenable. In Section C.5 it is shown that meridional as well as azimuthal movement takes place and that the final shape of the inflated balloon is not spherical, but slightly spheroidal. The authors' analysis, in the absence of the effect of inhomogeneity at the seams, does not account for this.

So far as the radial imbalance is concerned, the authors assume that this can be handled by additional radial displacements which are governed by Eqs. (3) and (4), of which the former is neglected. When this additional radial movement is expanded in a Fourier series along a parallel of latitude, and when the load imbalance is similarly expanded, then, by equating the first terms in the expansions, the authors arrive at Eq. (5). We have been able to confirm Eq. (5) only on the assumption that the second term on the right side of Eq. (4) is neglected. This appears to be a reasonable assumption. Moreover, the authors' conclusion that the deviation from sphericity does not contain a term which is quadratic in the width of the gore is confirmed in our own analysis as shown in the Appendix.

However, Eq. (5) must be questioned in that it contains the term ϵ_o in the denominator. Also, when the second term on the right side of Eq.(4) is neglected, the use of a Fourier expansion appears unnecessary since the additional displacement can then be obtained through direct integration. This also leads to the predicted "kink" in the final shape as a result of the seam reinforcement. Finally we are tempted to question the actual quantitative results which, according to the authors, vary with the fourth power of the width of the gore. Since the original development of Eqs. (1) and (2) was correct up to only the second power, the conclusions are believed to be unreliable.

The strains obtained in Eqs. (1) and (2) are somewhat at variance with the ones derived in Section C.5. If, in conformity with the discussion in Section C.5, the strain ϵ_o is assumed to be of the same order of magnitude as $(\pi/n)^2$, that is, if

$$2\,\epsilon_o = \lambda\,(\pi/n)^2,$$

then Eq. (2) takes the form

$$\epsilon_\varphi = \left(\frac{\pi}{n}\right)^2 \left(\frac{\lambda}{2} - \frac{1}{3}\cos^2\theta\right) \pm \ldots$$

if again only terms up the second power in π/n are included. In contrast, it is shown in Section C.5 that ϵ_φ is independent of θ so far as the term involving $(\pi/n)^2$ is concerned. Since it is this variation which forms the basis for the correction during the unloading process, it appears that the authors' subsequent developments are without proper foundation.

However, assuming Eq. (6) to hold during unloading, the authors develop Eqs. (7) and (9) on the basis of Eqs. (1) and (2). We have been unable to follow the rationale behind this procedure. Eqs. (1) and (2) give strains which are inadmissible, according to the authors, and which give rise to additional radial displacements as indicated in Eq. (5). It is not clear why these corrective displacements have not been incorporated in the strain expressions before proceeding to the determination of the unloading process. In any event, in view of the uncertain validity of the assumptions underlying all these equations as well as of the preliminary computations carried out in Section C.5 we are not tempted to place too much credence in the quantitative results obtained in the ARC report.

C.3 EXPERIMENTAL PROCEDURE

In contrast to the foregoing discussion, the test procedure as outlined in the ARC report appears to be sound and well conceived. The program is fairly straightforward, and the results should be reasonably reliable, given a fair degree of care during the experiments.

We find the substantially lower value of the stiffness K_o, as compared with the predicted value, as puzzling as do the authors. However, the authors' explanation in terms of a miss-match of the cylinder with the splicing material is somewhat bewildering. In particular, we have been unable to find a rational

derivation for the equations on Page 23. Perhaps this is due to a laxity in the definition of the terms. As the equations are written, it would follow that the specimen is subjected to an axial force and a bending moment for vanishing values of ϵ. Rather we expect that the apparent "softness" of the specimen is due to the substantial unevenness and wrinkles which produce extensions under forces which are substantially smaller than they would be in the absence of such wrinkles.

C.4 PRINCIPAL DISAGREEMENT

We believe that the structural analysis contained in the ARC report does not represent a safe prediction of the final shape of the Echo II balloon. All deviations from true sphericity during unloading are computed on the basis of the assumption that the balloon, during the inflation process, becomes a perfect sphere through radial motion. This assumption is unconfirmed, untenable, and contradicted in our own preliminary study.

C.5 AN INDEPENDENT ANALYSIS

In what follows we develop the basic equations governing the idealized case of an elastic balloon of homogeneous properties and composed of a large number of gores. For simplicity we assume Poisson's ratio μ to vanish; this introduces no significant deviation from generality. We assume a circular cylindrical coordinate system in which the z axis represents the axis of rotation of a representative cylindrical gore segment and in which the x and y axis form the plane containing the center line of that gore. The y axis points toward the pole and the x axis lies in the equatorial plane. We denote unit vectors in the coordinate directions by $\bar{e}_x$, $\bar{e}_y$, $\bar{e}_z$ respectively.

If r (corresponding to r_0 in the ARC report) denotes the radius of the gore cylinder and θ the latitude of a generic point, then the position vector in the original configuration can be written as

$$\bar{r} = r \cos\theta\, \bar{e}_x + r \sin\theta\, \bar{e}_y + z\, \bar{e}_z \qquad (C.1)$$

In the deformed state the position vector is

$$\bar{R} = \bar{r} + (w \cos\theta - v \sin\theta)\, \bar{e}_x + (w \sin\theta + v \cos\theta)\, \bar{e}_y + u\, \bar{e}_z \qquad (C.2)$$

in which u, v, w represent the displacement components in the axial (z), circumferential (θ), and radial direction, respectively, and are each to be treated as functions of the variables θ and z. The boundary of the gore is given (originally) by $z = \alpha r \cos\theta$, in which α represents the very small half central angle at the equator and corresponds to the ARC term π/n. Henceforth, for the sake of simplicity, this boundary will be referred to as B.

It follows from the symmetry of the problem that all points on B move in the plane containing B and the center of the balloon. This can be expressed in the form

$$\bar{R} \cdot \bar{e}_z = \alpha\, \bar{R} \cdot \bar{e}_x \text{ on B}$$

which, after substitution of Eqs. (1) and (2), leads to

$$u = \alpha\ (w \cos\theta - v \sin\theta) \text{ on B} \qquad (C.3)$$

Note that Eq. (C.3) as well as the boundary conditions developed later on must be satisfied for all values of θ.

A further result of the symmetry of the deformation is obtained by setting the shearing membrane force equal to zero on B, that is

$$S = 0 \quad \text{on B} \qquad (C.4)$$

This shearing force S is expressed in terms of the displacements later on.

A final boundary condition is obtained from the assumption that the shell has vanishing bending stiffness. In the "membrane" so obtained, equilibrium requires the absence of discontinuities in the surface slopes (unless there exist concentrated forces). In the present case this implies that the balloon must be "smooth" at the seams;[1] in view of the symmetry of the deformation described previously, this in turn means that the vector normal to the balloon surface must also lie in the plane of B, that is,

$$\bar{R}_{,\theta} \times \bar{R}_{,z} \cdot \bar{e}_z = \alpha\ \bar{R}_{,\theta} \times \bar{R}_{,z} \cdot \bar{e}_x \text{ on B},$$

in which a comma followed by a subscript represents the partial derivative with respect to the associated variable.

When Eqs. (C.1) and (C.2) are substituted in this equation, and after linearization with respect to the displacement components, we obtain

$$w_{,z} = -\alpha \cos\theta\ (1 + u_{,z}) - \frac{\alpha}{r}\ [(w_{,\theta} - v) \sin\theta + (w + v_{,\theta}) \cos\theta] \text{ on B} \qquad (C.5)$$

In line with the assumption of the vanishing of Poisson's ratio, the membrane forces are expressed in terms of the displacements as follows:

$$N_z = K\left(u_{,z} + \frac{1}{2}\ w^2{}_{,z}\right)$$

$$N_\theta = \frac{K}{r}\ (v_{,\theta} + w) \qquad (K = E\ t) \qquad (C.6)$$

$$2S = K\left(\frac{u_{,\theta}}{r} + v_{,z}\right)$$

In Eq. (C.6) we have retained some non-linear terms and have discarded others; this is consistent with the assumption of "shallow shell" theory.

We now expand the displacement components in a power series near the central line $z = 0$ as follows:

---

[1] A more realistic analysis involves the development or retention of slight kinks as boundary layers. This has been discussed in Appendix B.

$$\frac{w}{r} = a + b\,\frac{z^2}{r^2} \pm \ldots$$

$$\frac{u}{r} = c\,\frac{z}{r} + d\,\frac{z^3}{r^3} \pm \ldots \qquad \text{(C.7)}$$

$$\frac{v}{r} = f + g\,\frac{z^2}{r^2} \pm \ldots$$

in which the terms a, b, etc., are functions of θ. A so, Eq. (C.7) already take account of obvious symmetry conditions with respect to the central line.

If Eq. (C.7) is substituted in Eq. (C.6), then the membrane forces are also expressed in terms of power series in z. These membrane forces are subject to the three equations of equilibrium

$$N_{z,z} + \frac{S,_\theta}{r} = 0$$

$$S,_z + \frac{N_{\theta,\theta}}{r} = 0 \qquad \text{(C.8)}^2$$

$$\frac{N_\theta}{r} - N_z\, w,_{zz} = p$$

in which the last equation represents again an approximation consistent with shallow shell theory, and p designates the internal pressure. Substitution of Eqs. (C.7) and (C.6) in Eq. (C.8) results in a system of equations, which, for z = 0, assumes the form

$$6\,d + 4\,b^2 + \frac{1}{2}\,c'' + g' = 0 \qquad \text{(a)}$$

$$\frac{1}{2}\,c' + g + f'' + a' = 0 \qquad \text{(b)} \qquad \text{(C.9)}$$

$$f' + a - 2\,b\,c = \frac{pr}{K} \qquad \text{(c)}$$

Similarly, Eqs. (C.4), (C.3), and (C.5) lead to

$$c' + 2\,g = -\,d'\,\alpha^2 \cos^2\theta \pm \ldots \qquad \text{(d)}$$

$$c - a + f\tan\theta = -\,(d - b + g\tan\theta)\,\alpha^2 \cos^2\theta \pm \ldots \qquad \text{(e)} \qquad \text{(C.9)}^3$$

$$2\,b + c + a'\tan\theta + a + f' - f\tan\theta =$$

$$= -\,1 - (3\,d + b'\tan\theta + b + g' - k\tan\theta)\,\alpha^2 \cos^2\theta \qquad \text{(f)}$$

---

2 The exact equations of equilibrium relative to the deformed configuration contain further terms, which can be ignored in the present case.

3 The terms omitted contain powers of α higher than the second.

in which a prime represents the derivative with respect to θ.

Eqs. (C.9) constitute a system of six non-linear differential equations in the six unknown functions a, b, c, d, f, and g. The general solution of this system is, of course, involved and is therefore not attempted here. However, if it is assumed that all functions are regular in α near $\alpha = 0$ and can therefore be expanded in a power series near $\alpha = 0$ (that is, $a = a_o + \alpha^2 a_1 \pm \ldots$ etc), then it is possible to find the solution by means of the usual perturbation technique by equating individual powers of α to zero. Also, it will be assumed that the right side of Eq. (C.9c) can be expressed in the form $\lambda \alpha^2$ in which λ is a term comparable in magnitude to unity.[4]

In the perturbation expansion described above, the system of equations involving the terms independent of α leads to

$$b_o = -\frac{1}{2} \; ; \; d_o = -\frac{1}{6} \; ; \; a_o = \ldots = g_o = 0 \qquad \text{(C.10)}$$

It is noted that Eqs. (C.10) do not represent the only possible solution; however, the other solutions are physically unrealistic and lead to difficulties in the higher order expansions.

For the terms quadratic in α we arrive at the following system of equations:

$$6 d_1 - 4 b_1 + \frac{1}{2} c_1'' + g_1'' = 0 \qquad \text{(a)}$$

$$\frac{1}{2} c_1' + g_1 + f_1'' + a_1' = 0 \qquad \text{(b)}$$

$$f_1' + a_1 + c_1 = \lambda \qquad \text{(c)}$$

$$c_1' + 2 g_1 = 0 \qquad \text{(d)}$$

$$c_1 - a_1 + f_1 \tan\theta = -\frac{1}{3} \cos\theta \qquad \text{(e)}$$

$$2b_1 + c_1 + a_1' \tan\theta + a_1 + f_1' - f_1 \tan\theta = \cos^2\theta \qquad \text{(f)}$$

(C.11)

By combining Eqs. (b), (c), (d), and (e) we are led to the following equations:

$$a_1 + f_1' = C_1 \qquad \text{(a)}$$

$$f_1' + f_1 \tan\theta = 2 C_1 - \lambda - \frac{1}{3} \cos\theta \qquad \text{(b)}$$

(C.12)

in which C_1 is a constant integration. The general solution of Eq. (C.12b) is

---

[4] See Section C.5.

$$f_1 = \left[C_2 + (2 C_1 - \lambda) \ln \tan \left(\frac{\theta}{2} + \frac{\pi}{4} \right) - \frac{\theta}{3} \right] \cos \theta, \qquad (C.13)$$

in which C_2 is another constant of integration. Since, at the equator, v vanishes, and because of the regularity requirements at the poles, it follows that $C_2 = 0$ and $C_1 = \frac{\lambda}{2}$, that is,

$$f_1 = - \frac{\theta}{3} \cos \theta \qquad (C.14)$$

and, in view of Eq. (C.12a),

$$a_1 = \frac{1}{3} \cos \theta - \frac{\theta}{3} \sin \theta + \frac{\lambda}{2} \; . \qquad (C.15)$$

Substitution in the other equations leads to

$$c_1 = \frac{\lambda}{2} \; ; \; g_1 = 0, \qquad (C.16)$$

and finally, in view of Eqs. (C.11a) and (C.11f),

$$b_1 = \frac{1}{2} (\cos^2 \theta - \lambda) + \frac{1}{3} \sin \theta \tan \theta \qquad (C.17)$$

$$d_1 = \frac{1}{3} (\cos^2 \theta - \lambda) + \frac{2}{9} \sin \theta \tan \theta$$

The process could now be continued for the determination of the higher order terms; however, this is not attempted here since the main purpose of this investigation is to present a comparison of our solution with that presented in the ARC report. It is felt that the results obtained here and evaluated further below afford such a comparison.

With all the functions so obtained we determine the displacements, after letting $z \equiv \alpha \, r \, \zeta$,

$$\frac{w}{r} = \alpha^2 \left(\frac{\lambda}{2} + \frac{1}{3} \cos \theta - \frac{\theta}{3} \sin \theta - \frac{1}{2} \zeta^2 \right) \pm \ldots$$

$$\frac{u}{r} = \alpha^3 \left(\frac{\lambda}{2} \zeta - \frac{1}{6} \zeta^3 \right) \pm \ldots \qquad (C.18)$$

$$\frac{v}{r} = - \frac{\alpha^2}{3} \theta \cos \theta \pm \ldots$$

It is noted that Eqs. (C.18) and especially the presence of a circumferential displacement v, are incompatible with the authors' assumed radial movement. Similarly, the membrane forces are given as

$$N_z = K \lambda \frac{\alpha^2}{2} \pm \ldots$$

$$N_\theta = K \lambda \frac{\alpha^2}{2} \pm \ldots \qquad (C.19)$$

$$S = 0 \pm \ldots$$

We note that, so far as the terms involving the second power of α are concerned, the membrane forces are constants; this is in contradiction with the ARC report, as already discussed in the main body of this study.

Finally, with the displacements given in Eqs. (C.18), we determine the position vector in the deformed state by substitution in Eqs. (C.1) and (C.2). If we call R the final distance of a generic point from the center of the balloon, we obtain, for $z = 0$,

$$\frac{R}{r} = 1 + \alpha^2 \left(\frac{\lambda}{2} + \frac{1}{3} \cos\theta - \frac{1}{3}\theta \sin\theta \right) \pm \ldots \qquad (C.20)$$

The same expression is obtained for any other value of z. In other words, within the approximation implicit in terminating the series with the second power of α, the parallels of latitude are perfect circles. To the extent that the deviation from true circularity does not appear for terms of power less than the fourth, the present study is in agreement with the ARC report; however, no agreement as to the magnitude of the fourth order term is implied. Moreover, Eq. (C.20) shows that the meridians are not true circles and that, within the limits of the expansion employed here, there occurs a flattening of the sphere which is given by

$$\frac{R}{r}(\theta = 0) - \frac{R}{r}\left(\theta = \frac{\pi}{2}\right) = \frac{\alpha^2}{6}(2 + \pi) \pm \ldots \qquad (C.21)$$

This flattening effect is missing in the ARC report; this is not surprising inasmuch as the ARC report is based on the fundamental assumption of radial motion into circular shape.

APPENDIX D

This report is concerned with the Radar Reflectivity Measurements performed by Conductron for NASA as part of the Static Inflation Tests, Lakehurst, NAS, June - July 1963.

D.1 DESCRIPTION OF MEASUREMENT PROCEDURE

A scaffold, 48 feet high, was erected in the Lakehurst NAS main dirigible hangar. Upon this scaffold was constructed a wooden track, 86 feet in length. The track formed a circular arc; 100 feet from the surface of the balloon, which when inflated, had a radius of 67.5 feet. The angle subtended by the arc was 30°. Figure D-1 illustrates the relative position of the inflated balloon, the scaffolding, and the hangar interior. Figure D-2 illustrates the plan view of the relative positions of the balloon and the scaffolding. At either end of the track was located two standard gain horn antennas, one L-Band and one C-Band. They were mounted back to back so that by a rotation, either one could be made to point at the balloon, aligned along the balloon radius. These horns were the transmitting antennas, being connected, respectively, to a 1.71 KMC and a C-Band CW source. The sources were located on a platform mounted just beneath the track. A small wooden cart was constructed to move along the track. On the cart, similarly to the transmitting horns, were mounted a third pair of horns. These served as receiving antennas, and were connected to a Scientific Atlanta receiver, located on the deck of the hangar. The coordinates of the recorder chart were db vs. angle. The cart was motor driven, and its position on the track was synchronized to the motion of the recorder chart, so that the angular position of the cart could be made to coincide with the recorded position on the chart. The cable from the receiving antenna to the receiver was slung so that constant cable length could be maintained, independently of cart position. Figure D-3 is a sketch of the physical arrangements.

Switching was provided so that all changes of electrical connections and positioning of the receiver cart could be controlled from a console which was constructed and located adjacent to the receiver. Rotation of the horns was performed by technicians who were located at either end of the track. Tuning and monitoring of the RF sources was performed by a technician located on the source platform. The mounting of the horns was constructed so that axial rotation could be performed, permitting change of polarization.

One hundred feet from the scaffold and on the opposite side from the balloon, a tower was erected, atop of which was placed a flat calibration plate whose position could be remotely controlled and synchronized. During calibration runs the horns were aligned in the direction of the flat plate. Calibrations were performed at 5.85 and at 1.71 KMC. Prior to a test sequence, the C-Band horns were aligned in the direction of the flat plate, with the receiver cart adjacent to the left transmitter horn. All horns were at vertical polarization. The 5.85 source was connected to the left transmitting horn, the flat plate rotated, and a flat plate pattern run off on the recording paper. The

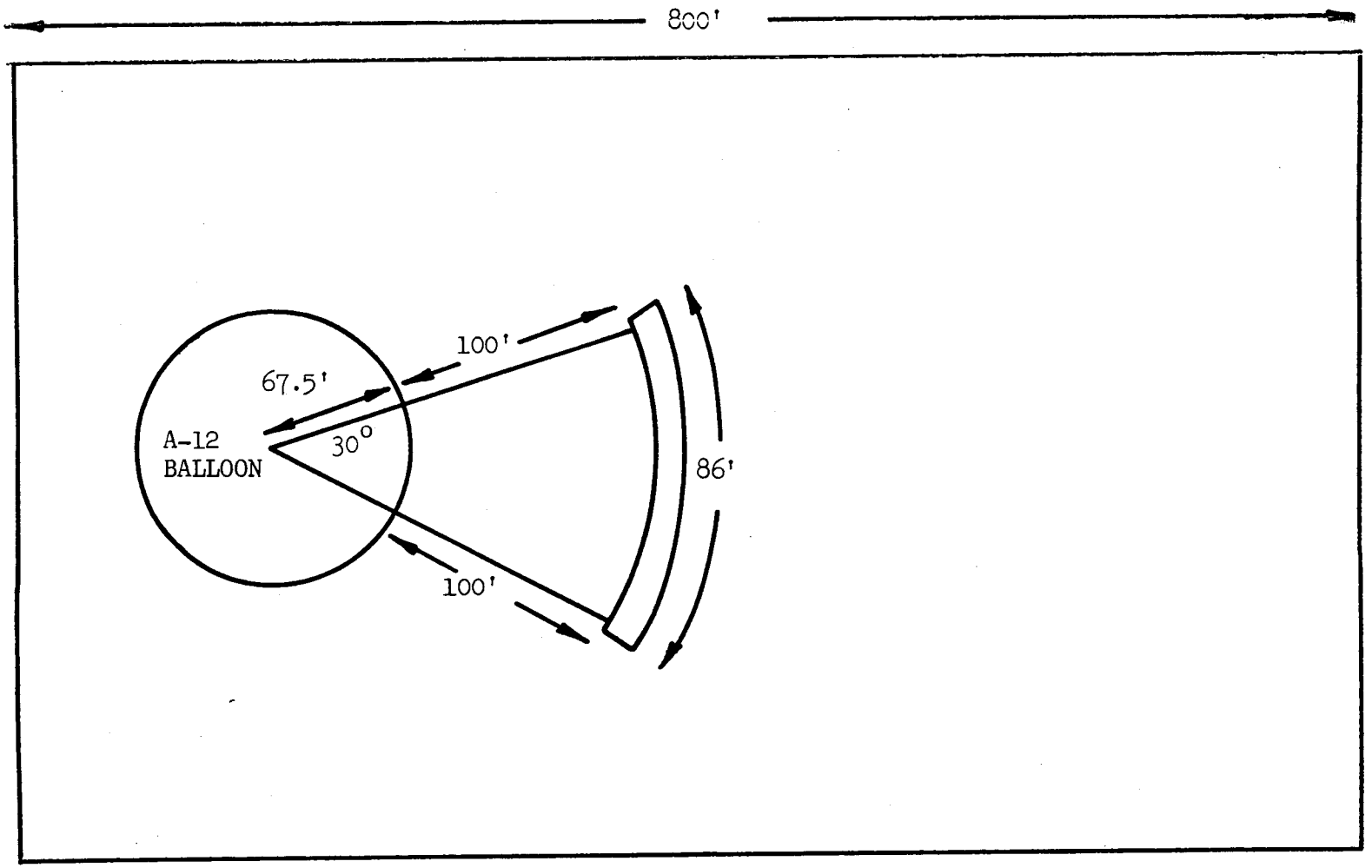

Figure D-1 Schematic (Not Scale) Representation of RF Equipment Mounting Relative to the Balloon.

An 86 foot track was constructed on top of a 50 foot scaffold. Transmitting antennas were located at either end of the track and a moveable cart containing receiving antennas had its position synchronized to the receiver console. Receiver was located on the ground. RF sources were mounted on a platform suspended from and directly below the track (see Figure D-3).

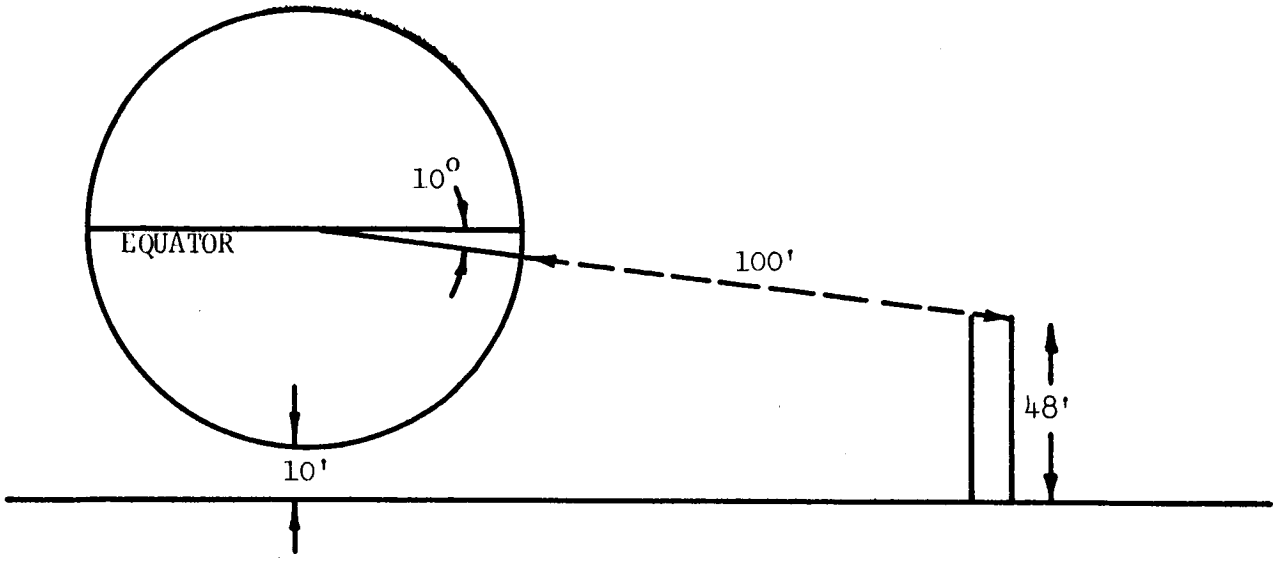

Figure D-2 (Not Scale) Plane View of Scaffold-Balloon Configuration. Viewing Aspect for 10° South of Equator

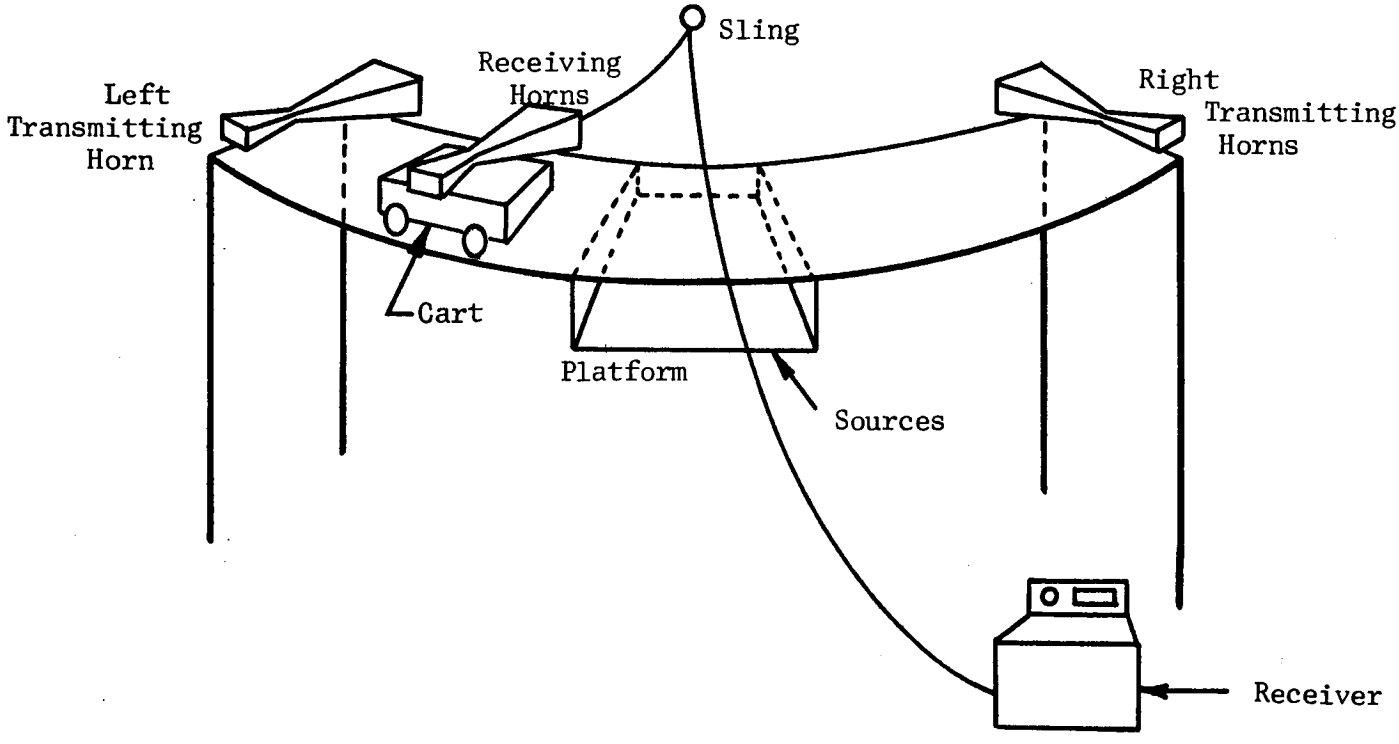

Figure D-3 Sketch (Not Scale) of Scaffold Antennas and Receiver Arrangement

voltage source was then connected to the receiver through an attenuator and adjusted so that the receiver pen coincided with the flat plate maximum. A straight line pattern, using this attenuator setting was run. The right transmitter was then connected, a new flat plate pattern recorded, and its maximum compared to the straight line pattern. The attenuator setting was then readjusted so as to lie midway between the two flat plate maximum. This adjustment was maintained throughout the test sequence, and used as the calibration level for measurements at 5.85 and 5.65 KMC. Its nominal value at 5.65 was obtained by computation. The L-Band system was similarly calibrated. At the conclusion of a test sequence, the stability of the source was tested against a flat plate run. For no test sequence was there observed a change in the calibration level.

A test sequence was performed in the following steps:

1. Upon being notified by the test director that the balloon had been inflated to a given pressure level, which was to be maintained throughout the test sequence, the L-Band system was connected and the horns, all polarized vertically, were aligned on the balloon, the receiver cart adjacent to the right transmitter.

2. The right transmitter was connected, and the cart moved to the left, the signal level being recorded.

3. When the receiving horn reached the left most position, the left transmitter was connected, and the receiving horn run to the right. Simultaneously the right transmitter was rotated to horizontal polarization.

4. Upon reaching the right most position, the right transmitter was connected, the receiver run to the left, and the left transmitter rotated to horizontal.

5. Upon reaching the left most position, the left transmitter was connected and the cart run to the right.

6. Upon reaching the right most position, the receiving horn was rotated to horizontal, the right transmitter connected, and the cart run to the left.

7. Upon reaching the left most position, the left transmitter was connected, and the cart run to the right.

8. The recording paper was then calibrated with the secondary standard.

These steps were then repeated for 5.65 and 5.85 KMC. In this fashion, at each frequency, patterns were obtained, which for simplicity, were successively labeled in the following manner:

TRANSMIT RIGHT	VV
TRANSMIT LEFT	VV
TRANSMIT RIGHT	HV
TRANSMIT LEFT	HV
TRANSMIT RIGHT	HH
TRANSMIT LEFT	HH

For any transmit position, the bistatic angle increased from 0^{o} to 30^{o}. The "specular" angle, defined as the bisector of the bistatic angle, increased from 0^{o} to 15^{o}. If the specular angle were redefined to be the angular position on the balloon corresponding to the specular ray, letting, for convenience, the right most position correspond to 0^{o}, then for TRANSMIT RIGHT, the specular angle increased from 0^{o} to 15^{o}, and for TRANSMIT LEFT, it decreased from 30^{o} to 15^{o}.

The balloon was constructed of adjacent gores, each subtending an angle of $\frac{180^{o}}{53} \sim 3.4^{o}$. The sector of the balloon corresponding to $0^{o} - 15^{o}$ contained two adjacent reinforced gores; therefore, the patterns corresponding to TRANSMIT RIGHT represent a specular angle which passes over the reinforced gores, and those corresponding to TRANSMIT LEFT, a specular angle which does not pass over the reinforced gores.

D.2 BACKGROUND LEVELS

The radar cross-section of a conducting sphere, 67.5 feet in diameter, is 1335 m^2, or 31.2 db > m^2. Following usual practice in cross-section measurements, it was felt that to validate the measurements, the background levels must be maintained at least 10 db and preferably 20 db below this nominal value. The antennas being located 167.5 ft from the center of the 67.5 foot (radius) balloon, the balloon subtended an angle of 44^{o} of the antenna beam. Antenna patterns of the standard gain horns were measured at the Conductron Range. At 22^{o}, the poorest of the horns (in terms of beamwidth) had a power gain of - 12 db relative to its peak. Therefore, any power radiated past the balloon and reflected from the back wall of the hangar was, automatically, 12 db below the specularly reflected power. The background levels in the hangar were found, prior to balloon inflation, by mounting a transmitter on a crane, and transmitting from the nominal location of the center of the balloon. Receiving antennas were also mounted on cranes and moved along the planned position of the receiver track. The data was calibrated and the signal power received was found to be 20 to 30 db below the nominal return from the balloon.

A more serious background effect was direct cross-coupling between the transmitting and receiving antenna. In preliminary tests, there was superimposed upon the cross-section pattern a sinusoidal oscillation which decreased as the bistatic angle increased. This oscillation occurred in both frequency bands. The period of the oscillation was consistent with side lobe coupling, since the maxima and minima occurred when the antenna separation was such that postulated sidelobes would be, respectively, in and out of phase. In any event, dielectric absorber sheets were placed next to the transmitting antennas, shielding them from the receiving antennas. The result was to eliminate completely the apparent coupling at C-band, and to reduce it to a maximum of 1.5 db at L-band.

It was not felt that this last residual coupling compromised the data because it was clearly identifiable, and could be taken into account in the analysis and reduction task.

D.3 DATA CORRECTION

Each calibration consisted of four measurements. As noted above, a secondary source was adjusted to locate the receiver pen midway between two flat plate maxima before each test series and compared to two flat plate maxima after each test series. Using all of the calibrations so obtained, the mean calibration level at L-Band was 25.5 db and 36.7 db at C-Band. At both bands, the standard deviation was less than 1/2 db.

Because the antennas were located in the near zone of the balloon, it was necessary to apply the near zone correction to the data. In Section D.7, the derivation of the near zone correction for a sphere is derived. Taking into account the fact that the bistatic angle 2α is less than 30^{o}, the formula at the bottom of page of the appendix shows that the measured magnitude of the bistatically scattered field is

$$E^{(m)} = E_o \frac{a}{2r},$$

where E_o is the magnitude of the incident field, a is the radius of the sphere, and r is the distance of the antennas from the center of the sphere. If the magnitude of the field backscattered by the calibration plate, is $E^{(c)}$, then

$$E^{(c)} = \frac{1}{\sqrt{4\pi (r - a)^2}} \sqrt{\sigma^{(c)}}$$

where $\sigma^{(c)}$ is the cross section of the calibration plate. But then, the measured cross section $\sigma^{(m)}$ is

$$\sigma^{m} = \left(\frac{E^{m}}{E^{c}} \right)^2 \qquad \sigma^{(c)} = (\pi a^2) \left\{\frac{r - a}{r}\right\}^2.$$

Thus, the true cross section, πa^2, is

$$\left(\frac{r}{r - a}\right) \sigma^{(m)};$$

for $r = 167.5$, $r - a = 100$

$$\pi a^2 = \left(\frac{r}{r - a}\right)^2 \sigma^{(m)} = (1.67)^2 \sigma^{(m)},$$

or

$$\pi a^2 = \sigma^{(m)} + 4.5 \text{ db.}$$

Thus, the near-field measured cross section must be increased by 4.5 db to obtain the true cross section.

The antenna taper, previously mentioned in connection with background levels has an effect upon the data. At the maximum bistatic angle, that part of the balloon which is most significant for scattering, i.e., that part in the neighborhood of the bistatic angle bisector, is at the 9.5° point of the antenna pattern, with a consequent power loss. The resulting data correction is:

+ 3 db, at L-Band, horizontal polarization
+ 2.2 db, at L-Band, vertical polarization,
+ 5 db, at C-Band, horizontal polarization, and
+ 4 db, at C-Band, vertical polarization.

These corrections must be applied to the measured cross section at bistatic angles of 30°. For lesser bistatic angles, we have interpolated linearly.

D.4 THE STATIC INFLATION TESTS

During the period, 1 June - 10 August, 1963, three A-12 balloons were inflated. Balloon No. 9 was initially inflated to check out systems. Balloon No. 11 was then inflated to rupture, Balloon No. 9 was reinflated to rupture, and Balloon No. 13 was inflated to rupture. R.F. data was obtained for all three balloons. For balloons No. 9 and No. 11, measurements were made at 1.71 KMC, 5.65 KMC, and 5.85 KMC. The test procedure was to inflate the balloon to a given nominal surface stress, to maintain the stress while a complete R.F. test sequence was performed, to reduce the stress to approximately 500 psi, and to perform the test sequence again in this "relaxed" condition. This was then repeated at a higher pressure, until rupture. It was very quickly observed that the HV cross sections were, with few exceptional points, well down in the background.

To analyze the data, it was decided to divide the balloon into 5° intervals. After making the corrections to the data noted above, the average cross section on each 5° interval was measured using a planimeter, and the scintillation on the interval (i.e., the difference, in db, between the maximum and minimum cross section. There was not enough difference between the 5.65 KMC and 5.85 KMC data to warrant considering both, so 5.85 KMC was chosen. The results are shown in Tables D-1 and D-2. The columns headed 0, 5, 10, 15, 20, 25, are the 5° intervals starting from the right (reinforced gore)[1]. The entries under "m" are the mean values relative to the nominal balloon, and the entries under "$\pm$" are the scintillations.

Balloon No. 13 was designated to be the prime data balloon. In order to keep the balloon under stress for shorter periods of time, it was decided to omit the 5.65 KMC measurement and to perform cross polarization measurements only as spot checks. The results are listed in Table D-3.

[1] For Nos. 11 and 13 Balloons. For No. 9 Balloon, the reinforced gore was on the left.

TABLE D-1

MEAN VALUES AND SCINTILLATIONS OVER 5° INTERVALS

NO. 11 BALLOON

Pattern #	Psi		0		5		10		15		20		25	
			m	±	m	±	m	±	m	±	m	±	m	±
46 - 63	750	L_V	0	10	-4	28	0	8	-1	7	0	6	0	4
		L_H	2	10	-3	30	1	8	0	4	1	3	1	3
		C_V	1	9	-1	23	-1	14	-2	7	1	9	0	4
		C_H	0	9	0	28	-1	19	-3	9	1	7	0	4
82 - 99	1500	L_V	1	8	-2	33	0	6	0	5	1	3	0	4
		L_H	1	12	-1	28	1	8	1	6	2	4	1	4
		C_V	0	9	-2	21	0	13	-4	4	-1	8	-1	5
		C_H	0	10	-1	21	-1	15	-3	6	-1	9	-1	4
126 - 143	2780	L_V	1	8	-1	26	1	6	0	6	2	3	1	3
		L_H	1	7	0	27	2	8	1	5	2	3	2	3
		C_V	1	8	0	18	1	9	-2	3	0	4	-1	3
		C_H	0	9	-1	18	0	8	-1	5	1	5	0	4
162 - 179	4800	L_V	1	6	0	19	0	7	1	4	2	3	1	5
		L_H	2	9	0	17	2	4	3	3	4	4	2	3
		C_V	1	6	1	12	1	3	0	1	0	3	-1	3
		C_H	0	4	0	12	1	3	1	2	1	2	0	2
180 - 197	500	L_V	2	9	1	23	1	7	2	3	3	3	2	3
		L_H	3	8	1	22	1	5	2	4	4	3	2	3
		C_V	0	6	-1	16	0	7	-2	3	-1	5	-1	4
		C_H	0	7	-1	15	0	7	0	3	0	5	-1	3

TABLE D-2

MEAN VALUES AND SCINTILLATIONS OVER 5° INTERVALS

NO. 9 BALLOON

Pattern #	Psi		m	±	m	±	m	±	m	±	m	±	m	±
202 - 217	750	L_V	-1	4	-1	3	-1	6	-3	8	-5	17	-1	8
		L_H	1	3	1	5	1	5	0	6	-5	23	1	4
		C_V	-3	10	-2	6	-1	9	-4	12	-4	18	-3	19
		C_H	-2	9	-1	6	-1	12	-1	9	-5	17	-2	20

TABLE D-2 Cont.

Pattern #	Psi		m^0	±	m^5	±	m^{10}	±	m^{15}	±	m^{20}	±	m^{25}	±
230 - 241	1500	L_V	0	5	-1	3	0	4	-1	5	-3	20	0	5
		L_H	0	4	0	4	1	5	0	3	-4	12	1	5
		C_V	-2	10	-4	6	-4	12	-2	9	-5	13	-3	19
		C_H	-2	9	-1	5	0	12	-1	9	3	15	-2	20
260 - 269	2600	L_V	1	6	0	3	1	4	0	4	-2	12	1	4
		L_H	1	4	2	2	4	4	1	3	-2	13	2	4
		C_V	-1	9	0	5	1	9	-2	6	-5	16	-2	16
		C_H	-1	9	-1	5	0	10	0	6	-4	16	-1	15
280 - 289	4800	L_V	1	5	0	2	1	4	1	5	-4	11	1	4
		L_H	1	5	1	2	2	5	1	3	-1	7	2	3
		C_V	0	7	1	3	2	7	0	4	-2	8	1	12
		C_H	0	7	1	5	2	7	1	5	-2	10	0	10
290 - 299	500	L_V	1	4	0	4	2	5	1	3	-2	13	2	4
		L_H	1	5	1	4	0	5	2	3	-1	11	2	5
		C_V	0	9	1	6	1	7	1	6	-2	11	0	13
		C_H	0	8	0	5	0	11	3	7	-1	12	0	13

TABLE D-3

MEAN VALUES AND SCINTILLATION OVER 5^o INTERVALS

NO. 13 BALLOON

Pattern #	Psi		m^0	±	m^5	±	m^{10}	±	m^{15}	±	m^{20}	±	m^{25}	±
312 - 329	400	L_V	3	5	0	3	0	4	0	4	0	3	0	4
		L_H	2	4	1	3	0	4	3	4	3	4	1	2
		C_V	5	6	4	11	6	7	2	5	2	6	3	8
		C_H	5	7	3	12	3	6	3	8	2	6	3	7
322 - 339	1500	L_V	2	3	0	3	-1	3	1	3	1	2	2	4
		L_H	2	3	1	3	1	2	3	2	2	3	3	4
		C_V	2	4	3	8	1	7	-1	5	-2	4	-1	6
		C_H	0	5	3	9	1	8	1	4	-1	5	0	6

TABLE D-3 Cont.

Pattern #	Psi		m^0	±	m^5	±	m^{10}	±	m^{15}	±	m^{20}	±	m^{25}	±
340 - 347	2800	L_V	2	3	1	3	-1	2	1	3	2	4	2	4
		L_H	1	2	0	3	-2	5	2	2	2	2	2	3
		C_V	0	3	1	5	-1	6	-2	6	-2	6	-1	7
		C_H	0	4	1	8	-2	9	0	5	1	5	1	5
348 - 359	4800	L_V	2	1	1	2	0	3	0	3	1	5	1	3
		L_H	2	1	2	2	0	3	2	3	3	3	2	2
		C_V	1	3	1	5	1	4	-1	5	0	5	0	5
		C_H	0	5	1	5	0	6	0	4	1	6	1	5
360 - 371	500	L_V	2	2	1	3	1	4	-1	3	-1	5	0	4
		L_H	1	2	1	3	0	5	1	4	2	3	1	4
		C_V	0	5	1	7	1	5	-1	5	-1	5	0	6
		C_H	0	5	0	7	-1	7	0	5	0	5	0	5
372 - 383	7400	L_V	1	1	1	3	0	2	-2	3	-1	5	0	3
		L_H	2	2	1	4	0	3	1	3	1	3	1	2
		C_V	0	4	1	3	0	4	-2	6	-1	6	0	2
		C_H	0	3	1	5	-1	7	-2	8	1	6	-1	3
384 - 393	500	L_V	2	2	1	2	0	3	-1	3	0	4	0	4
		L_H	1	2	1	3	0	5	2	2	2	3	2	3
		C_V	0	6	1	6	0	6	-2	7	0	5	-1	5
		C_H	-1	6	1	6	0	7	-2	6	-1	5	-1	6

D.5 DISCUSSION OF THE RESULTS

For the prime data balloon No. 13, we are interested in the mean values and scintillation as functions of frequency, pressure, and polarization. To exhibit this dependence, we have chosen to display the data in the following tables, Table D-4 and Table D-5.

TABLE D-4

PSI	m - REINFORCED GORE L_V	L_H	C_V	C_H	m - SUMMED OVER OTHER GORES* L_V	L_H	C_V	C_H
400	0	1	4	3	3	9	18	18
1500	0	1	3	3	5	11	-1	1
2800	1	0	1	1	6	5	-6	0
4800	1	2	1	1	4	9	0	2
500	1	1	1	0	-1	5	-1	-1
7400	1	1	1	1	-2	5	-3	-3
500	1	1	1	1	1	7	-3	-5

*These sums, when divided by 5, give the average values of m and ± for the unreinforced part of the balloon.

TABLE D-5

	± - REINFORCED GORE				± - SUMMED OVER OTHER GORES*			
PSI	L_V	L_H	C_V	C_H	L_V	L_H	C_V	C_H
400	3	3	11	12	20	18	32	34
1500	3	3	8	9	15	14	26	28
2800	3	3	5	8	16	14	28	28
4800	2	2	7	7	15	14	22	26
500	3	3	7	7	18	18	31	27
7400	3	4	3	5	14	13	22	27
500	2	3	6	6	16	15	29	30

These tables are self-explanatory and represent the final reduction of the data obtained on the No. 13 balloon. They reveal several clear, albeit slight, dependences upon the parameters. It should be borne in mind that first of all, the computations exhibited in the tables in this report have been rounded to the nearest decibel, and that small db differences in cross section can correspond to larger percentage differences in fields, and therefore represent significant physical effects. The data reduction herein has been designed to extract from the raw data an expression of systematic dependence upon parameters. It remains an open question to decide the effects of their dependence upon a particular communications system. Even though the scintillations in the radar cross section of an A-12 balloon may be large, they are systematic and predictible, and a program to design them out of a communications system through the use of filters is feasible.

*These sums, when divided by 5, give the average values of m and ± for the unreinforced part of the balloon.

D.6 SAMPLES OF RAW DATA

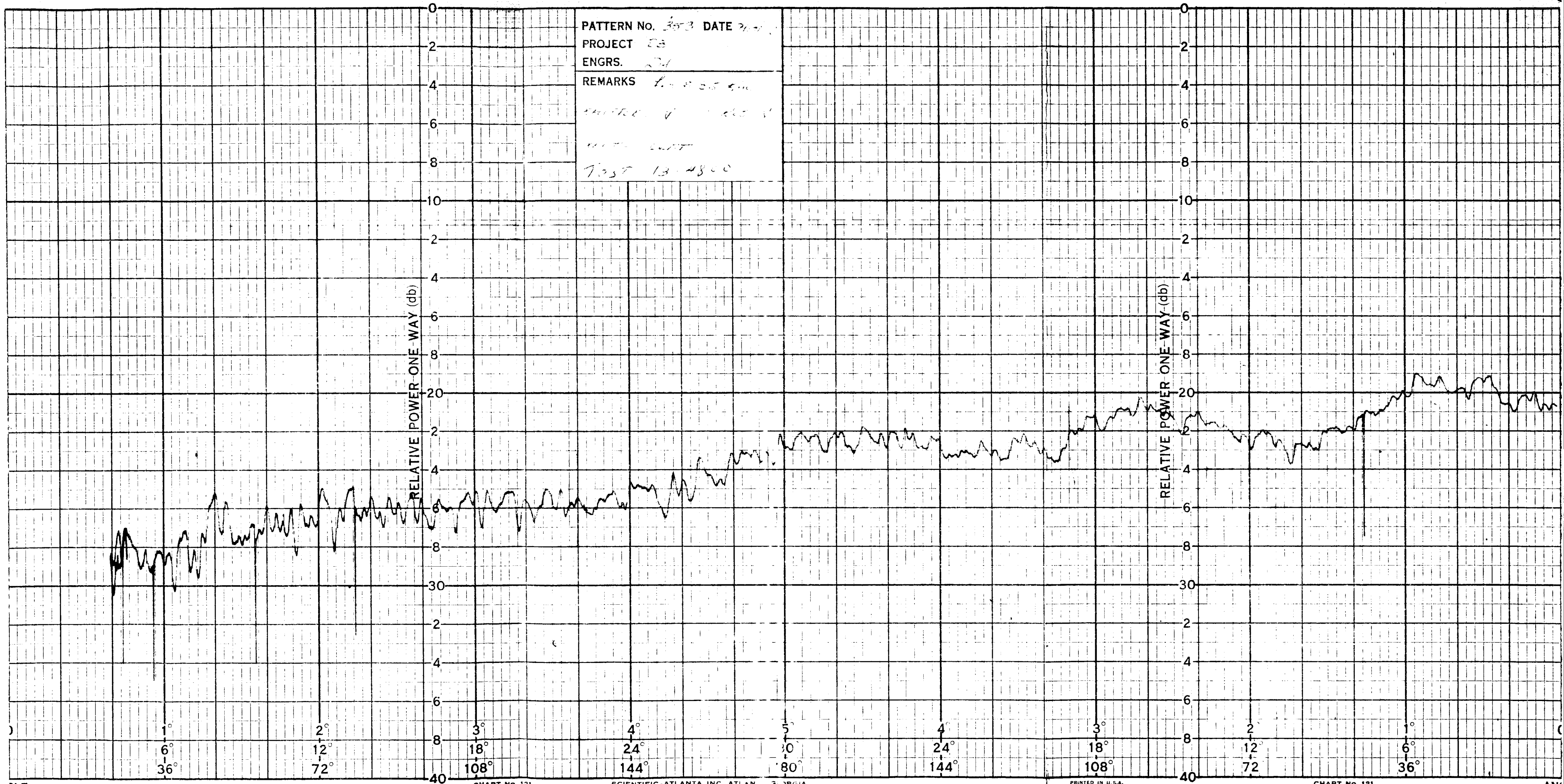
PATTERN No. 353 DATE 2-
PROJECT 28
ENGRS. JM
REMARKS
RELATIVE POWER ONE-WAY (db)
0
2
4
6
8
10
20
30
40
1°
6°
36°
2°
12°
72°
3°
18°
108°
4°
24°
144°
5°
30°
180°
4°
24°
144°
3°
18°
108°
2°
12°
72
1°
6°
36°
CHART No. 121
SCIENTIFIC-ATLANTA, INC., ATLANTA, GEORGIA
PRINTED IN U.S.A.
CHART No. 121

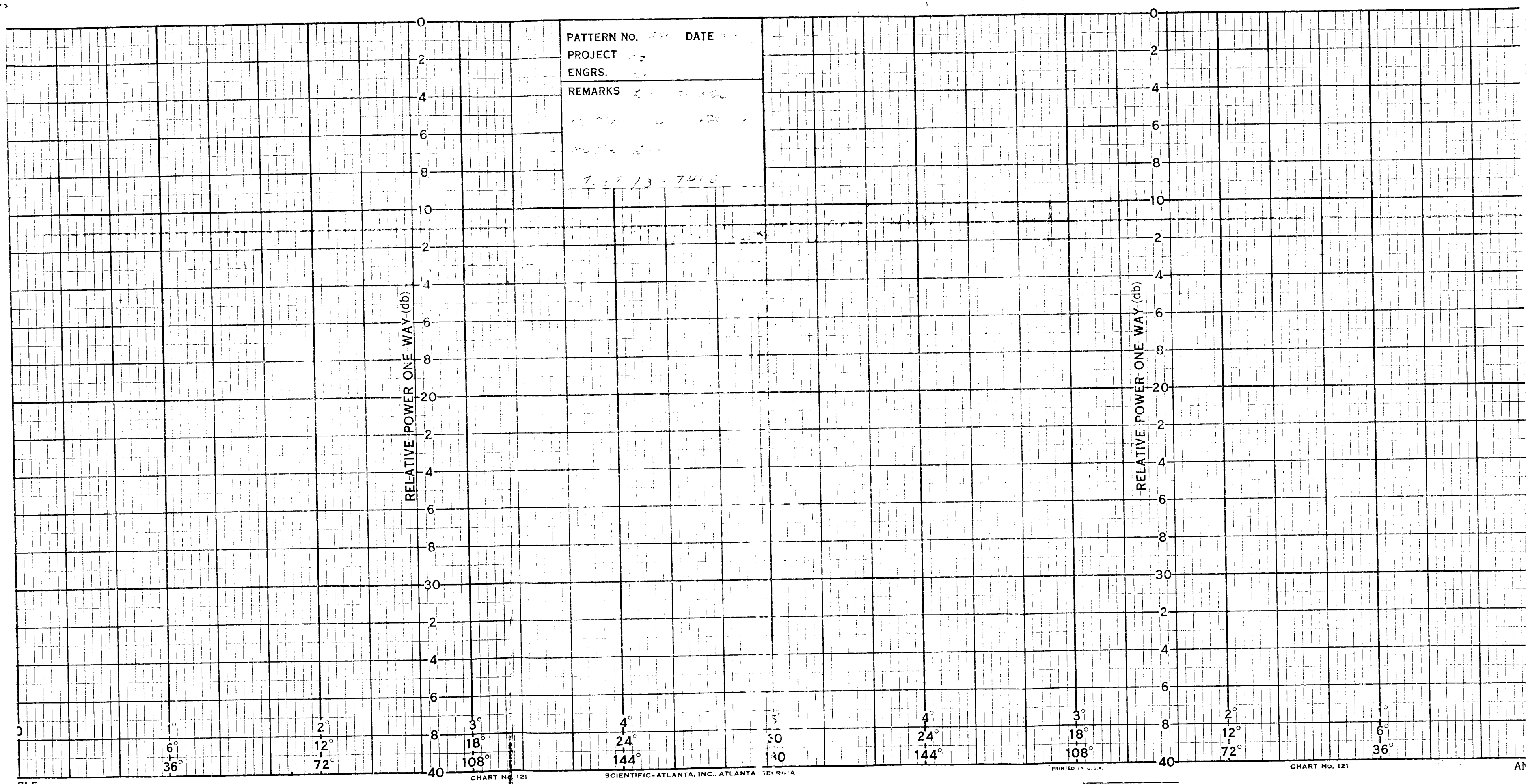
PATTERN No.
DATE
PROJECT
ENGRS.
REMARKS
RELATIVE POWER ONE WAY (db)
0
2
4
6
8
10
20
30
40
1°
6°
36°
2°
12°
72°
3°
18°
108°
4°
24°
144°
CHART No. 121
SCIENTIFIC-ATLANTA, INC., ATLANTA, GEORGIA
PRINTED IN U.S.A.

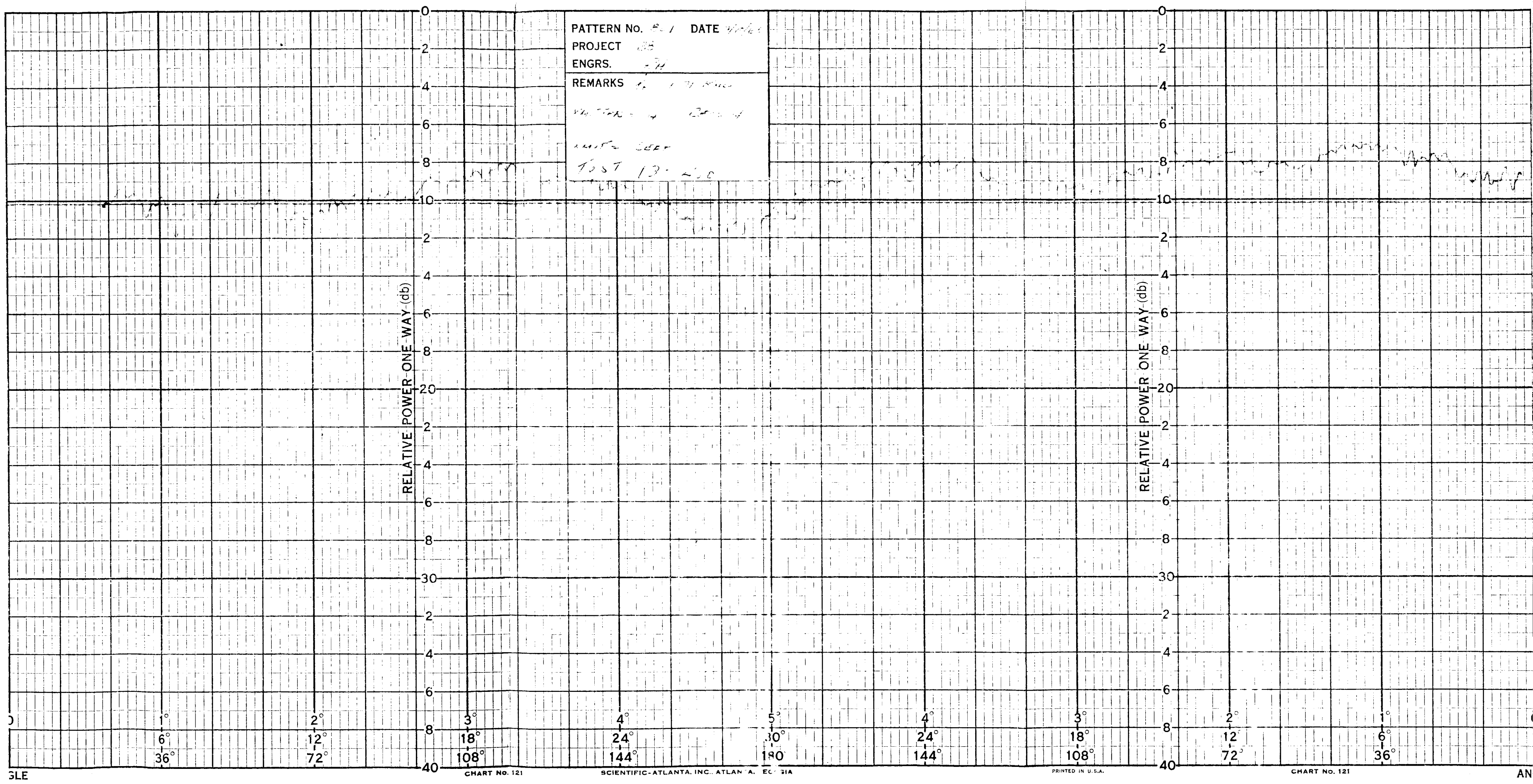
PATTERN No.
DATE
PROJECT
ENGRS.
REMARKS
RELATIVE POWER ONE WAY (db)
0
2
4
6
8
10
20
30
40
1°
6°
36°
2°
12°
72°
3°
18°
108°
4°
24°
144°
5°
30°
180
CHART No. 121
SCIENTIFIC-ATLANTA, INC., ATLANTA, GEORGIA
PRINTED IN U.S.A.

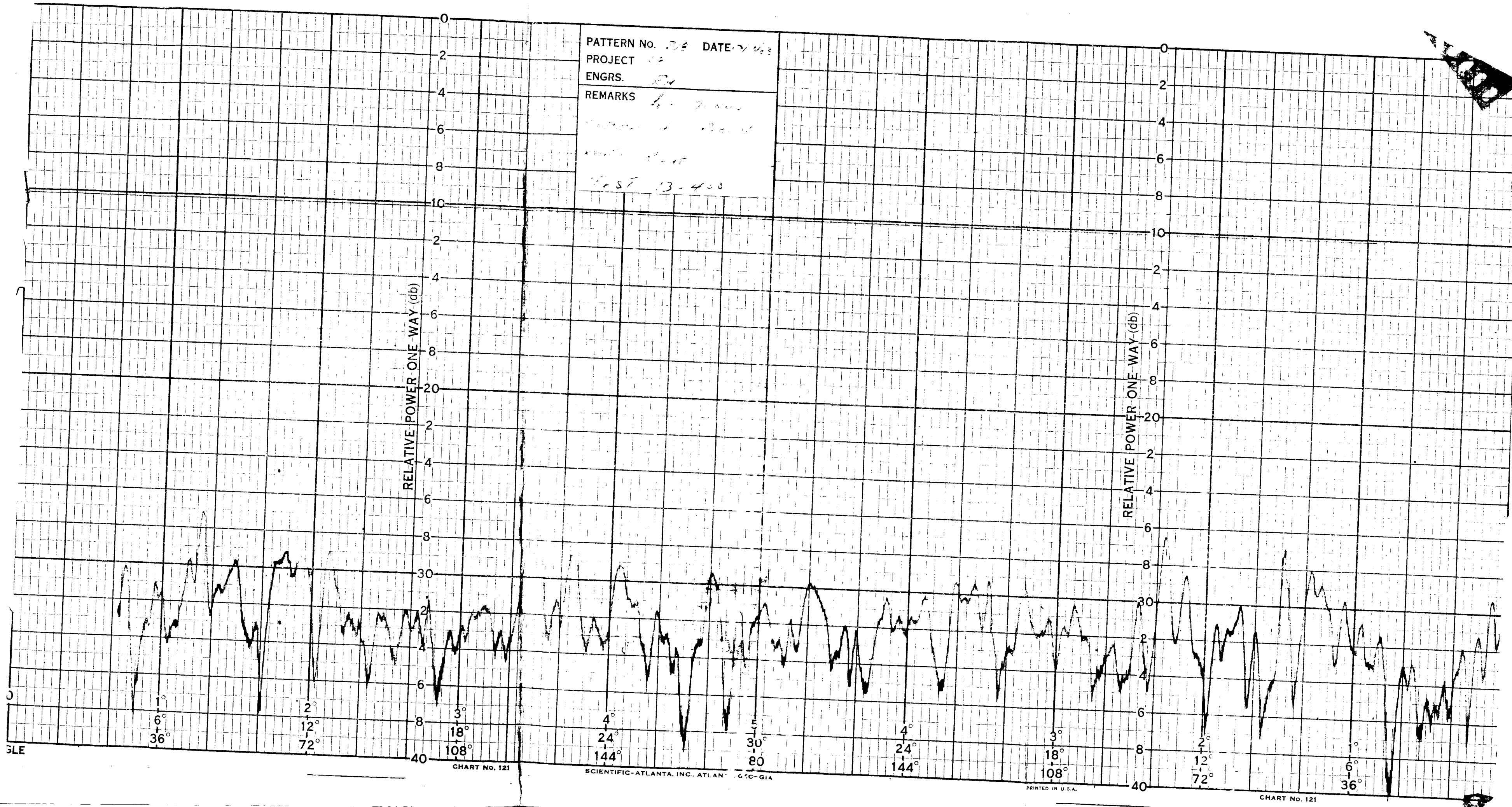
PATTERN No.
DATE
PROJECT
ENGRS.
REMARKS
RELATIVE POWER ONE-WAY (db)
0
2
4
6
8
10
20
30
40
1°
6°
36°
2°
12°
72°
3°
18°
108°
4°
24°
144°
5°
30°
80
CHART No. 121
SCIENTIFIC-ATLANTA, INC., ATLANTA, GEORGIA
PRINTED IN U.S.A.

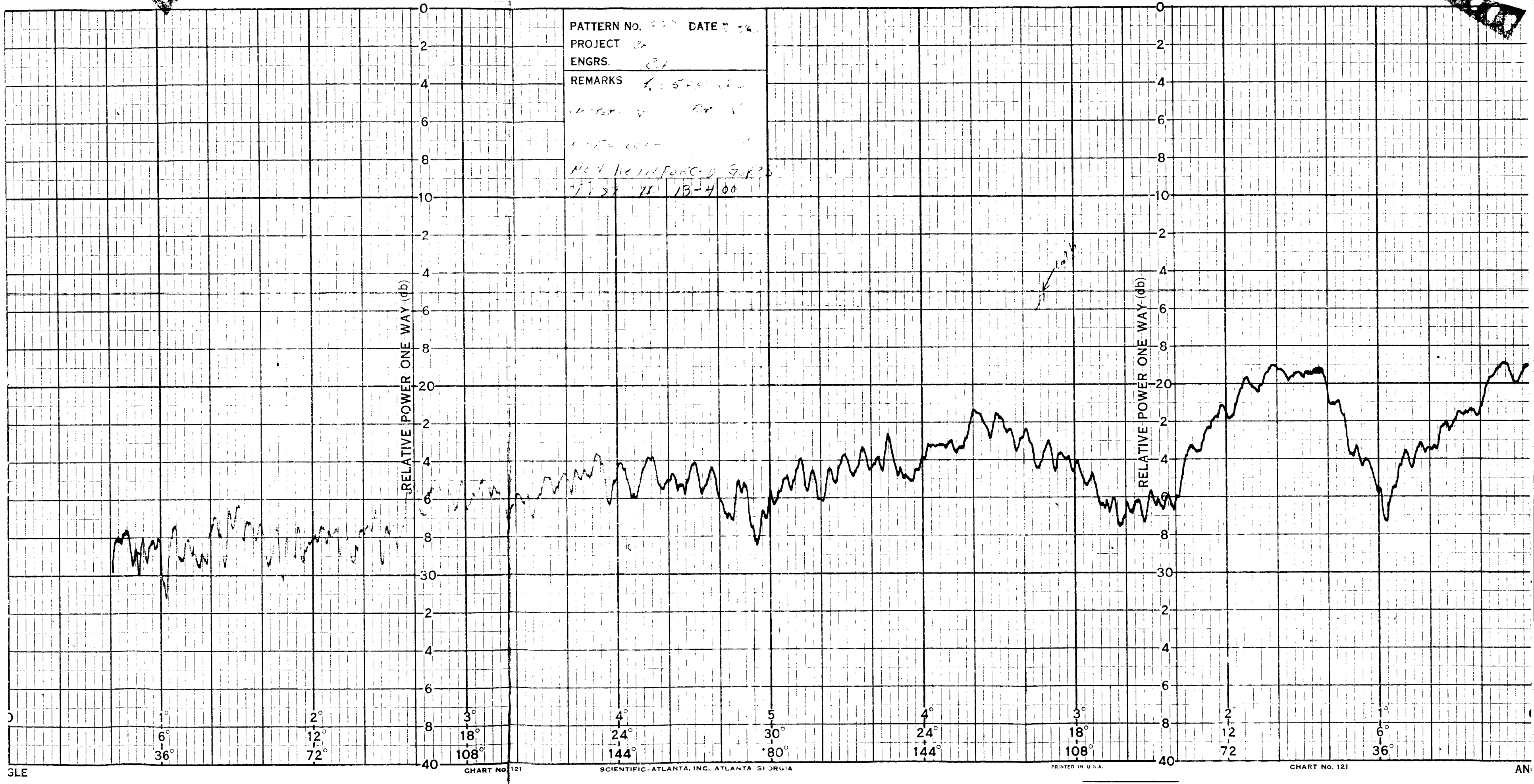
PATTERN No.
DATE
PROJECT
ENGRS.
REMARKS
RELATIVE POWER ONE-WAY (db)
0
2
4
6
8
10
20
30
40
1°
6°
36°
2°
12°
72°
3°
18°
108°
4°
24°
144°
5
30°
80°
4°
24°
144°
3°
18°
108°
2°
12
72
1°
6°
36°
CHART No. 121
SCIENTIFIC-ATLANTA, INC., ATLANTA GEORGIA
PRINTED IN U.S.A.
CHART No. 121

D.7 NEAR-ZONE BISTATIC SCATTERING BY A SPHERE

The high frequency near-zone bistatic scattering by a perfectly conducting sphere for a receiver in the illuminated region is considered. For large values of ka, where k is the free space wave number and a is the radius of the sphere, the dominant contribution comes from the region of the specular point with the diffracted field being insignificant. In particular, for the present case ka is the order of 2×10^3. The near zone bistatic field can be obtained using the Kline-Luneberg asymptotic expansion, for which the analysis was worked out by Schensted [1] for plane wave incidence on bodies of revolution.

D.7.1 Bistatic Scattering for Plane Wave Incidence

Let a plane wave travel in the direction of the positive z-axis and polarized in the x direction. Consider a sphere of radius a, whose illuminated portion of the surface is given by

$$z = f(\rho) = a - \sqrt{a^2 - \rho^2} \qquad \text{(D-1)}$$

where

$$\rho = \sqrt{x^2 + y^2}.$$

The scattered field has the form

$$\underline{E}^s = e^{iks} \sum_{n=0} \lambda^n \underline{E}_n \qquad \text{(D-2)}$$

For the case on hand, only the first term given by n = 0 need be considered, since the remainder of the expression is the order of $1/(ka)$. The phase factor s is the distance along the incident ray from the z = 0 plane to the specular point, plus the distance along the scattered ray from the specular point to observer. See Figure D-4, s is the distance AB + BP. The leading term of expression (D-2) has the form

$$\underline{E}_o = \left(\frac{\rho}{h_\rho \, h_\phi} \right)^{1/2} (-\cos \phi \, \hat{\underline{\rho}} + \sin \phi \, \hat{\underline{\phi}}) \qquad \text{(D-3)}$$

where for the observation point P, ρ is the distance of the specular point B from the z-axis. If the bistatic angle ABP is defined to be 2α, then we have

$$\rho = a \sin \alpha \qquad \text{(D-4)}$$

The angle ϕ associated with the position of the observer P is the angle between the y = 0 plane and the plane containing the point P and the z-axis. The values of h_ρ and h_ϕ can be found on using Equations D-1, D-4 and reference [1] to have the form

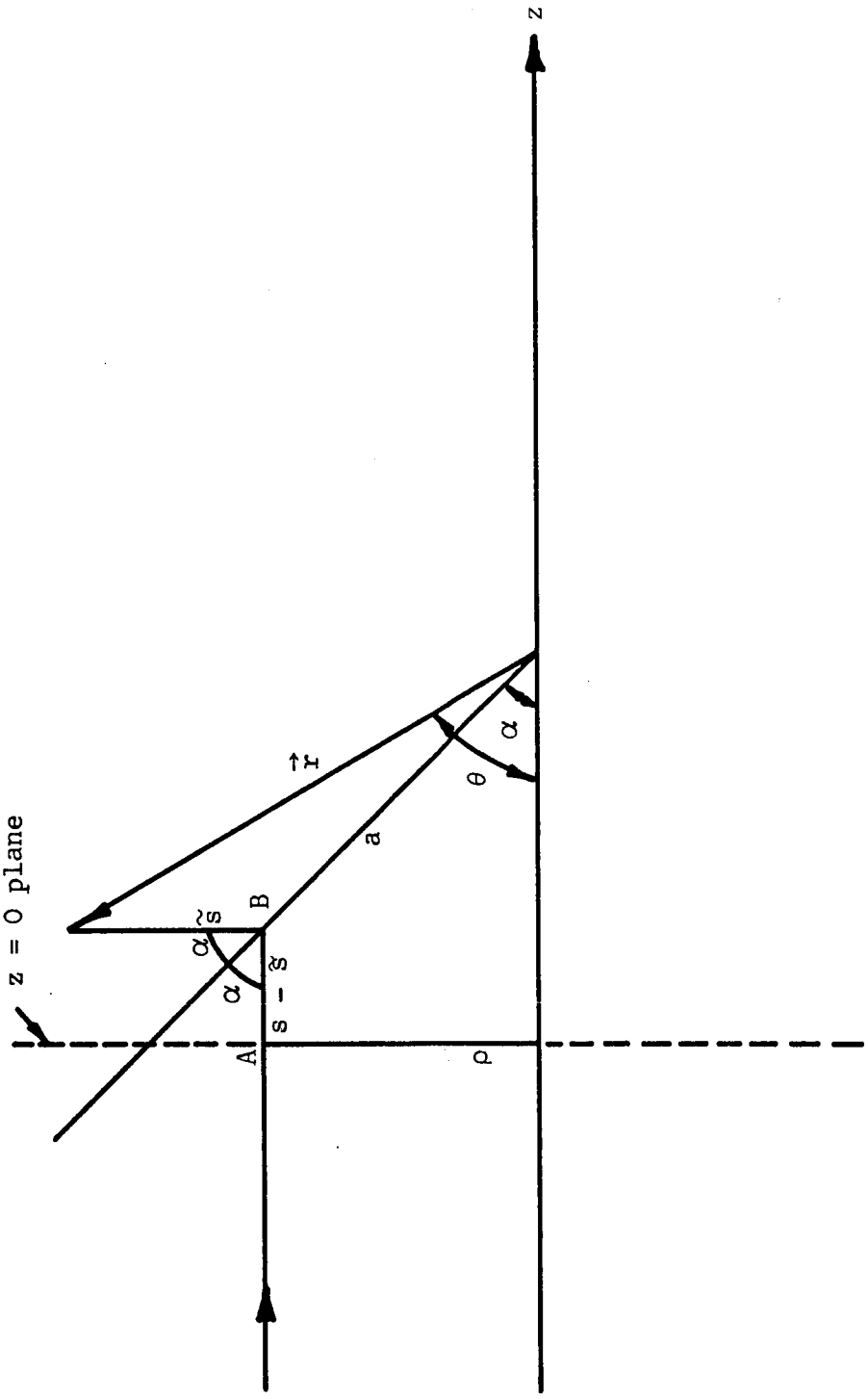

Figure D-4 Relationships Among the Geometric Parameters Defined in Section D.7.1

$$h_\rho = 1 + \frac{2\tilde{s}}{a \cos\alpha}$$

$$h_\phi = a \sin\alpha \left[1 + \frac{2\tilde{s}}{a} \cos\alpha\right] \qquad \text{(D-5)}$$

where $\tilde{s}$ is the distance BP. The vectors $\hat{\phi}$ and $\hat{\rho}$ have the form

$$\hat{\phi} = -\sin\phi\, \hat{i}_x + \cos\phi\, \hat{i}_y$$

$$\hat{\rho} = \cos 2\alpha \left[\cos\phi\, \hat{i}_x + \sin\phi\, \hat{i}_y\right] + \sin 2\alpha\, \hat{i}_z \qquad \text{(D-6)}$$

To complete the picture we need to find $\tilde{s}$ in terms of the angle α and the distance r of the observer from the center of the sphere. It is seen from Figure D-4, that

$$\frac{\tilde{s}}{\sin(\theta - \alpha)} = \frac{a}{\sin(2\alpha - \theta)} = \frac{r}{\sin\alpha} \qquad \text{(D-7)}$$

Solving the last two equations for $\theta - \alpha$, we have obtained

$$\frac{\sin(\theta - \alpha)}{\sin\alpha} = -\frac{a}{r}\cos\alpha + \sqrt{1 - \left(\frac{a}{r}\right)^2 \sin^2\alpha} \qquad \text{(D-8)}$$

thus giving

$$\tilde{s} = a\left[-\cos\alpha + \sqrt{\left(\frac{r}{a}\right)^2 - \sin^2\alpha}\right] \qquad \text{(D-9)}$$

Hence combining the above results we obtain

$$\sqrt{\frac{D(o)}{D(s)}} = \left(\frac{\rho}{h_\rho h_\phi}\right)^{1/2} = \left[\left(1 - 2\cos^2\alpha + 2\cos\alpha\sqrt{\left(\frac{r}{a}\right)^2 - \sin^2\alpha}\right)\right. \qquad \text{(D-10)}$$

$$\left. \cdot \left(-1 + \frac{2}{\cos\alpha}\sqrt{\left(\frac{r}{a}\right)^2 - \sin^2\alpha}\right)\right]^{-1/2}$$

D.7.1.1 Relationship Between Near-Zone and Far-Zone Results Let a transmitter be located at point T (Figure D-5). We shall assume that it is sufficiently far away from the sphere so that the specular region lies in the far-zone of the antenna. In addition we shall first assume that locally in the region about the specular point the incident wave can be treated as a plane wave. Let $E^o \underline{i}_x$ be the electric intensity of the incident radiation at the specular point.

The scattered field in the near zone and far zone will be given in Table D-6, for the following two polarizations. Specifically we shall consider vertical and horizontal polarization, where the incident radiation is respectively polarized perpendicular and parallel to the plane formed by the transmitter, the receiver (previously called observer) and the center of the sphere. The scattered field for the horizontal and vertical polarization cases are found by setting $\phi = 0$, and $\phi = \pi/2$ respectively in Equations D-3 and D-6.

As seen from Table D-6, there are no cross-polarization terms. This is because the cross-polarization terms occur in the terms of the series (Equation D-2) which have been neglected, and are of lower order by a factor 5×10^{-4}. The angle 2α is the far-zone bistatic angle. To extrapolate far-zone results from near zone results this angle must be fixed.

We next come to the question of changing the assumption of plane wave incidence. A more accurate assumption with the transmitter at a finite distance from the sphere is to treat the incidence wave in the neighborhood of the specular point as a spherical wave. The main effect of this is to change the factor $\sqrt{D(o)/D(\tilde{s})}$ given by Equation D-10. For simplicity we will take transmitter and receiver to be the same distance r from the center of the sphere. The "divergence factor" $\sqrt{D(o)/D(\tilde{s})}$ can be obtained from Fock [2],

$$\sqrt{D(o)/D(\tilde{s})} = \frac{a}{2r} \left\{ \frac{\cos \alpha}{M(\frac{a}{r} \sin^2 \alpha + \cos \alpha \, M)} \right\}^{1/2}.$$

$$\text{with } M = \sqrt{1 - (\frac{a}{r} \sin \alpha)^2}$$

Thus if a spherical wave is assumed incident, then Table D-6 must be modified in that the near field magnitude (the second column) must be replaced by

$$E_o \; \frac{a}{2r} \left\{ \frac{\cos \alpha}{M(\frac{a}{r} \sin^2 \alpha + \cos \alpha \, M)} \right\}^{1/2}$$

REFERENCES:

[1] Schensted, C. E., "Electromagnetic and Acoustic Scattering by a Semi-Infinite Body of Revolution," J. Appl. Phys., 26, 3, 306-308 (1955).

[2] Fock, V. A., "Generalization of the Reflection Formulas to the Case of Reflection of an Arbitrary Wave from a Surface of Arbitrary Form, Z.E.T.F., 20, 961-970 (1950).

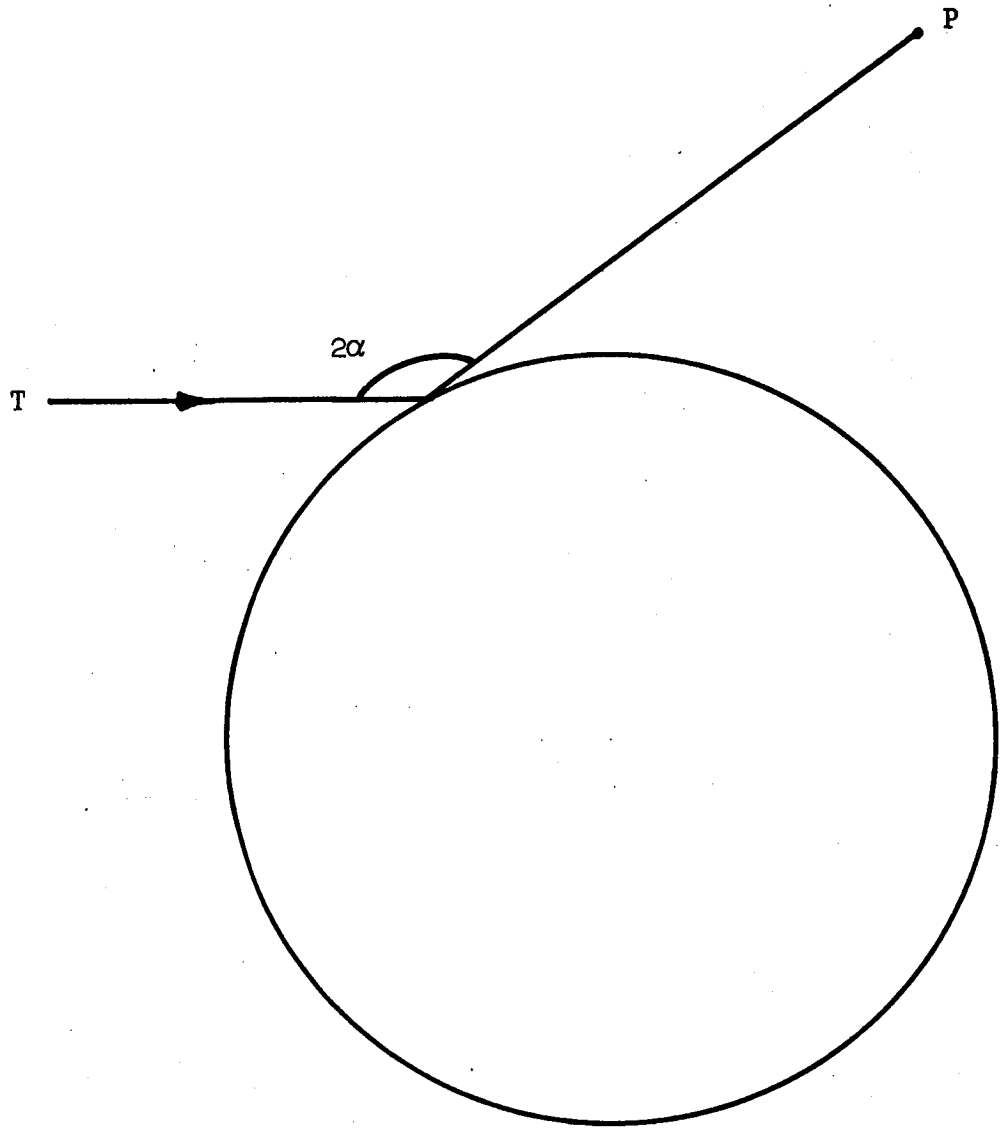

Figure D-5 Bistatic Geometry

T = transmitter
P = receiver
2α = bistatic angle

TABLE D-6

PLANE WAVE INCIDENCE

INCIDENT POLARIZATION	MAGNITUDE NEAR-ZONE SCATTERED FIELD	MAGNITUDE FAR-ZONE SCATTERED FIELD	POLARIZATION OF SCATTERED FIELD
Horizontal	$E_o[1-2\cos^2\alpha+2\cos\alpha L)(-1+\frac{2}{\cos\alpha}L]^{-1/2}$	$E_o \frac{a}{2r}$	Horizontal
Vertical	Same as above	Same as above	Vertical

NOMENCLATURE

r = distance of transmitter from center of sphere
2α = far-zone bistatic angle

$$L = \sqrt{(\frac{r}{a})^2 - \sin^2\alpha}$$

APPENDIX E

E.1 CONDITIONS FOR WHICH PHYSICS OPTICS APPROXIMATION CAN BE USED ON A QUASI-ROUGH PERFECTLY CONDUCTING SURFACE

We shall consider perturbations on a large convex surface the values of curvature of which is everywhere large compared to wavelength. The basic unperturbed surface will be given by $z = g(x, y)$, where the cartesian coordinate system is chosen so that x-y plane is tangent to this surface at the origin. The perturbation will be given by $z = \delta(x, y)$ so that the rough surface is described by

$$z = g(x, y) + \delta(x, y).$$

We shall consider a plane wave incident upon the surface the direction of propagation lying in the x-z plane. Specifically the incident magnetic field intensity is given by

$$\underline{H}^o = \underline{a}\, e^{ik(x \sin\alpha - z \cos\alpha)}$$

where $|\alpha| < \pi/2$.

From Maue* we have the following integral equation for the tangential components of $\underline{H}$ on the surface

$$\frac{1}{2}\,\underline{j}(P) = \underline{j}^o(P) + \int_S [\nabla_Q G \times \underline{j}(Q)] \times \underline{n}(P)\, d S_Q. \qquad (E.1)$$

where

$$\underline{j} = \underline{n} \times \underline{H}$$

$$G = \frac{e^{ikr}}{4\pi r}$$

with $r = |\underline{x}_p - \underline{x}_Q|$

and $\underline{n}$ is the outward normal to the surface. The physical optics approximation that we seek is that

$$\underline{n} \times \underline{H}(\underline{x}) \sim 2\, \underline{n} \times \underline{H}^o(\underline{x}).$$

Hence we shall first assume that

---

* Maue, A.W., Zeit f Physik, 126, pp. 601-618 (1949).

$$\underline{j}(\underline{x}) = \underline{I}(\underline{x})\, e^{ik(x \sin\alpha - z \cos\alpha)}$$

where $\underline{I}(x)$ is a slowly varying function of $(\underline{x})$.

Integral equation (E.1) can then be written in the form

$$\underline{I}(\underline{x}) = 2\,\underline{I}^{o}(x) + \frac{1}{2\pi}\int_{S} \frac{1}{r}\left[ik - \frac{1}{r}\right]\left\{(\underline{\nabla}_Q\, \underline{r} \times \underline{I}_Q) \times \underline{n}_p\right\} e^{ikf}\, d\, S_Q \qquad (E.2)$$

where $f = r + (x' - x)\sin\alpha - (z' - z)\cos\alpha$. (E.2a)

Apart from the exponential factor in the integrand, the integrand is a slowly varying function. Hence we will look for the stationary phase point. This is the point for which

$$\frac{\partial f}{\partial x'} = 0 \qquad (E.3)$$

$$\frac{\partial f}{\partial y'} = 0 \qquad (E.4)$$

where we have taken the coordinates of the point $\underline{x}_Q$ to be (x', y', z') and the variable of integration x' and y' so that

$$n_z\,(x')\, d\, S_Q = dx'\, dy' .$$

One condition on the surface is that $n_z(x') \geq 0$.

The stationary point specified by equations (E.3) and (E.4) satisfy the equations

$$\frac{1}{r}\left\{(x' - x) + (z' - z)\frac{\partial z'}{\partial x'}\right\} + \sin\alpha - \cos\alpha\,\frac{\partial z'}{\partial x'} = 0 \qquad (E.5)$$

$$\frac{1}{r}\left\{(y' - y) + (z' - z)\frac{\partial z'}{\partial y'}\right\} - \cos\alpha\,\frac{\partial z'}{\partial y'} = 0 \qquad (E.6)$$

Set

$$\frac{\underline{x}' - \underline{x}}{r} = \hat{\underline{r}} ,$$

$$(\sin\alpha,\ 0,\ -\cos\alpha) = \hat{\underline{k}} ,$$

$$\underline{P} = \hat{\underline{r}} + \hat{\underline{k}} ,$$

giving from the above

$$P_x = - P_z \frac{\partial z'}{\partial x'}$$

$$P_y = - P_z \frac{\partial z'}{\partial y'} .$$

Thus we have

$$\underline{P} = P_z \left\{ - \frac{\partial z'}{\partial x'} , - \frac{\partial z'}{\partial y'} , 1 \right\}$$

$$|\underline{P}| = \pm P_z \left[1 + \left(\frac{\partial z'}{\partial x'} \right)^2 + \left(\frac{\partial z'}{\partial y'} \right)^2 \right]^{1/2}$$

$$\therefore \underline{P} = \pm |\underline{P}| \; \underline{n} (\underline{x}') .$$

We thus have

$$(\hat{\underline{r}} + \hat{\underline{k}}) = \pm \; |\hat{\underline{r}} + \hat{\underline{k}}| \; \underline{n}$$

with solutions

$$\underline{r} = - \hat{\underline{k}} + \beta \, \underline{n}$$

with

$$\beta = 0 \text{ or } \beta = \pm 2 \, \hat{\underline{k}} \cdot \hat{\underline{n}}.$$

The case where $\beta = 0$ corresponds to observation point $\underline{x}$ being in the penumbra region and the stationary phase point $\underline{x}'$ being in the illuminated region for the body surface being convex.

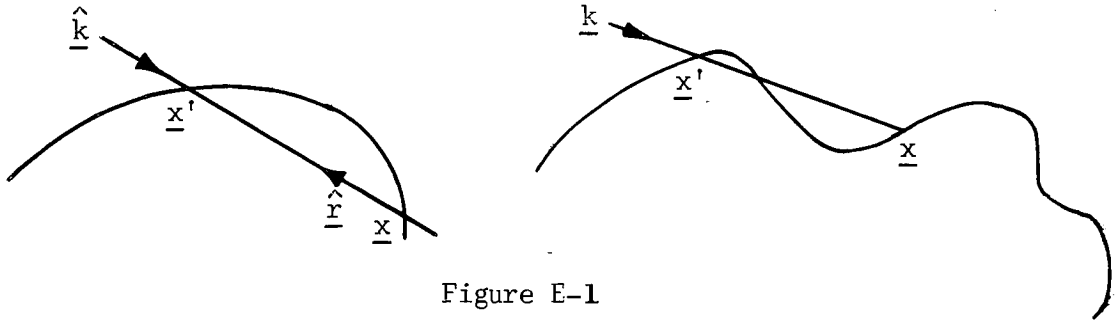

Figure E-1

For large corrugations the point $\underline{x}$ can be in the illuminated region, but there is a shadow corridor separating the two points.

The case where $\beta = 2\,\hat{\underline{k}} \cdot \hat{\underline{n}}$ corresponds to the case where both $\underline{x}$ and $\underline{x}'$ are in the shadow region for a convex surface.

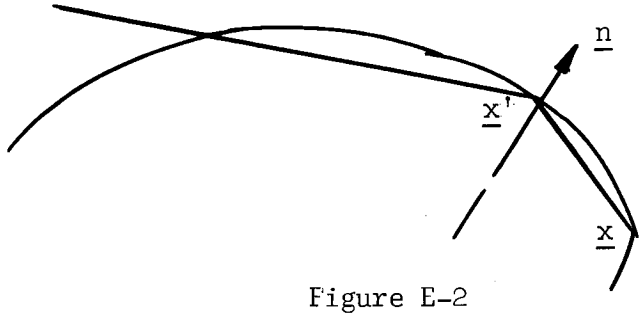

Figure E-2

The case where $\beta = -2\,\hat{\underline{k}} \cdot \hat{\underline{n}}$ corresponds to a concave section of the surface is shown in the diagram.

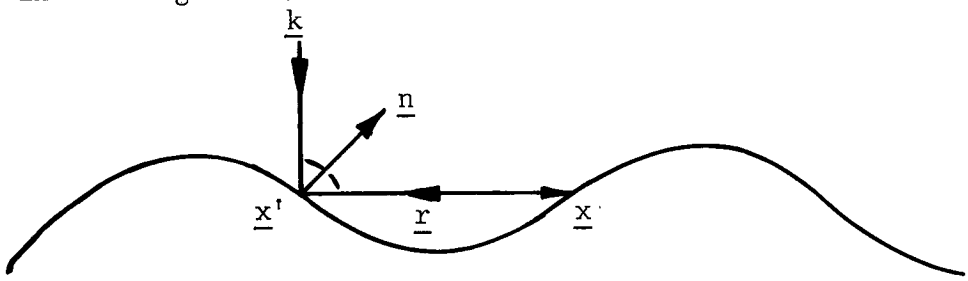

Figure E-3

Physically the stationary point in this case corresponds to multiple scattering.

From these results we see that in order to use physical optics on a region of a perturbed surface, we require these regions to be sure that for the angle of incidence under consideration, there must be no corridors of shadows; and secondly, the perturbed surface must be locally convex everywhere in the domain.

With these restrictions there are no stationary phase points and the main contribution to the integral (E.2) arises from the neighborhood of the point $\underline{x}$.

To evaluate the integral contained in Equation (E.2) we will take $\underline{x} = (0, 0, \delta_o)$. This places no restriction, only specifying the choice of the origin. We will consider the particular case where the unperturbed surface is a very large sphere of radius a, where its equation in the vicinity of origin is given by

$$z = g(x, y) = -\frac{1}{2a}(x^2 + y^2) \tag{E.7}$$

The perturbed surface will be given by

$$z = \delta(x, y) = \delta_o + \epsilon(x, y) \tag{E.8}$$

where δ_o is the value of δ at $x = 0$, $y = 0$. Hence ϵ vanishes at $x = 0$, $y = 0$. In the integrand at the integral on the right hand side of equation (E.2) we can approximate $\underline{I}(\underline{x}')$ by $2\,\underline{n}(\underline{x}') \times \underline{a}$ where $\underline{a}$ is the unit vector denoting the direction of the magnetic intensity vector.

The explicit integral to be considered is

$$\frac{1}{2\pi} \iint \frac{dx'\,dy'}{n_x(\underline{x}')}\, e^{ikf}\, L(x', y') \tag{E.9}$$

where f is given by equation (E.2a) and

$$L = \frac{2}{r}\left(ik - \frac{1}{r}\right)\{\nabla_r' \times [\underline{n}(\underline{x}') \times \underline{a}]\} \times \underline{n}(\underline{x}) \tag{E.10}$$

First we have

$$r^2 = x'^2 + y'^2 + [\epsilon - \frac{1}{2a}(x'^2 + y'^2)]^2$$

and setting $x'^2 + y'^2 = \rho^2$

$$r = \rho[1 + \frac{1}{2}(\frac{\epsilon}{\rho} - \frac{\rho}{2a})^2 + \ldots]$$

where we assume that $|\epsilon/\rho| \ll 1$ as $\rho \to 0$. This last requirement is equivalent to requiring that

$$\left|\frac{\partial \epsilon}{\partial x'}\right| \;,\; \left|\frac{\partial \epsilon}{\partial y'}\right| \ll 1$$

at $x' = 0$, $y' = 0$. This specifies that the slopes of perturbation are small. We require $|\epsilon/\rho| << 1$ for all ρ in a large region about $\rho = 0$. For values of $\rho << a$, we have

$$r \sim \rho + \frac{1}{2}\frac{\epsilon^2}{\rho} - \frac{1}{a}\frac{\rho\epsilon}{a} + \frac{1}{8}\frac{\rho^3}{a^2}$$

Thus for a region about $\rho \sim 0$, we have

$$kf \sim k\rho + \frac{1}{2}\frac{k\epsilon^2}{\rho} - \frac{1}{2}\frac{k\rho\epsilon}{a} + \frac{1}{8}\frac{k\rho^3}{a^2} + k\rho\cos\theta\sin\alpha - \cos\alpha\left\{\epsilon - \frac{\rho^2}{2a}\right\}$$

where $x' = \rho\cos\theta$. This expression can be approximated in the vicinity of $\rho \sim 0$ by

$$kf \sim k\rho\left[1 + \frac{1}{2}\frac{\epsilon^2}{\rho^2} + \cos\theta\sin\alpha - \frac{\epsilon}{\rho}\cos\alpha\right]$$

where we have neglected $(\frac{\epsilon}{a})$ which is extremely small. Thus kf is a rapidly varying function essentially behaving by $k\rho$.

We have assumed that the factor L/n_z in the integrand of expression (E.9) is slowly varying with respect to the exponential. Since the oscillation of exponential is proportional to wavelength, we require that the variation of L/n_z in a distance of a wavelength be small.

The factor L/n_z is a function of the unperturbed surface $g(x, y)$ and the perturbed surface $\delta(x, y)$ together with their first derivatives with respect to x' and y'. However, since the unperturbed surface has very large radius of curvature a, and $ka \gg 1$, then the variation of the above factor's dependence on $g(x, y)$ is very small. The main question concerns the variation with respect to perturbation. Essentially we will require that

$$\left|\frac{\partial^2\epsilon}{\partial x^2}\right| , \left|\frac{\partial^2\epsilon}{\partial y^2}\right| , \left|\frac{\partial^2\epsilon}{\partial x\partial y}\right| << \lambda$$

Going back to the requirement that the surface be convex, additional restrictions can be placed upon ϵ.

The sign of the curvature of the curves formed by the intersection of the surface and the x-constant and y-constant planes will correspond to the signs of

$$\frac{\partial^2}{\partial y'^2}\left\{-\frac{(x'^2 + y'^2)}{2a} + \epsilon\right\} \text{ and } \frac{\partial^2}{\partial x'^2}\left\{-\frac{x'^2 + y'^2}{2a} + \epsilon\right\}$$

respectively. We require that for the surface to be locally convex

$$\frac{1}{a} - \frac{\partial^2\epsilon}{\partial x'^2} > 0$$

$$\frac{1}{a} - \frac{\partial^2\epsilon}{\partial y'^2} > 0$$

Hence for a section of the perturbed surface which is a valley we have

$$0 \leq \frac{\partial^2 \epsilon}{\partial x'^2} < \frac{1}{a}$$

$$0 \leq \frac{\partial^2 \epsilon}{\partial y'^2} < \frac{1}{a}$$

To illustrate the conditions, let the perturbed surface be represented by the form

$$\delta(x, y) = h \cos \ell \times \cos \ell y$$

In this case $h = \delta_o$. It is seen that the requirement $\left|\frac{\partial^2 \epsilon}{\partial x^2}\right| < \frac{1}{a}$ gives rise to

$$\frac{1}{a} > h \ell^2 .$$

Essentially the width d of a hill or valley is given by $d = \frac{\pi}{\ell}$. The above condition then places the following restriction upon the height h of the hill or depth of valley

$$d > \sqrt{\pi^2 h a}$$

For example given a hill of height 1/4" and a ~ 810", we have

$$d > 42".$$

With the above restrictions upon the derivatives of $\epsilon(x', y')$, the leading term of the asymptotic expression for integral (E.9) can be obtained by integrating key parts with respect to the variable ρ and retaining only the lower limit of integration giving

$$-\frac{1}{ik2\pi} \int_0^{2\pi} d\theta \lim_{\rho \to 0} \left[\frac{\rho L}{n_z \frac{\partial f}{\partial \rho}} \right]$$

Evaluation of this integral will give rise to terms of the order $(k R_x)^{-1}$, $(k R_y)^{-1}$ where R_x and R_y are the radii of curvature of the perturbed surface at the point $(0, 0, \delta_o)$. Since these factors are much less than unity, the correction terms given by the above integral to the physical optics term is small.

APPENDIX F

F.1 RADAR CROSS SECTION (NASA BALLOON)

This represents an approach to the problems of predicting the radar cross section of a perturbed spherical surface. The method is basically a consideration of the geometric properties of the perturbations and what their effects would be when imposed on a true spherical shape.

Figures F-1 through F-5 are topographic projections of the deviations from a true sphere of radius r_o = 810 inches. These deviations are the differences in the vertical distance from the true sphere, (see Fgirue F-6), to the perturbed sphere. Each value of the deviation, δ, is given at a lattice point on a six-inch grid and is defined to be positive if the perturbed sphere is above the true sphere and negative if it is below. If a collection of points are all zero, then for that portion of the sphere projected in the x, y plane the perturbed sphere is tangent to the true sphere.

The five figures represent the projections for four gores at three different pressures. The center of the graphs are seam lines between the gores and each gore extends to about the eighth grid on either side of the seam. We have called areas below the true sphere "valleys" and above the true sphere "hills". A "plateau" is an area where the perturbed sphere is above the true sphere, but basically spherical in local geometric character. A "canyon", on the other hand, is a region where a "valley" area is beginning to rise. Small perturbations, from point to point, have not been considered and only the gross topological features described above have been mapped.

Figure F-1 shows the projections for gores 102 and 103 at 2800 psi. In this figure, two features are outstanding, namely a hill rising over 0.2" above the true sphere and a deep valley or pit lying about 0.4" below separated by a distance of around 35". From this figure, it can be seen that the hill starts to bulge on either side of the seam but dips down into a shallow valley on gore 103 where it begins to rise again near the lower side. The upper half and extreme edges of both gores are in general valleys, and seem to be deepening at the edge of gore 102 and rising at the edge of gore 103 except at the extreme upper portion, where it is of course a rather deep pit. Figure F-2 shows the same gores at a pressure of 4800 psi. From this figure, it is seen that little similarity exists between Figures F-1 and F-2 even though they are the same gores. However, it is pointed out that gores 102 and 103 are unreinforced and this may account for the lack of similarity. In Figure F-2, gore 103 is divided about midway by a hill on the left and a valley on the right. This hill extends over the seam to gore 102 where it becomes a plateau about 0.14" above the true sphere. Just below the plateau the hill peaks to almost 0.3", and this is about the only similarity between Figures F-1 and F-2, that is, the hill peaks are in roughly the same location and are about the same height. Figure F-3

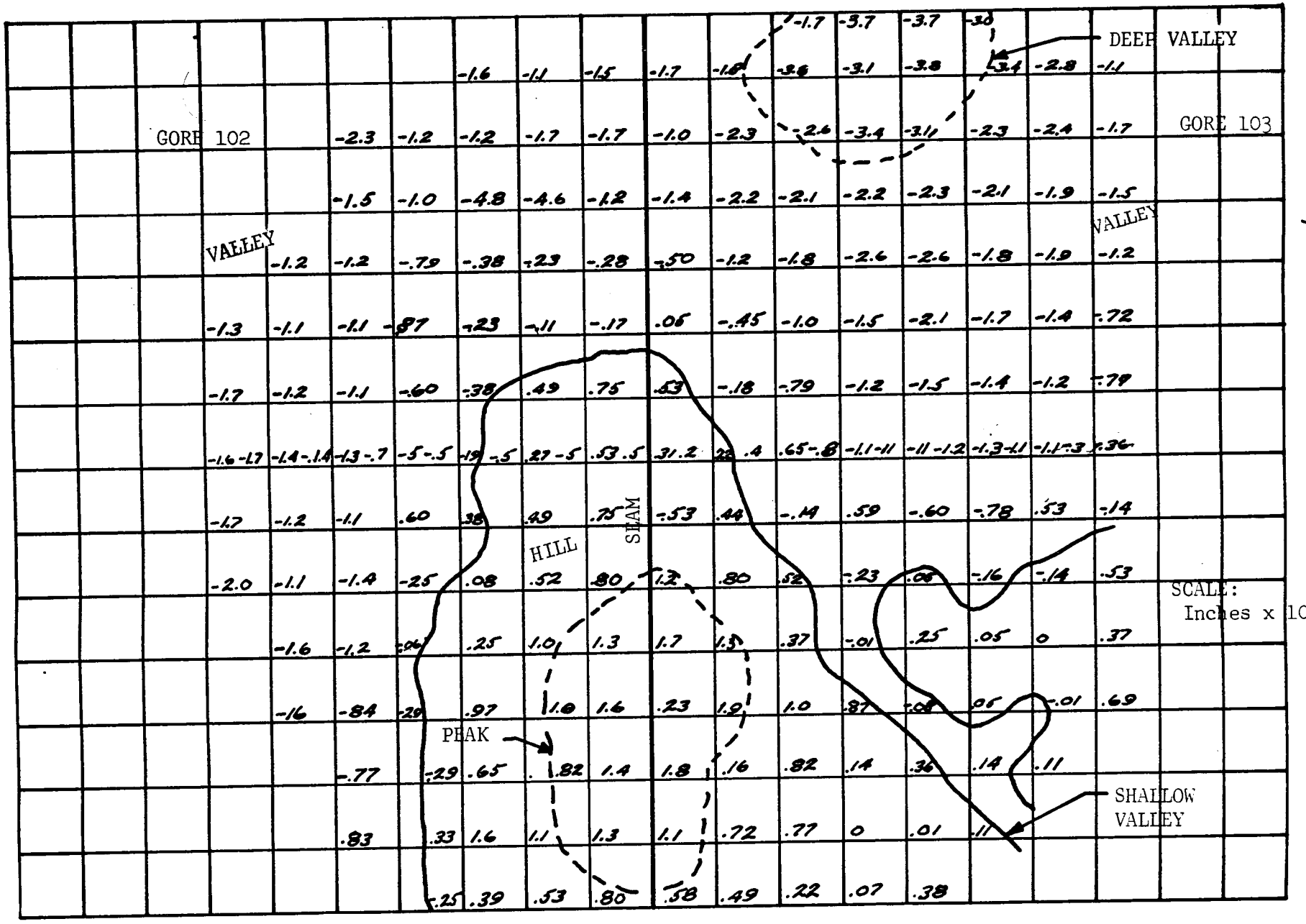

Figure F-1 Contour Map of Gores 103 and 102 at 2800 PSI

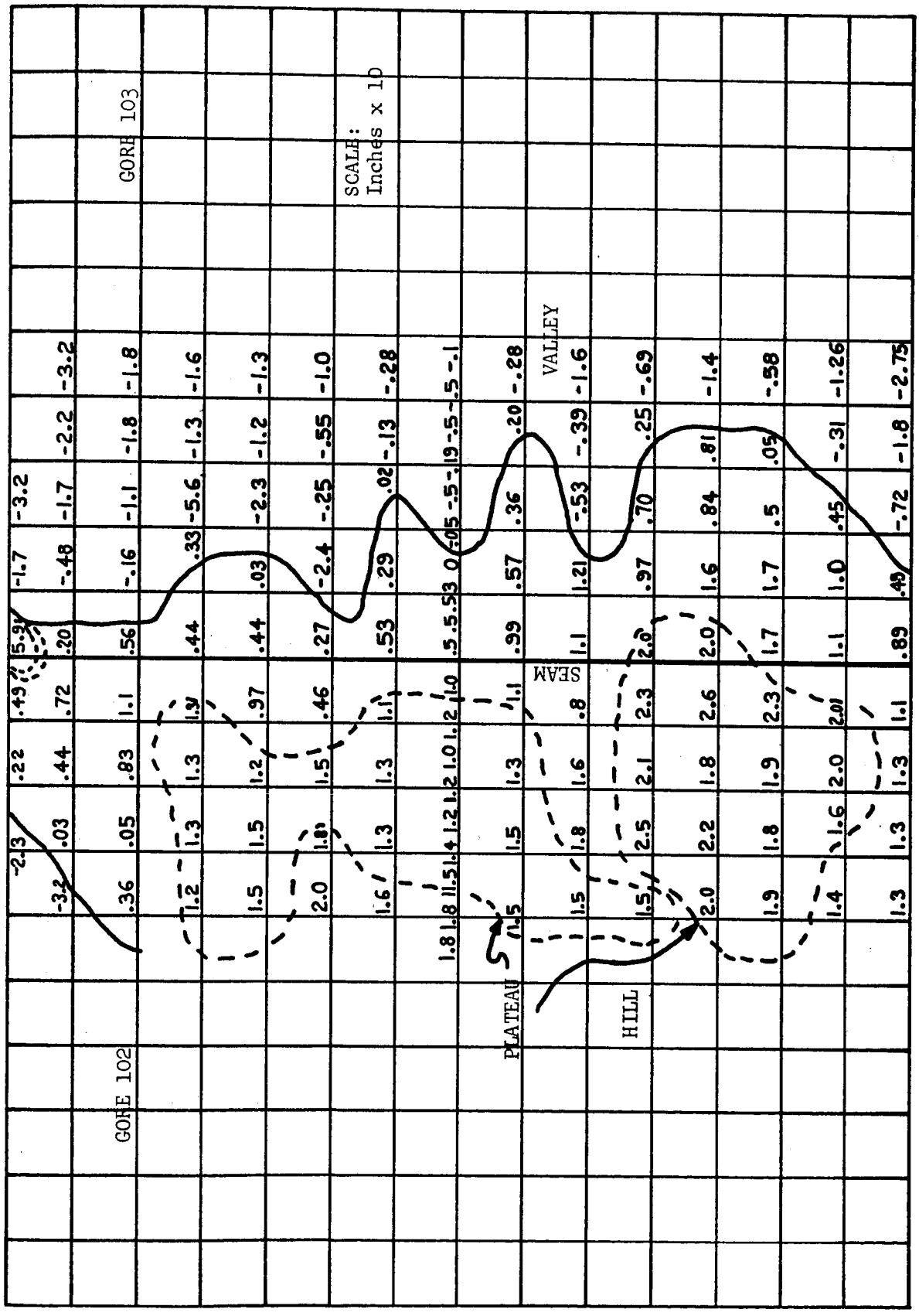

Figure F-2 Contour Map of Gores 102 and 103 at 4800 PSI

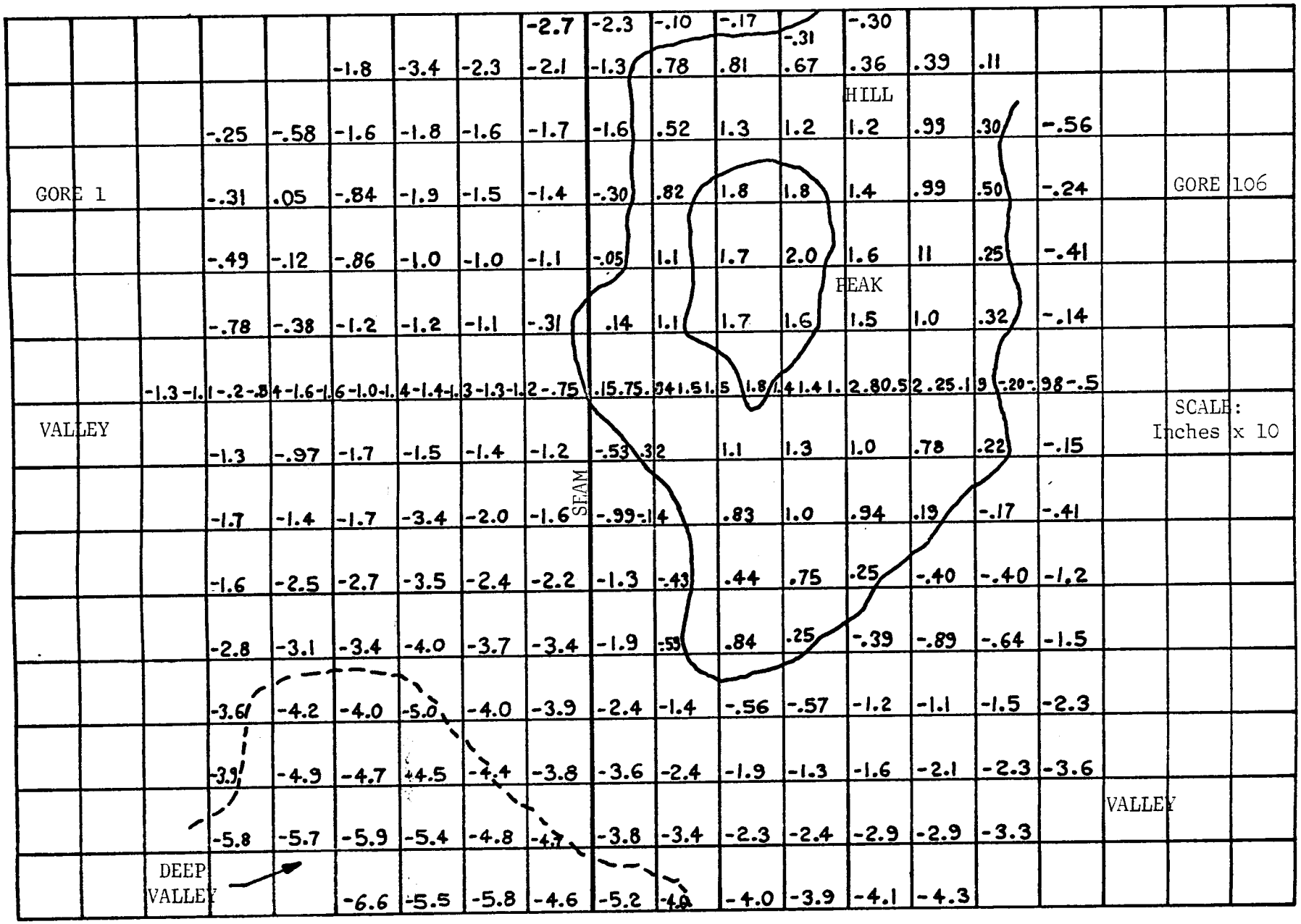

Figure F-3 Contour Map of Gores 106 and 1 at 4800 PSI

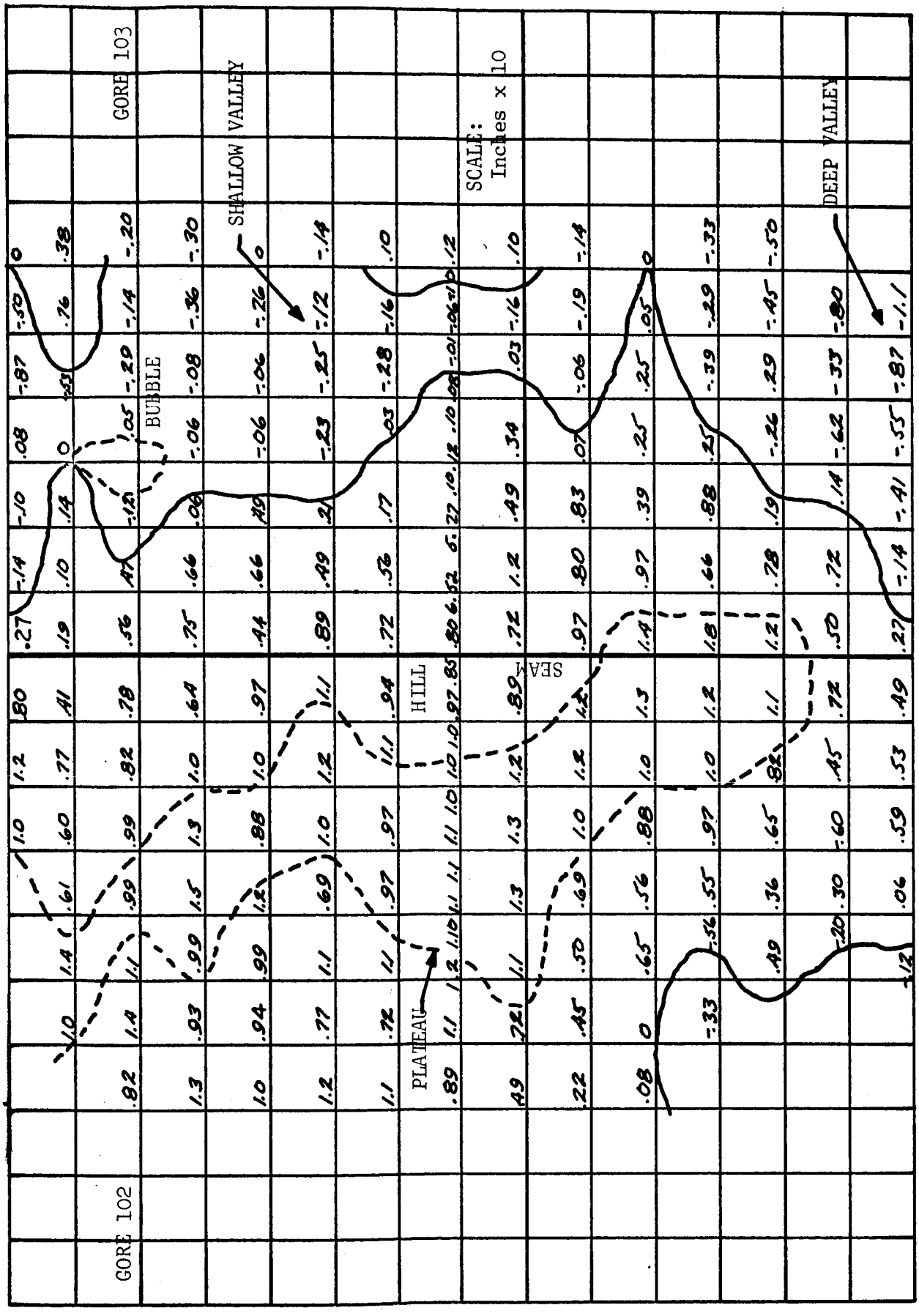

Figure F-4 Contour Map of Gores 103 and 102 at 7400 PSI

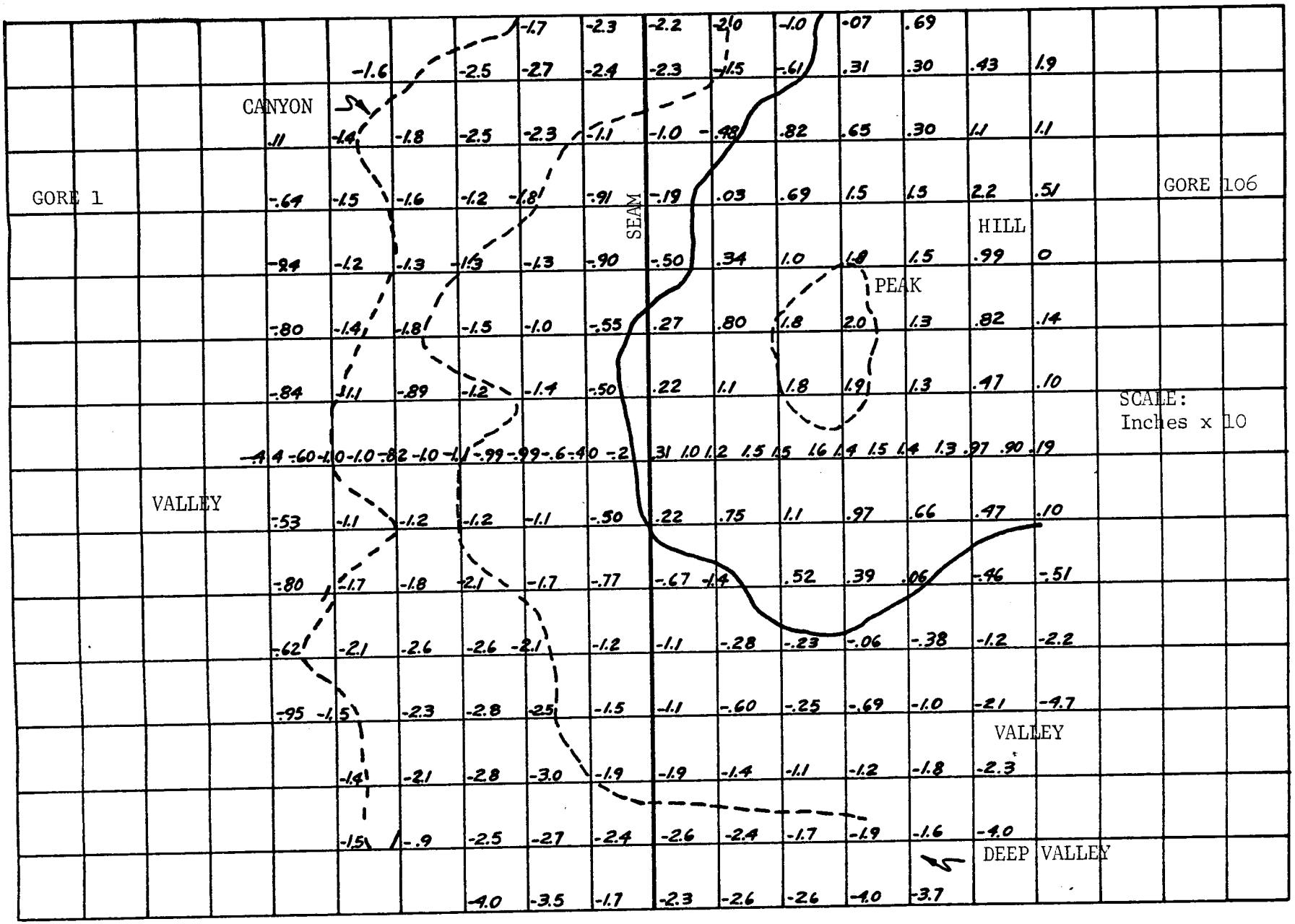

Figure F-5 Contour Map of Gores 106 and 1 at 7400 PSI

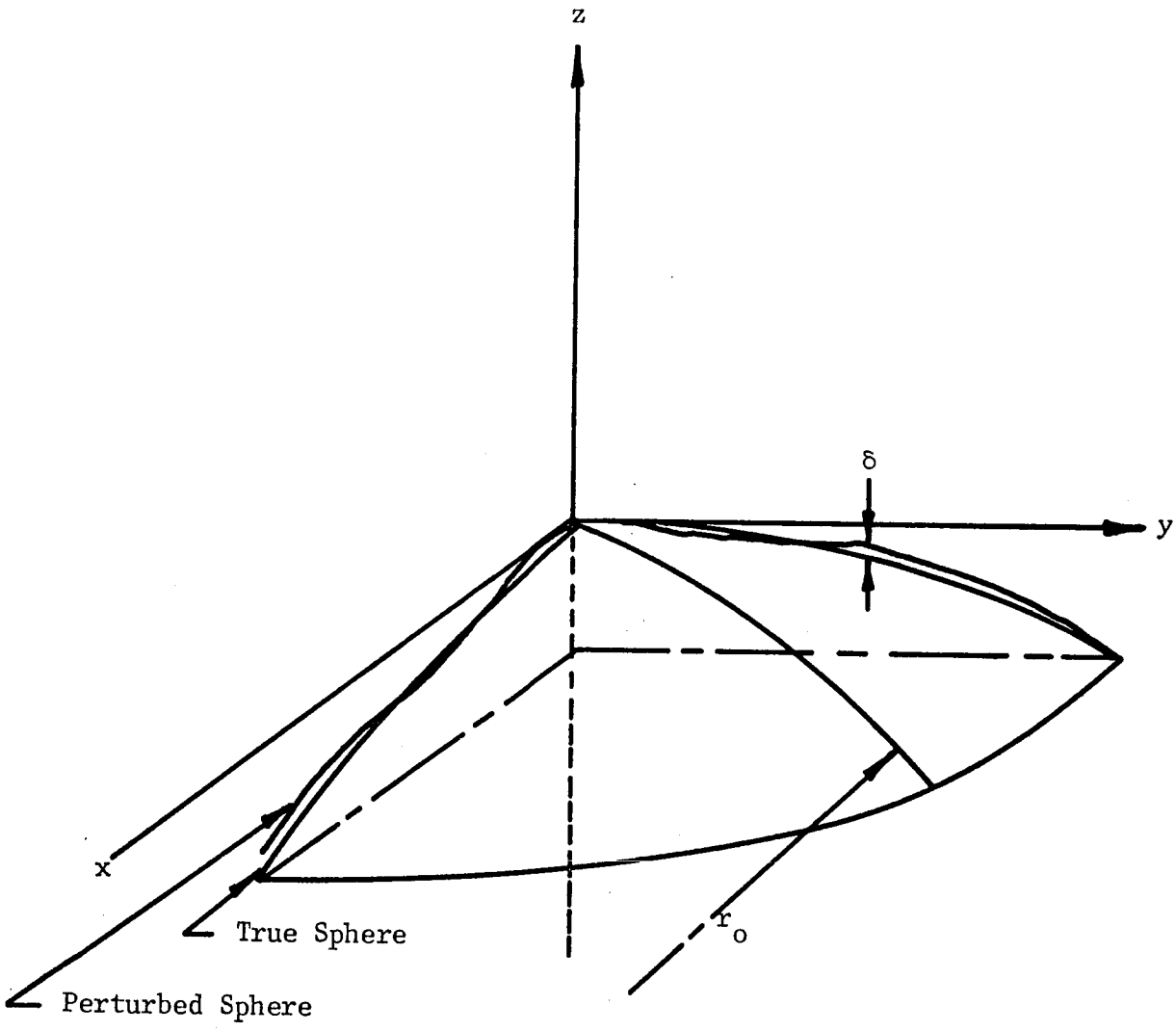

Figure F-6 Section of True Sphere vs. Perturbed Sphere. True Sphere Radius = r_o. $\delta(x, y)$ = Deviation in z Direction Between True and Perturbed Spheres.

is the projection of gores 1 and 106 also at 4800 psi. This figure shows a hill rising to a peak of 0.2" covering most of gore 106. The hill drops gradually to a valley on all sides extending over into gore 1 where it drops into a deep valley at the bottom of about 0.6". Figure F-4 is again gores 102 and 103 only now the pressure has been increased to 7400 psi. The similarity between Figure F-4 and F-2 is a lot more pronounced now. Gore 103 is again divided into a hill on the left dropping down into a valley on the right. The hill continues again over into gore 102 where the plateau forms in approximately the same location at a height of about 0.12" which is slightly less than the 4800 psi case. It is also noted that the peak in 4800 psi case blends into the plateau shown in Figure F-4. Figure F-5 shows gores 1 and 106 again which are the reinforced gores. There is close resemblence between this figure and Figure F-3 which was the 4800 psi case. It is noted that as before the hill is located on the upper half of gore 106 and peaks to about 0.2" again in almost the same place. The deep valley is at the bottom of both gores and is about the same value from the true sphere. Figure F-5 has a rather well defined canyon located on gore 1 but, in general, it is about the same displacement as seen on gore 1 in Figure F-3.

In conclusion, it has been shown that the undulations of the perturbed sphere are rather random in nature and are dependent upon whether the gores are reinforced and at what pressure the balloon is at. The deviations average about 0.2" from the true sphere and range to as much as $\pm$ 0.6". These deviations at the frequencies for which the cross section has been computed are instrumental in contributing to the oscillation noted in the experimental results.

A method for evaluating the quantitative oscillatory effect of the bumps shown in Figure F-1 through F-5 is to consider a physical optics method in order to approximate the radar cross section. If we consider first, the return one would expect by illuminating a "hill" say, the cross section can be obtained in the following manner.

Figure F-7 is the projection of the perturbed balloon shown in the z, ρ plane where $\rho = \sqrt{x^2 + y^2}$. For a first approximation we assume the perturbation to be a spheriod whose semi-major axis in the z,ρ plane is b and a respectively. However, in computing the cross section, we will further assume that the perturbation is smoothly joined to the sphere such that the first derivatives are matched and the contribution of the matching surfaces caused by a second derivative discontinuity is of the same order as the discontinuity caused by the spheroid joined to the sphere directly.

The physical optics cross section is given by,

$$\sigma = \frac{4\pi}{\lambda^2} \left| \int_{s'} e^{2ikz} \frac{\partial A}{\partial z} \, dz \right|^2 \qquad \text{(F.1)}$$

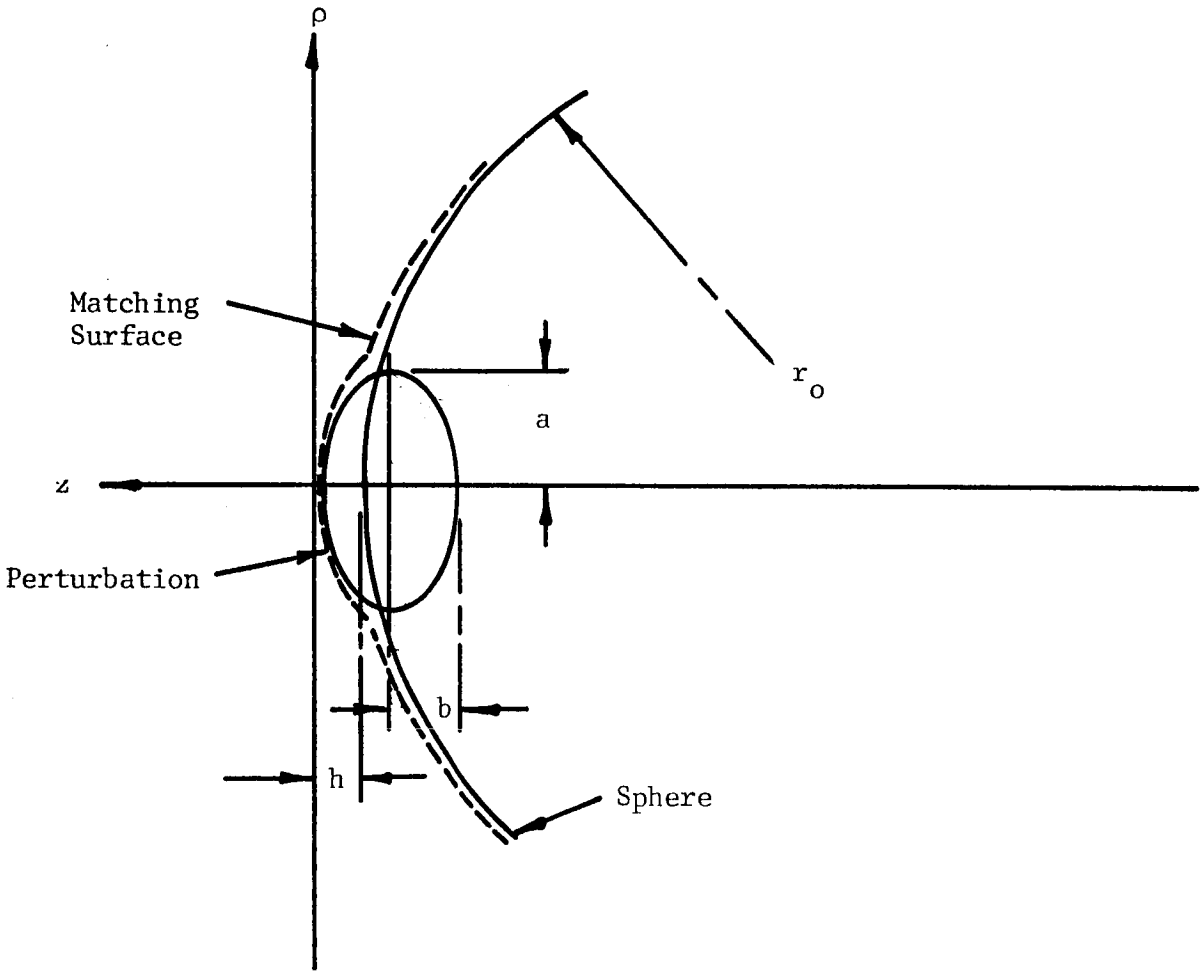

Figure F-7 Matching a Smooth Surface to a Perturbed Sphere. Matching is Done so that First and Second Derivative Discontinuities are the Same as Perturbed Sphere

where A is the area projected on the ρ plane at a distance z down the z axis. s' is the lit region which is just the hemisphere bounded by $-r_o - h \leq z \leq -h$. In the actual integration, the contribution from the shadow boundary, $z = -r_o - h$, is neglected since theory has shown this contribution to be spurious. If we define,

$$I = \left| \int_{s'} e^{2ikz} \frac{\partial A}{\partial z} dz \right|^2 \tag{F.2}$$

then integrating by parts yields,

$$I = \frac{e^{2ikz}}{2ik} \left(\frac{\partial A}{\partial z} - \frac{1}{2ik} \frac{\partial^2 A}{\partial z^2} \right) + o\left(\frac{1}{k^3}\right) \tag{F.3}$$

where I is evaluated over the region s'. The projected area is given by

$$A = \pi\rho^2 = \begin{cases} \pi a^2 \left[1 - \dfrac{(z+b)^2}{b^2}\right], & -b \leq z \leq 0 \\ \pi\left[r_o^2 - (z + r_o + h)^2\right], & -h - r_o \leq z \leq -b \end{cases} \tag{F.4}$$

Solving Equation F.4, $\frac{\partial A}{\partial z}$ and $\frac{\partial^2 A}{\partial z^2}$ and recalling that we will assume no first derivative discontinuity at the join, the integral is then given by

$$I = \frac{\pi}{2ik} \left\{ -\frac{2a^2}{b} + \frac{a^2}{ikb^2} - \frac{e^{-2ikb}}{ik} \right\} \tag{F.5}$$

Substituting Equation F.5 into Equation F.1 for the cross section

$$\sigma = \frac{\pi a^4}{b^4} \frac{\lambda a^2}{2b} \sin 2kb + \frac{\lambda^2}{16\pi} \left(\frac{a^4}{b^4} + 1 - \frac{2a^2}{b^2} \cos 2kb \right) \tag{F.6}$$

where $b \simeq \frac{a^2}{2r_o} + h$, $r_o \gg a$.

For the case of a valley, we will assume that the situation is basically the same only now the spheroid could lie within the true sphere as shown in Figure F-8. If the same analysis is applied, we find that the cross section one would obtain by considering incidence on the valley is given by

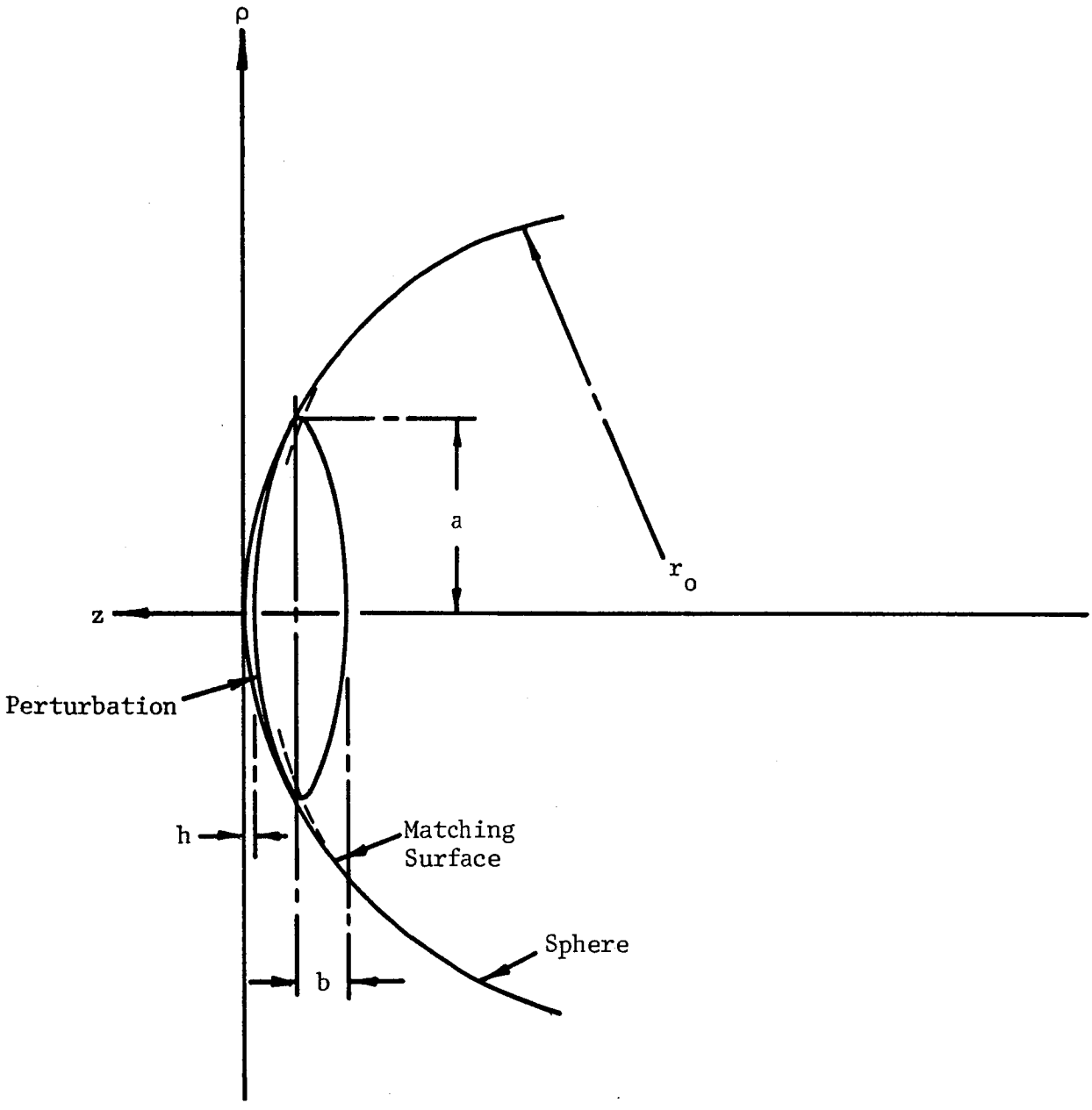

Figure F-8 Matching a Spheroid to Perturbed Sphere. Sphere Radius = r_o. Dotted Line Labeled Matching Surface Represents a Spheroid Giving Best Fit to Perturbed Sphere in Valley Region

$$\sigma = \frac{\pi a^4}{b^4}(b+h)^2 - \frac{\lambda a^2}{2b^2}(b+h)\sin 2k(b+h) + \frac{\lambda^2}{16\pi}$$

$$\left\{\frac{a^4}{b^4} + 1 - \frac{2a^2}{b^2}\cos 2k(b+h)\right\} \qquad (F.7)$$

where $b \leq \frac{a^2}{2r_o} - h$, $r_o \gg a$.

In order to consider the applications of Equations (F.6) and (F.7) to the problem one must determine the values of a and h from Figure F-1 - F-5. Since, in general, the figures show a partial hill and a partial valley, we could compute the cross section incident to each if there were more data available and obtain an average scintillation signature over the region. However, since not enough information is here at this time to obtain the desired input for Equations (F.6) and (F.7), the above analysis will have to remain as an academic approach until such time the information becomes available.

Another approach utilizing the method of physical optics is as follows. If we go back to Equation (F.3) for the integral, namely,

$$I = \frac{e^{2ikz}}{2ik}\left(\frac{\partial A}{\partial z} - \frac{1}{2ik}\frac{\partial^2 A}{\partial z^2} + o\left(\frac{1}{k^3}\right)\right), \qquad (F.8)$$

and assume we have a continuous surface out to the shadow boundary, then, integrating from z = 0 to the shadow boundary and excluding the boundary contribution gives,

$$I = \frac{1}{2ik}\left\{A'(0) - \frac{1}{2ik}A''(0)\right\} + o\left(\frac{1}{k^3}\right) \qquad (F.9)$$

Then to $o\left(\frac{1}{k^4}\right)$ in the cross section, we obtain

$$\sigma = \frac{[A'(0)]^2}{4\pi} \qquad (F.10)$$

If we had a true sphere then the change in the projected area on the plane of incidence evaluated at z = 0 is simply $2\pi r_o$, which gives us of course, $\sigma = \pi r_o^2$ as expected. In order to apply Equation (F.9) to the information available, all one need to do is pick up the center point on Figures F-1 and F-5 and compute A'(0) in the following manner and observe the precaution indicated.

Figures F-9 and F-10 show the geometry of the situation, where Figure (F-9) is the projection in the z, plane (i.e., x, y plane). From Figure (F-9) we see that for the contour of constant z shown in Figure (F-10) the area is given by

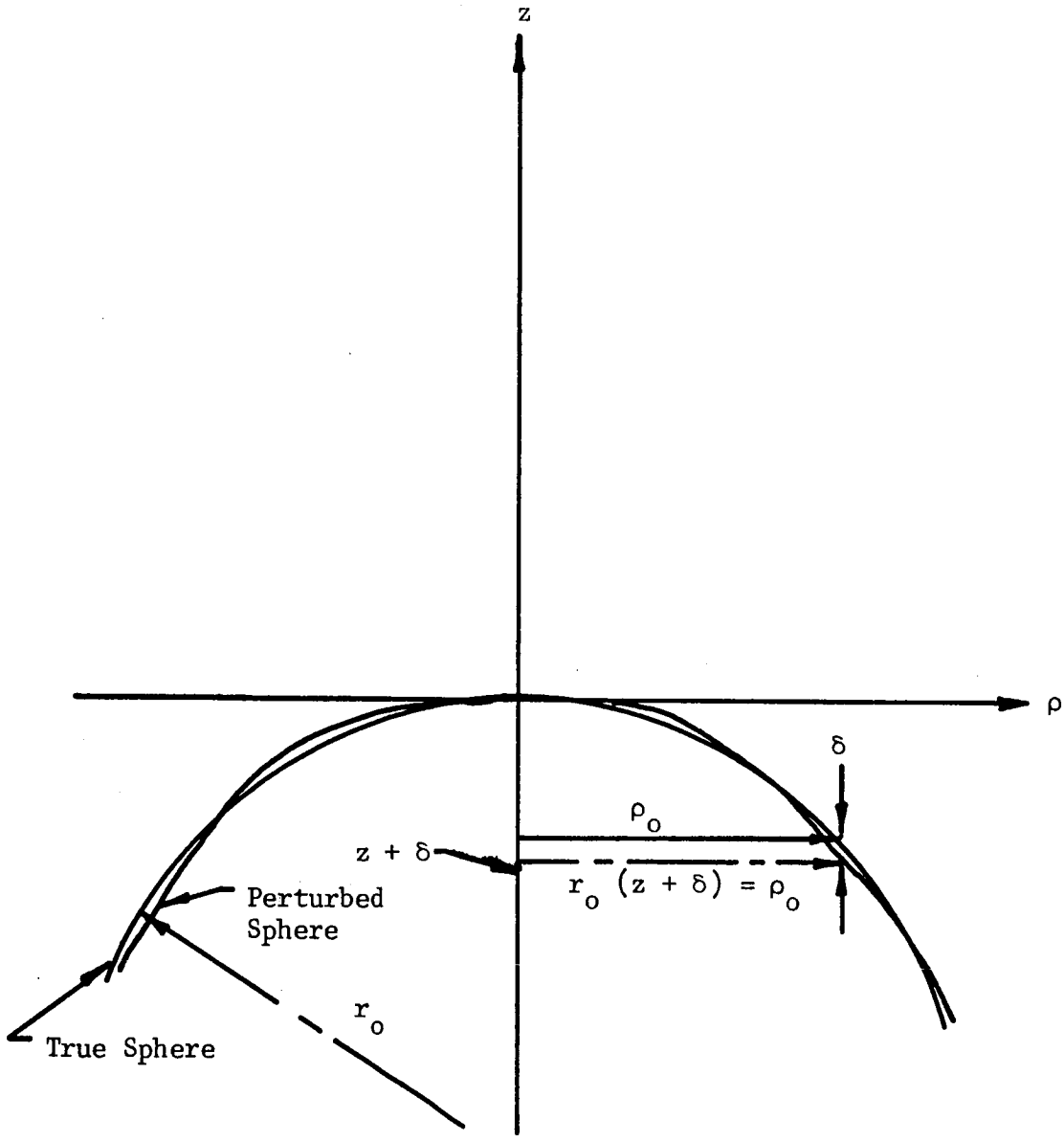

Figure F-9 Cut of Perturbed Sphere Relative to True Sphere

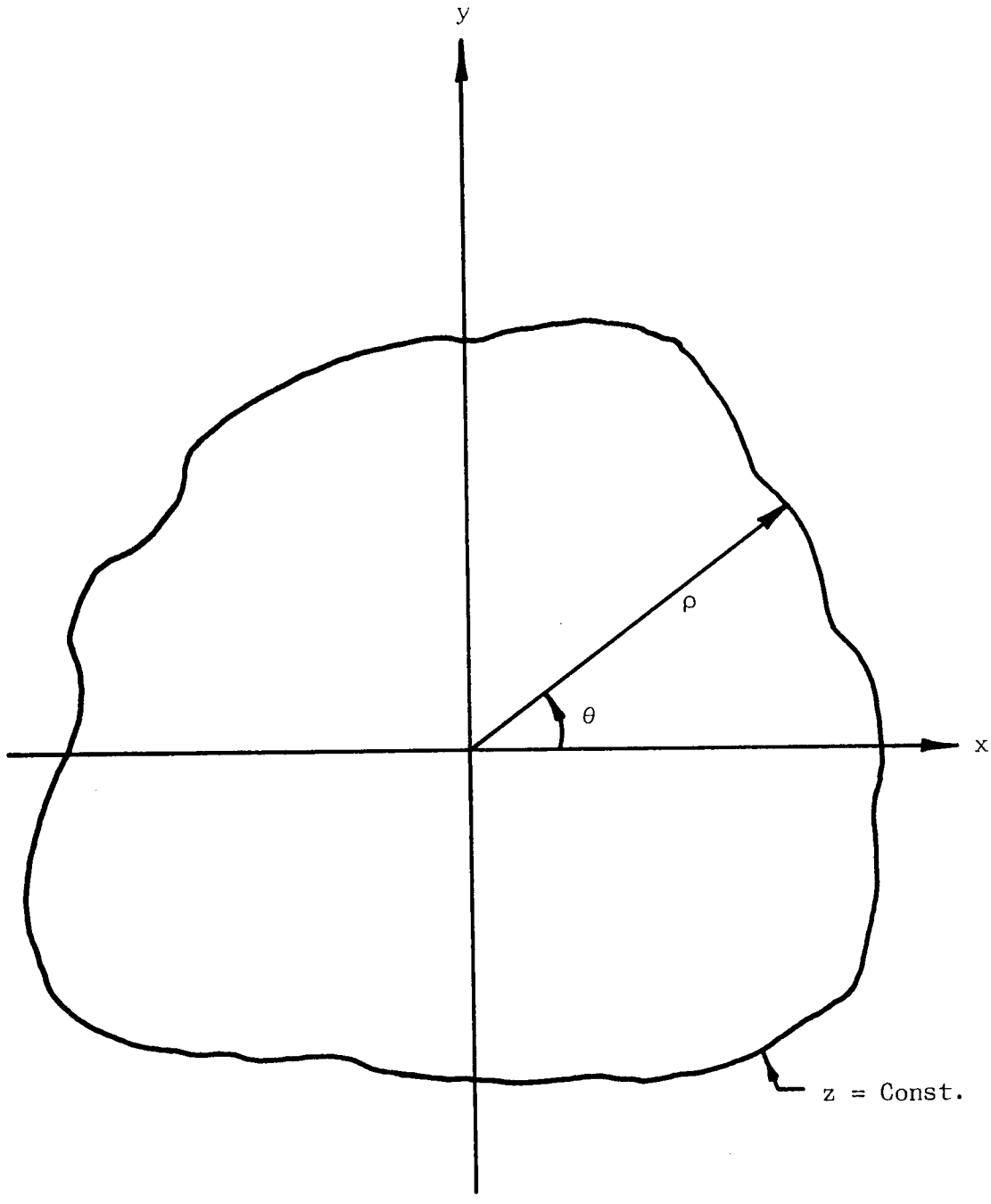

Figure F-10 Projected Area for Physical Optics Evaluation

$$A(z) = \frac{1}{2} \rho^2 \, d\theta, \tag{F.11}$$

where

$$\rho^2 \simeq 2 r_o \delta - 2 r_o z, \qquad r_o \gg \delta, z. \tag{F.12}$$

Substitution of (F.11) into Equation (F.10) gives,

$$A(z) = -2\pi r_o \left[z - \frac{1}{2\pi} \int_0^{2\pi} \delta \, d\theta \right] \tag{F.13}$$

hence

$$A'(0) = -2\pi r_o \left[1 - \frac{1}{2\pi} \int_0^{2\pi} \frac{\partial \delta}{\partial z}(0) \, d\theta \right] \tag{F.14}$$

$$= -2\pi r_o \left(1 - \overline{\frac{\partial \delta}{\partial z}(0)} \right)$$

where $\overline{\frac{\partial \delta(0)}{\partial z}}$ implies the average value of $\frac{\partial \delta(0)}{\partial z}$ in the region $0 \leq \theta \leq 2\pi$. Now, consider

$$\frac{\partial \delta}{\partial z} = \frac{\partial \delta}{\partial \rho} \frac{\partial \rho}{\partial z} \tag{F.15}$$

From Equation (F.11)

$$\frac{\partial \rho}{\partial z} = \frac{1}{\frac{\partial}{\partial \rho} - \frac{\rho}{r_o}} \tag{F.16}$$

hence

$$\frac{\partial \delta}{\partial z} = \frac{\frac{\partial \delta}{\partial \rho}}{\frac{\partial \delta}{\partial \rho} - \frac{\rho}{r_o}} \tag{F.17}$$

Substitution into (F.13) for A'(0) gives,

$$A'(0) = -2\pi r_o \left[\frac{-\frac{\rho}{r_o}}{\frac{\partial \delta}{\partial \rho} - \frac{\rho}{r_o}} \right] \tag{F.18}$$

$$= -2\pi r_o \left(\frac{1}{1 - \frac{r_o}{\rho} \frac{\partial \delta}{\partial \rho}} \right)$$

subject to the restriction

$$\rho > \left| r_o \overline{\frac{\partial \delta}{\partial \rho}} \right| \tag{F.19}$$

within and on the boundary ρ = const. Then the cross section is simply,

$$\sigma = \pi r_o^2 \left| \frac{1}{1 - \left(\frac{r_o}{\rho}\right)\left(\overline{\frac{\partial \delta}{\rho}}\right)} \right|^2 \tag{F.20}$$

To implement Equation (F.20) we draw a circle of radius ρ, subject to condition (F.19) at the center of the figures for which one wishes to obtain the cross section. Then compute,

$$\frac{\partial \delta}{\partial \rho} = \frac{\Delta \delta}{\rho} = (\delta_\rho - \delta_{center})/\rho \tag{F.21}$$

at a number of points on the circumference. From these values find the average value,

$$\overline{\frac{\partial \delta}{\partial \rho}}$$

and substitute it into Equation (F.20) for the cross sections. The validity of this procedure of course depends upon condition (F.19). If we examine the physics a little closer, we have by Equation (F.10).

$$A'(z) = \int_0^{2\pi} \rho \frac{\partial \rho}{\partial z} \, d\theta \tag{F.22}$$

which when substituted back into (F.9) gives,

$$\sigma = \pi \left| \frac{1}{2\pi} \int_0^{2\pi} \frac{\rho \, d\theta}{\frac{\partial z}{\partial \rho}} \right|^2 \tag{F.23}$$

Since z is the equation of the surface the points on the surface for which

$$\frac{\partial z}{\partial \rho} = 0$$

are just the specular reflection points. Hence, if ρ is chosen such that the circle encloses a specular point, the results will not be valid.

If the perturbed surface follows the true sphere contour rather closely then the specular point will be around $\rho = 0$ as can be seen from (F.9). Therefore, in determining ρ one must find the specular point and choose this point as $\rho = 0$. It can be shown that

$$\lim_{\substack{\rho \to 0 \\ z' \to 0}} \frac{\rho}{\frac{\partial z}{\partial \rho}} = -r_o \qquad \text{(F.24)}$$

Therefore, no singularity exists within the boundary, and the cross section will only be valid out to the next specular point. If no other specular points appear in the region, the cross section should be quite accurate.

In conclusion, it is pointed out that Equation (F.20) will be valid if the perturbed sphere has a horizontal slope at $x = y = 0$. If, however, this is not the case, then all one need do is locate the specular point which should be near the center and measure

$$\frac{\partial \delta}{\partial \rho}$$

centered around this point. This transformation does not present any change in the predicted cross section since the portion over which we are measuring is comparatively flat. If, on the other hand, more than one specular point lies close to the origin the prediction will not be valid.

APPENDIX G

G.1 RADAR CROSS SECTION OF ECHO II

The radar cross section of Echo II can be determined by physical optics method. Here, the backscattered magnetic field can be determined by

$$\bar{H}_s = \frac{jkH_o}{2\pi R_o} e^{-u2kR_o} \int_{s_1} (\hat{k}_o \cdot \hat{n})\, \hat{a}\, e^{-j2\hat{k}_o \cdot \bar{r}}\, ds \qquad (G.1)$$

where

$\hat{a}$ is the unit polarization vector of the incident magnetic field
$\hat{k}_o$ is the unit propagation vector of the incident magnetic field
$\hat{n}^o$ is the unit outward normal vector to the surface of the object
$\bar{r}$ is the position vector of the surface of the object
H_o is the magnitude of the incident magnetic field
R_o^o is the distance from the point of observation to the scatterer reference point
s_1 is the illuminated surface of the scatterer.

With the propagation vector given by

$$\hat{k}_o = \hat{x} \sin\theta_1 \cos\phi_1 + \hat{y} \sin\theta_1 \sin\phi_1 + \hat{z} \cos\theta_1 \qquad (G.2)$$

and the position vector given by

$$\bar{r} = r\,(\hat{x} \sin\theta \cos\phi + \hat{y} \sin\theta \sin\phi + \hat{z} \cos\theta) \qquad (G.3)$$

$$r = (x^2 + y^2 + z^2)^{1/2} \qquad (G.4)$$

and the position vector given by

$$\bar{r} = r\,(\hat{x} \sin\theta \cos\phi + \hat{y} \sin\theta \sin\phi + \hat{z} \cos\theta)$$
$$r = (x^2 + y^2 + z^2)^{1/2} \qquad (G.5)$$

then

$$\hat{k}_o \cdot r = r\,[\sin\theta_1 \sin\theta \cos(\phi - \phi_1) + \cos\theta \cos\theta_1] \qquad (G.6)$$

For the Echo II scatterer, the object is a sphere with small perturbations on the surface, and therefore, the unit outward normal vector can be represented by

$$\hat{n} = \frac{r}{|r|} = \hat{r} \qquad (G.7)$$

and thus giving

$$\hat{k}_o \cdot \hat{n} = \sin\theta_1 \sin\theta \cos(\phi - \phi_1) + \cos\theta \cos\theta_1 \qquad (G.8)$$

Let $\beta(\theta, \phi) = \sin\theta_1 \sin\theta \cos(\phi - \phi_1) + \cos\theta \cos\theta_1$, then the scattered magnetic field is

$$\overline{H}_s = \frac{jkH_o}{2\pi R_o} e^{-j2kR_o} \int \hat{a}\, r^2\, \beta(\theta, \phi) \sin\theta\, e^{-u2k\beta(\theta,\phi)r}\, d\theta\, d\phi \qquad (G.9)$$

since $ds = r^2 \sin\theta\, d\theta\, d\phi$. For the scatterer under consideration, Echo II, the surface of this scatterer is assumed to be a perturbed spherical surface with small perturbations less than a wavelength. The distance r from the center of the scatterer to a point on the surface can be represented by

$$r = r_o + \delta(r_o) \qquad (G.10)$$

where r_o is the radius of the sphere and $\delta(r_o)$ is the deviation of the scatterer from a spherical body. Since the deviations are small, only the phase variations need to be considered so that the scattered magnetic field can be approximated by

$$\overline{H}_s = \frac{jkH_o}{2\pi R_o} e^{-j2kR_o} r_o^2 \int_{S_1} \hat{a}\, \beta(\theta, \phi) \sin\theta\, e^{-j2k\beta(\theta,\phi)r_o} \qquad (G.11)$$

$$[1 - 2jk\beta(\theta,\phi)\,\delta(r_o) - 2k^2\beta^2(\theta,\phi)\,\delta^2(r_o)]\, d\theta\, d\phi \qquad (G.12)$$

The first term of the above integral is the sphere scattered field. The second and third integrals pertain to the scattered field resulting from the surface not being spherical.

The Echo II balloon was intended to be a spherical body, but due to the construction, the joining of spherical segments at a seam, the surface budges and flattens. The amount of budging and flattening is dependent upon inflation pressure. Plots of constant contours of depression from the spherical tip for various inflation pressures were made available so that from these data, the deviation from the spherical body can be determined. These deviations can best be represented in rectangular coordinates so that by the use of the rectangular-spherical coordinate transformations,

$$\begin{aligned} x &= r_o \sin\theta \cos\phi \\ y &= r_o \sin\theta \cos\phi \\ z &= r_o \cos\theta \end{aligned} \qquad (G.13)$$

so that

$$d\theta = \frac{dx \cos \phi + dy \sin \phi}{r_o \cos \theta} \tag{G.14}$$

$$d\phi = \frac{dy \cos \phi - dx \sin \phi}{r_o \sin \theta_o} \tag{G.15}$$

$$\cos \phi = x/(x^2 + y^2)^{1/2} \qquad \sin \phi = y/(x^2 + y^2)^{1/2}$$

$$\sin \theta = (x^2 + y^2)^{1/2}/r_o \qquad \cos \theta = \left(1 - \frac{x^2 + y^2}{r_o^2}\right)^{1/2} \tag{G.16}$$

Also, $\delta(r_o) \approx \delta_z \cos \theta$ so that the scattered field becomes

$$\bar{H}_s = \frac{jkH_o}{2\pi R_o} e^{-j2kR_o} \left\{ r_o^2 \int_{s_1} \hat{a}\, \beta(\theta,\phi) \sin \theta\, e^{-j2k\beta(\theta,\phi)r_o}\, d\theta\, d\phi \right. \tag{G.17}$$

$$- \frac{2}{r_o} \int_{s_1} \hat{a}\, \frac{\beta(x,y)}{x^2+y^2} \left[(x^2 - y^2)\, dx\, dy + xy\, (dy^2 - dx^2)\right] \tag{G.18}$$

$$\left. \left[jk \frac{\beta(x,y)}{r_o} \delta_z + k^2 \frac{\beta^2(x,y)}{r_o^2} \delta_z^2 \cos \theta \right] e^{-j2k\beta(x,y)} \right\} \tag{G.19}$$

where

$$\beta(x,y) = (x \cos \phi_1 + y \sin \phi_1) \sin \theta_1 + r_o \cos \theta \cos \theta_1 \tag{G.20}$$

$$\cos \theta = \left(1 - \frac{x^2 + y^2}{r_o^2}\right)^{1/2} \tag{G.21}$$

Since the task of defining the perturbed function δ_z over all points become formidable, discrete points will be considered so that the integral involving the perturbation function can be written as a sum. With

$$dx = dy = \Delta x = b,$$

and

$$x = n\, \Delta x = bn \tag{G.22}$$

$$y = m\, \Delta x = bm,$$

the scattered field is

$$\bar{H}_s = \frac{jk\bar{H}_o}{2\pi R_o} e^{-j2kR_o} \left\{ r_o^2 \int \hat{a} \sin\theta \, e^{-j2\beta(\theta,\phi)r_o} \beta(\theta,\phi) \, d\theta \, d\phi \right. \quad (G.23)$$

$$- \frac{2b^2}{r_o} \sum_n \sum_m \hat{a} \, \beta(n,m) \left(\frac{n^2 - m^2}{n^2 + m^2} \right) e^{-j2k\beta(n,m)} \quad (G.24)$$

$$\left. \left[jk \frac{\beta(n,m)}{r_o} \delta_{znm} + k^2 \frac{\beta^2(n,m)}{r_o^2} \delta_{znm}^2 \cos\theta_{nm} \right] \right\} \quad (G.25)$$

where

$$\beta(n,m) = b(n\cos\phi_1 + m\sin\phi_1)\sin\theta_1 + r_o \cos\theta_{nm} \cos\theta_1 \quad (G.26)$$

$$\cos\theta_{nm} = \left[1 - b^2 \frac{n^2 + m^2}{r_o^2} \right]^{1/2} \quad (G.27)$$

For the problem at hand, θ_{nm} is small so that

$$\cos\theta_{nm} \approx 1 - \frac{b^2}{2r_o}(n^2 + m^2) \quad (G.28)$$

and by letting $\phi_1 = 0$

$$\beta(n,m) = bn\sin\theta_1 + r_o\cos\theta_1 - b^2 \frac{(n^2 + m^2)}{2r_o^2} \cos\theta_1 \quad (G.29)$$

The resultant scattered field is

$$\bar{E}_s(\theta_1) = \frac{jk\bar{H}_o}{2\pi R_o} e^{-j2kR_o} \left\{ r_o^2 \int_{s_1} \hat{a} \, \beta(\theta,\phi) \sin\theta \, e^{-j2k\beta(\theta,\phi)r_o} \, d\theta \, d\phi \right. \quad (G.30)$$

$$- \frac{2b^2}{r_o} e^{-j2kr_o\cos\theta_1} \sum_n \sum_m \hat{a} \, \alpha_n \left(\frac{n^2 - m^2}{n^2 + m^2} \right) e^{-j2k\gamma(n,m)} \quad (G.31)$$

$$\left. \left[j \frac{k\alpha_n}{r_o} \delta_{znm} + k^2 \frac{\alpha_n^2}{r_o^2} \delta_{znm}^2 \right] \right\} \quad (G.32)$$

where

$$\gamma(n,m) = bn\sin\theta_1 - \frac{b^2}{2r_o}(n^2 + m^2)\cos\theta_1 \quad (G.33)$$

$$\alpha_n = bn \sin\theta_1 + r_o \cos\theta_1 \qquad (G.33)$$

δ_{znm} is the deviation at point (n,m) from the sphere

The above representation contains within it two approximations. The first is caused by replacing the exponential in Equation G.9 by the first three terms in its power series expansion as given by the factor G.12. In order to justify this approximation, an estimate of the magnitude of $\delta(r_o)$ must be found and using this estimate the error induced by omitting the remainder of the power series must be computed. The magnitude $\delta(r_o)$ was obtained by examining the actual data in the photogrammetric measurements. The second approximation is obtained by replacing the integral by the summation. The accuracy of this approximation is, of course, dependent upon the magnitude of the grid size, b. The computations of the series were performed using successively smaller grid sizes until the difference in computations, taking account of the possible error induced by the first approximation, gave cross section values which differed by less than .75 db. The possible round off error inherent in the computer program was shown to give cross section error of less than .25 db. On this basis it is asserted that the total cross section error of the computation is less than 1 db.

The integral for the scattered field from the sphere, namely

$$\bar{H}_{sphere} = \frac{-H_o}{2R_o}\ \hat{a}\ r_o\ e^{-j2(R_o - r_o)} \qquad (G.34)$$

For the orientation chosen in this problem, θ_1 varies between $\pi/2$ and $3\pi/2$ so that by letting $\theta_1 = \theta_o - \pi$ for computation simplication, the scattered field about a normal aspect θ_o varying between $-\pi/2$ and $\pi/2$ becomes

$$\bar{H}_s(\theta_o) = \frac{H_o r_o}{2R_o} e^{-j2k(R_o - r_o)}\ \hat{a}\left\{1 + \frac{2kb^2}{\pi r_o} e^{-jkr_o(1-\cos\theta_o)}\ [\omega_1(\theta_o) - j\omega_2(\theta_o)]\right\} \qquad (G.35)$$

where

$$W_1(\theta_o) = \sum_n \sum_m \frac{k\alpha_n^2}{r_o^2}\left(\frac{n^2 - m^2}{n^2 + m^2}\right) e^{-j2k\gamma(n,m)}\ \delta_{znm} \qquad (G.36)$$

$$W_2(\theta_o) = \sum_n \sum_m \frac{k^2\alpha_n^3}{r_o^3}\left(\frac{n^2 - m^2}{n^2 - m^2}\right) e^{-j2k\gamma(n,m)}\ \delta_{znm} \qquad (G.37)$$

$$\alpha_n = bn \sin\theta_o - r_o \cos\theta_o \qquad (G.38)$$

$$\gamma(n,m) = bn \sin\theta_o + \frac{b^2}{2r_o}(n^2 + m^2)\cos\theta_o \qquad (G.39)$$

With b = 6 inches, r_o = 810 inches, k = 2π (0.084f) f in kmc,

$$\bar{H}_s(\theta_o) = \frac{H_o r_o}{2R_o} e^{-j2k(R_o - r_o)} \hat{a} \left\{ 1 + 0.0151f\, e^{-j2kr_o(1-\cos\theta_o)} \right.$$

$$\left. [\omega_1(\theta_o) - j\,\omega_2(\theta_o)] \right\} \qquad (G.40)$$

From the inflation test data, values of depression were referenced to a planar surface so that for the scattered field equation,

$$\delta_{znm} = \delta_{Rnm} - \frac{b^2}{2r_o}(n^2 + m^2) \qquad (G.41)$$

where δ_{Rnm} is the read value and the second term is the correction for the spherical deviations. In Table G-1, the average deviation, the average of the square of the deviation, and the range of the deviation for each gore at the various pressures are listed.

The cross section of an object is given by

$$\sigma = 4\,\pi\, R_o^2 \frac{|H_s|^2}{|H_i|^2} \qquad (G.42)$$

where H_s is the scattered magnetic field and H_i is the incident magnetic field. For the problem at hand, the cross section is

$$\sigma(\theta_o) = \pi\, r_o^2 \left| 1 + 0.0151f\, e^{-jkr_o(1-\cos\theta_o)} [\omega_1(\theta_o) - j\omega_2(\theta_o)] \right|^2 \qquad (G.43)$$

where when $\omega_1(\theta_o) = \omega_2(\theta_o) = 0$ the remaining cross section is that of the sphere, πr_o^2. The average cross section over all aspect angles is found by

$$\sigma_{avg} = \pi r_o^2 \left| 1 + \frac{0.0151f}{\beta_2 - \beta_1} \int_{\beta_1}^{\beta_2} e^{-j2kr_o(1-\cos\theta_o)} \right. \qquad (G.44)$$

$$\left. [\omega_1(\theta_o) - \omega_2(\theta_o)]\, d\theta_o \right|^2 \qquad (G.45)$$

where β_1 and β_2 define the interval of integration.

TABLE G-1

Gore Number	Pressure lb/in^2	Range of Deviation (inches)	Average Deviation (inches)	Standard Deviation ± (inches)
102	2800	-0.233 to 0.231	-0.029	0.112
	4800	-0.078 to 0.589	0.119	0.148
	7400	-0.045 to 0.149	0.078	0.088
103	2800	-0.368 to 0.231	-0.070	0.151
	4800	-0.384 to 0.200	-0.018	0.137
	7400	-0.098 to 0.168	-0.014	0.052
106	4800	-0.660 to 0.005	-0.239	0.291
	7400	-0.517 to 0.031	-0.163	0.198
1	4800	-0.515 to 0.195	-0.045	0.169
	7400	-0.647 to 0.221	-0.072	0.219

If it is assumed that the cross section results from only the two gores indicated in each inflation data plots, that is only the two gores shown are perturbed significantly to effect the cross section, then the resulting cross section relative to the sphere for 5.85 KMC are shown in Figures G-1 and G-2 for the angle range of -8.5 to +8.5 degrees as a function of pressure. If it is assumed that the balloon was made of samples of the gores as shown in the static inflation plots along the spherical surface, then the relative cross section for the various pressures are listed in Table G-2 for a 5.85 KMC frequency.

TABLE G-2

Pressure	Gores	Relative Cross Section (db)
2800	102 and 103	2.35
4800	102 and 103	-1.24
	106 and 1	3.00
7400	102 and 103	-0.76
	106 and 1	2.22

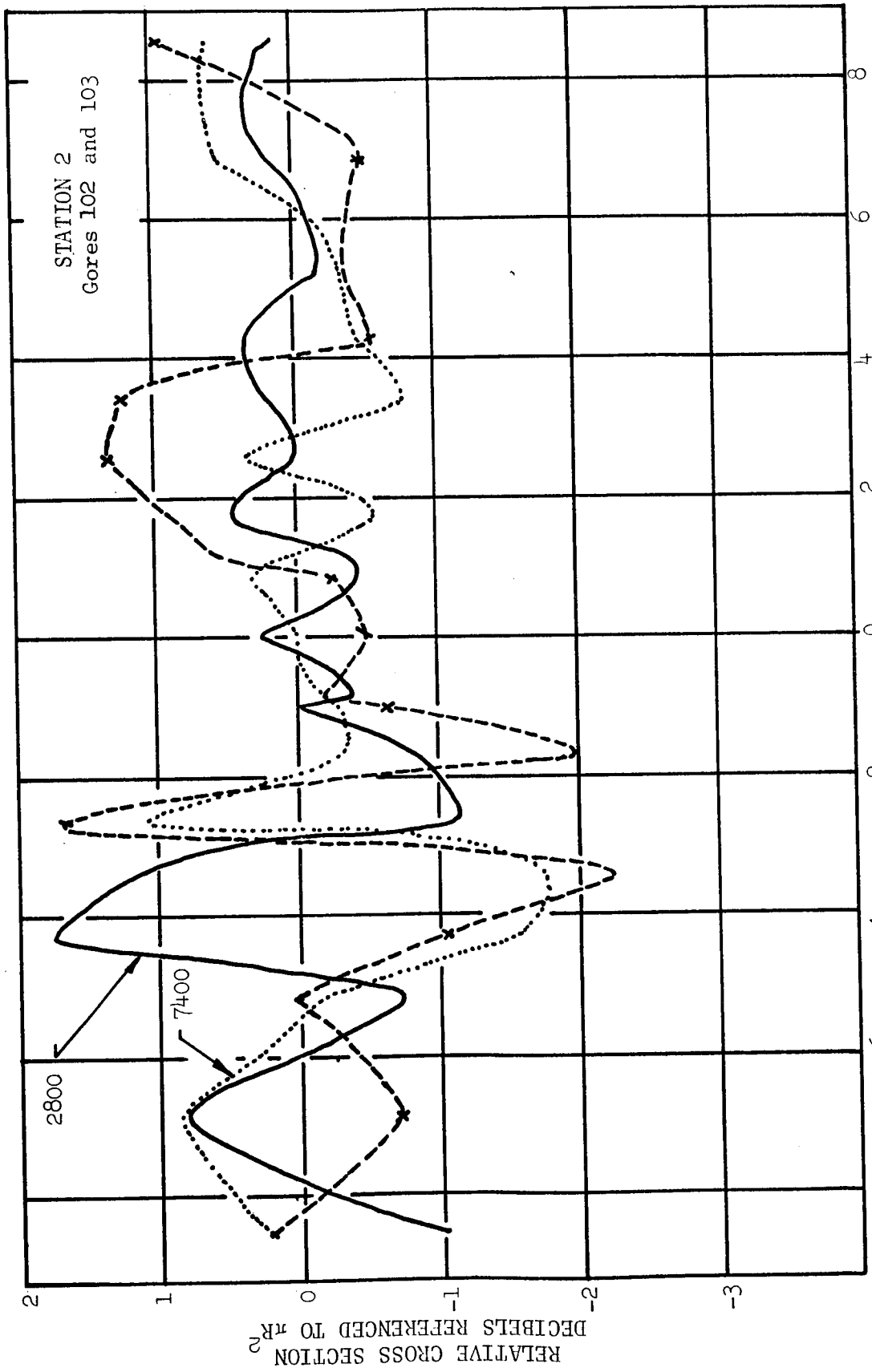

Figure G-1 Cross Section Echo II, Gores 102 and 103
Frequency 5.85 KMCS

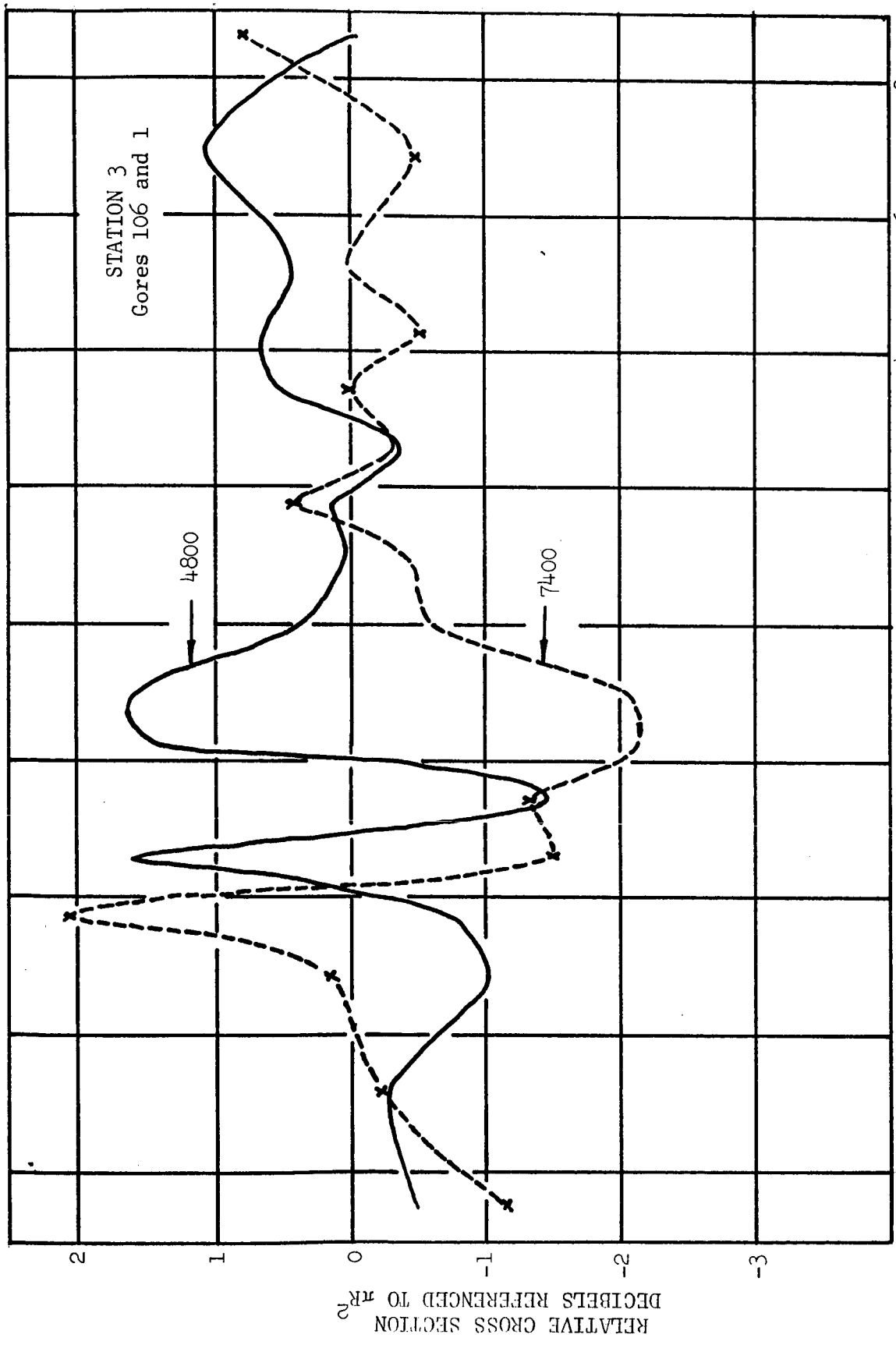

Figure G-2 Cross Section Echo II, Gores 106 and 1
Frequency 5.85 KMCS

or

$$\pi a^2 = \sigma^{(m)} + 4.5 \text{ db.}$$

Thus, the near-field measured cross section must be increased by 4.5 db to obtain the true cross section.

The antenna taper, previously mentioned in connection with background levels has an effect upon the data. At the maximum bistatic angle, that part of the balloon which is most significant for scattering, i.e., that part in the neighborhood of the bistatic angle bisector, is at the 9.5° point of the antenna pattern, with a consequent power loss. The resulting data correction is:

\+ 3 db, at L-Band, horizontal polarization
\+ 2.2 db, at L-Band, vertical polarization,
\+ 5 db, at C-Band, horizontal polarization, and
\+ 4 db, at C-Band, vertical polarization.

These corrections must be applied to the measured cross section at bistatic angles of 30°. For lesser bistatic angles, we have interpolated linearly.

D.4 THE STATIC INFLATION TESTS

During the period, 1 June - 10 August, 1963, three A-12 balloons were inflated. Balloon No. 9 was initially inflated to check out systems. Balloon No. 11 was then inflated to rupture, Balloon No. 9 was reinflated to rupture, and Balloon No. 13 was inflated to rupture. R.F. data was obtained for all three balloons. For balloons No. 9 and No. 11, measurements were made at 1.71 KMC, 5.65 KMC, and 5.85 KMC. The test procedure was to inflate the balloon to a given nominal surface stress, to maintain the stress while a complete R.F. test sequence was performed, to reduce the stress to approximately 500 psi, and to perform the test sequence again in this "relaxed" condition. This was then repeated at a higher pressure, until rupture. It was very quickly observed that the HV cross sections were, with few exceptional points, well down in the background.

To analyze the data, it was decided to divide the balloon into 5° intervals. After making the corrections to the data noted above, the average cross section on each 5° interval was measured using a planimeter, and the scintillation on the interval (i.e., the difference, in db, between the maximum and minimum cross section. There was not enough difference between the 5.65 KMC and 5.85 KMC data to warrant considering both, so 5.85 KMC was chosen. The results are shown in Tables D-1 and D-2. The columns headed 0, 5, 10, 15, 20, 25, are the 5° intervals starting from the right (reinforced gore)[1]. The entries under "m" are the mean values relative to the nominal balloon, and the entries under "Δ" are the scintillations.

Balloon No. 13 was designated to be the prime data balloon. In order to keep the balloon under stress for shorter periods of time, it was decided to omit the 5.65 KMC measurement and to perform cross polarization measurements only as spot checks. The results are listed in Table D-3.

[1] For Nos. 11 and 13 Balloons. For No. 9 Balloon, the reinforced gore was on the left.

TABLE D-1

MEAN VALUES AND SCINTILLATIONS OVER 5° INTERVALS

NO. 11 BALLOON

Pattern #	Psi		0		5		10		15		20		25	
			m	Δ*	m	Δ	m	Δ	m	Δ	m	Δ	m	Δ
46 - 63	750	L_V	0	10	-4	28	0	8	-1	7	0	6	0	4
		L_H	2	10	-3	30	1	8	0	4	1	3	1	3
		C_V	1	9	-1	23	-1	14	-2	7	1	9	0	4
		C_H	0	9	0	28	-1	19	-3	9	1	7	0	4
82 - 99	1500	L_V	1	8	-2	33	0	6	0	5	1	3	0	4
		L_H	1	12	-1	28	1	8	1	6	2	4	1	4
		C_V	0	9	-2	21	0	13	-4	4	-1	8	-1	5
		C_H	0	10	-1	21	-1	15	-3	6	-1	9	-1	4
126 - 143	2780	L_V	1	8	-1	26	1	6	0	6	2	3	1	3
		L_H	1	7	0	27	2	8	1	5	2	3	2	3
		C_V	1	8	0	18	1	9	-2	3	0	4	-1	3
		C_H	0	9	-1	18	0	8	-1	5	1	5	0	4
162 - 179	4800	L_V	1	6	0	19	0	7	1	4	2	3	1	5
		L_H	2	9	0	17	2	4	3	3	4	4	2	3
		C_V	1	6	1	12	1	3	0	1	0	3	-1	3
		C_H	0	4	0	12	1	3	1	2	1	2	0	2
180 - 197	500	L_V	2	9	1	23	1	7	2	3	3	3	2	3
		L_H	3	8	1	22	1	5	2	4	4	3	2	3
		C_V	0	6	-1	16	0	7	-2	3	-1	5	-1	4
		C_H	0	7	-1	15	0	7	0	3	0	5	-1	3

TABLE D-2

MEAN VALUES AND SCINTILLATIONS OVER 5° INTERVALS

NO. 9 BALLOON

Pattern #	Psi		m	Δ	m	Δ	m	Δ	m	Δ	m	Δ	m	Δ
202 - 217	750	L_V	-1	4	-1	3	-1	6	-3	8	-5	17	-1	8
		L_H	1	3	1	5	1	5	0	6	-5	23	1	4
		C_V	-3	10	-2	6	-1	9	-4	12	-4	18	-3	19
		C_H	-2	9	-1	6	-1	12	-1	9	-5	17	-2	20

* Entries under "Δ" give the peak to peak scintillation in db. This is more convenient to work with, since the mean does not always fall half way between these extremes.

TABLE D-2 Cont.

Pattern #	Psi		m^0	Δ	m^5	Δ	m^{10}	Δ	m^{15}	Δ	m^{20}	Δ	m^{25}	Δ
230 - 241	1500	L_V	0	5	-1	3	0	4	-1	5	-3	20	0	5
		L_H	0	4	0	4	1	5	0	3	-4	12	1	5
		C_V	-2	10	-4	6	-4	12	-2	9	-5	13	-3	19
		C_H	-2	9	-1	5	0	12	-1	9	3	15	-2	20
260 - 269	2600	L_V	1	6	0	3	1	4	0	4	-2	12	1	4
		L_H	1	4	2	2	4	4	1	3	-2	13	2	4
		C_V	-1	9	0	5	1	9	-2	6	-5	16	-2	16
		C_H	-1	9	-1	5	0	10	0	6	-4	16	-1	15
280 - 289	4800	L_V	1	5	0	2	1	4	1	5	-4	11	1	4
		L_H	1	5	1	2	2	5	1	3	-1	7	2	3
		C_V	0	7	1	3	2	7	0	4	-2	8	1	12
		C_H	0	7	1	5	2	7	1	5	-2	10	0	10
290 - 299	500	L_V	1	4	0	4	2	5	1	3	-2	13	2	4
		L_H	1	5	1	4	0	5	2	3	-1	11	2	5
		C_V	0	9	1	6	1	7	1	6	-2	11	0	13
		C_H	0	8	0	5	0	11	3	7	-1	12	0	13

TABLE D-3

MEAN VALUES AND SCINTILLATION OVER 5° INTERVALS

NO. 13 BALLOON

Pattern #	Psi		m^0	Δ	m^5	Δ	m^{10}	Δ	m^{15}	Δ	m^{20}	Δ	m^{25}	Δ
312 - 329	400	L_V	3	5	0	3	0	4	0	4	0	3	0	4
		L_H	2	4	1	3	0	4	3	4	3	4	1	2
		C_V	5	6	4	11	6	7	2	5	2	6	3	8
		C_H	5	7	3	12	3	6	3	8	2	6	3	7
322 - 339	1500	L_V	2	3	0	3	-1	3	1	3	1	2	2	4
		L_H	2	3	1	3	1	2	3	2	2	3	3	4
		C_V	2	4	3	8	1	7	-1	5	-2	4	-1	6
		C_H	0	5	3	9	1	8	1	4	-1	5	0	6

TABLE D-3 Cont.

Pattern #	Psi		m 0	Δ	m 5	Δ	m 10	Δ	m 15	Δ	m 20	Δ	m 25	Δ
340 - 347	2800	L_V	2	3	1	3	-1	2	1	3	2	4	2	4
		L_H	1	2	0	3	-2	5	2	2	2	2	2	3
		C_V	0	3	1	5	-1	6	-2	6	-2	6	-1	7
		C_H	0	4	1	8	-2	9	0	5	1	5	1	5
348 - 359	4800	L_V	2	1	1	2	0	3	0	3	1	5	1	3
		L_H	2	1	2	2	0	3	2	3	3	3	2	2
		C_V	1	3	1	5	1	4	-1	5	0	5	0	5
		C_H	0	5	1	5	0	6	0	4	1	6	1	5
360 - 371	500	L_V	2	2	1	3	1	4	-1	3	-1	5	0	4
		L_H	1	2	1	3	0	5	1	4	2	3	1	4
		C_V	0	5	1	7	1	5	-1	5	-1	5	0	6
		C_H	0	5	0	7	-1	7	0	5	0	5	0	5
372 - 383	7400	L_V	1	1	1	3	0	2	-2	3	-1	5	0	3
		L_H	2	2	1	4	0	3	1	3	1	3	1	2
		C_V	0	4	1	3	0	4	-2	6	-1	6	0	2
		C_H	0	3	1	5	-1	7	-2	8	1	6	-1	3
384 - 393	500	L_V	2	2	1	2	0	3	-1	3	0	4	0	4
		L_H	1	2	1	3	0	5	2	2	2	3	2	3
		C_V	0	6	1	6	0	6	-2	7	0	5	-1	5
		C_H	-1	6	1	6	0	7	-2	6	-1	5	-1	6

D.5 DISCUSSION OF THE RESULTS

For the prime data balloon No. 13, we are interested in the mean values and scintillation as functions of frequency, pressure, and polarization. To exhibit this dependence, we have chosen to display the data in the following tables, Table D-4 and Table D-5.

TABLE D-4

m - REINFORCED GORE					m - SUMMED OVER OTHER GORES*			
PSI	L_V	L_H	C_V	C_H	L_V	L_H	C_V	C_H
400	0	1	4	3	3	9	18	18
1500	0	1	3	3	5	11	-1	1
2800	1	0	1	1	6	5	-6	0
4800	1	2	1	1	4	9	0	2
500	1	1	1	0	-1	5	-1	-1
7400	1	1	1	1	-2	5	-3	-3
500	1	1	1	1	1	7	-3	-5

*These sums, when divided by 5, give the average values of m and Δ for the unreinforced part of the balloon.

TABLE D-5

Δ – REINFORCED GORE					Δ – SUMMED OVER OTHER GORES*			
PSI	L_V	L_H	C_V	C_H	L_V	L_H	C_V	C_H
400	3	3	11	12	20	18	32	34
1500	3	3	8	9	15	14	26	28
2800	3	3	5	8	16	14	28	28
4800	2	2	7	7	15	14	22	26
500	3	3	7	7	18	18	31	27
7400	3	4	3	5	14	13	22	27
500	2	3	6	6	16	15	29	30

These tables are self-explanatory and represent the final reduction of the data obtained on the No. 13 balloon. They reveal several clear, albeit slight, dependences upon the parameters. It should be borne in mind that first of all, the computations exhibited in the tables in this report have been rounded to the nearest decibel, and that small db differences in cross section can correspond to larger percentage differences in fields, and therefore represent significant physical effects. The data reduction herein has been designed to extract from the raw data an expression of systematic dependence upon parameters. It remains an open question to decide the effects of their dependence upon a particular communications system. Even though the scintillations in the radar cross section of an A-12 balloon may be large, they are systematic and predictible, and a program to design them out of a communications system through the use of filters is feasible.

*These sums, when divided by 5, give the average values of m and Δ for the unreinforced part of the balloon.

D.6 SAMPLES OF RAW DATA